Macro Fiber Composite Actuated Control Surfaces with Applications Toward Ducted Fan Vehicles

Brandon C. Stiltner

Thesis submitted to the faculty of the Virginia Polytechnic Institute and State University
in partial fulfillment of the requirements of the degree of

Master of Science

in

Aerospace Engineering

Cornel Sultan, Chairman
Craig Woolsey
Chris Hall

2011-July-26

Blacksburg, Virginia

Key Words: morphing control surfaces, ducted fan, UAVs, MAVs, piezoelectric, PZT, macro fiber composite

© Brandon Chase Stiltner, 2011

Macro Fiber Composite Actuated Control Surfaces with Applications Toward Ducted Fan Vehicles

Brandon C. Stiltner

Abstract

In most man-made flight, vehicle control is achieved by deflecting flaps. However, in nature, morphing surfaces are found on both flying and swimming creatures. Morphing is used in nature because it is a more efficient form of control. This thesis investigates using morphing flaps to control a class of UAVs known as ducted fan vehicles. Specifically, this thesis discusses both the challenges and benefits of using morphing control surfaces.

To achieve morphing, a piezoelectric device known as Macro Fiber Composites is used. These devices are embedded in the skin of the vehicles control surface, and when actuated, they cause the control surface to increase or decrease camber. This thesis describes experiments that were performed to investigate the performance of this type of actuator. Specifically, the actuation bandwidth of these devices is presented and compared to a servo. Results show that the morphing control surfaces can actuate at frequencies twice as high as a servo.

Dedication

to Nicole, for her love and support,
and to my family,
Ann, Eddie, and Dustin…

Acknowledgments

I would first like to thank my wife Nicole, for supporting and motivating me. She has made the late nights and early mornings a little less tiring.

I would also like to thank my advisor Dr. Sultan, for being both patient and supportive. Thank you for all the advice and input over the past four years.

I would like to thank AVID LLC and Paul Gelhausen for supporting my research. I would also like to thank John Ohanian, for being a great friend and wise advisor.

I would like to thank Chris Hickling for his help with experiments and also his LabView skills. Thanks to Etan for proof reading my thesis, and the rest of the AVID crew. And finally, to the rest of the people who have helped me achieve this goal "Thanks!"

Table of Contents

ABSTRACT ii

DEDICATION iii

ACKNOWLEDGMENTS iv

TABLE OF CONTENTS v

LIST OF FIGURES vii

LIST OF TABLES x

1. INTRODUCTION 1
- 1.1 DUCTED FAN MICRO AIR VEHICLES 1
- 1.2 DF-MAV CONTROL SURFACES 3
- 1.3 MORPHING CONTROL SURFACES 6
- 1.4 OBJECTIVE AND MOTIVATION 8
- 1.5 THESIS OUTLINE 10

2. LITERATURE REVIEW 12
- 2.1 DUCTED FAN MICRO AIR VEHICLES 12
  - *2.1.1 Ducted Fan Dynamics and Control* *12*
  - *2.1.2 Ducted Fan Design* *14*
  - *2.1.3 Ducted Fan Aerodynamics* *15*
- 2.2 MORPHING AND MACRO FIBER COMPOSITE ACTUATORS 15
- 2.3 HYSTERESIS MODELING AND CHARACTERIZATION 17

3. EXPERIMENT TEST SPECIMENS 20
- 3.1 MACRO FIBER COMPOSITE ELEMENTS 20
- 3.2 THIN BIMORPH TEST ELEMENTS 24
  - *3.2.1 Bimorph Specifications* *24*
  - *3.2.2 Bimorph Geometry* *26*
- 3.3 NOVEL BIMORPH AND LINKAGE ELEMENT 30
  - *3.3.1 The Bimorph and Linkage Combination* *31*
  - *3.3.2 Bimorph and Linkage Geometry* *35*
- 3.4 AIRFOIL TEST ELEMENTS 38
  - *3.4.1 Servo-Actuated Airfoil Details* *39*
  - *3.4.2 Bimorph-Actuated Airfoil* *41*

4. STEADY STATE EXPERIMENTS 43
- 4.1 SMALL BIMORPH BENCH TEST 43
  - *4.1.1 Equipment and Initial Setup* *45*
  - *4.1.2 Hysteresis Experimental Procedure* *48*
  - *4.1.3 Voltage Overshoot Experimental Procedure* *49*
- 4.2 SMALL BIMORPH AND LINKAGE BENCH TEST 49
  - *4.2.1 Equipment and Hardware* *51*
  - *4.2.2 Procedure* *52*

5. STEADY-STATE EXPERIMENT RESULTS 54
- 5.1 SMALL BIMORPH BENCH TEST 54
  - *5.1.1 Hysteresis Loop* *54*
  - *5.1.2 Overshoot Voltage* *58*

5.1.3 Circular Arc Assumption *60*
5.1.4 Bimorph Angle of Attack *63*
5.2 SMALL BIMORPH AND LINKAGE BENCH TEST 66
5.2.1 Bimorph and Linkage Hysteresis *67*
5.2.2 Bimorph and Linkage Angle of Attack *68*
5.2.3 Bimorph and Linkage Interactions *69*
6. SYSTEM IDENTIFICATION 71
6.1 FREQUENCY RESPONSE THEORY 71
6.2 DESCRIPTION OF EXPERIMENTS 74
6.2.1 Servo (Futaba S3156) Frequency Response *74*
6.2.2 Bimorph Frequency Response *77*
6.3 DATA ANALYSIS 79
6.4 RESULTS AND DISCUSSION 82
6.4.1 Servo Results *82*
6.4.2 Cantilevered Bimorph Results *85*
6.4.3 Bimorph-Actuated Airfoil Results *86*
6.4.4 Comparison of the Servo and Bimorph Actuated Wings *87*
6.5 DISCUSSION AND CONCLUSIONS 88
7. CONTROLLING THE BIMORPH 90
7.1 CLOSED-LOOP CONTROL SIMULATIONS 90
7.1.1 Tuning the PID Gains *92*
7.2 OPEN AND CLOSED LOOP STEP RESPONSE 95
7.2.1 Experimental Procedure *95*
7.2.2 Open Loop vs Closed Loop Comparison *96*
7.3 OTHER CONTROL IMPLEMENTATIONS 99
7.3.1 Potential Sensors and Implementation *99*
7.3.2 Hysteresis Inversion and Implementation *104*
8. CONCLUSIONS 110
8.1 THE BIMORPH AND LINKAGE CONCEPT 111
8.2 CONTROLLING THE BIMORPH 112
8.2.1 Frequency Response *113*
8.2.2 Closed Loop Control *114*
8.3 FUTURE RESEARCH FOR BIMORPH CONTROL 115
9. BIBLIOGRAPHY 117

List of Figures

FIGURE 1.1: THE HONEYWELL RQ-16 T-HAWK. (PUBLIC DOMAIN, PHOTO CREDIT U.S. NAVY) 3
FIGURE 1.2: (LEFT) AVID OAV PARAMETRIC GEOMETRY DEPICTING TRADITIONAL *PLUS* VANE CONFIGURATION; (RIGHT) *X* VANE CONFIGURATION. 5
FIGURE 1.3: (LEFT) VANE DEFLECTIONS THAT PRODUCE A POSITIVE PITCHING MOMENT ABOUT THE VEHICLES *Y-AXIS*; (RIGHT) VANE DEFLECTIONS THAT PRODUCE A YAW MOMENT ABOUT THE VEHICLES *Z-AXIS*. 6
FIGURE 1.4: SAMPLE MFC PATCH. IMAGE CREDIT SMART MATERIALS CORP. (WWW.SMART-MATERIAL.COM) 7
FIGURE 1.5: SKETCH OF A FLAT PLATE MORPHING VANE WITH A PASSIVE LINKAGE TO CONTROL VANE DEFLECTION. LEFT TO RIGHT MOVES FORWARD IN TIME AND SHOWS VANE MORPHING AND DEFLECTING. 10
FIGURE 2.1: NON-IDEAL RELAY, KNOWN AS A HYSTERON, WHICH IS A BUILDING BLOCK OF THE PREISACH HYSTERESIS MODEL [HTTP://EUCLID.UCC.IE/HYSTERESIS/NODE1.HTM]. 18
FIGURE 3.1: PICTURE OF THE M8528 P1 D33 MFC ELEMENT MADE BY SMART MATERIAL CORP. IMAGE CREDIT SMART MATERIAL CORP. (WWW.SMART-MATERIAL.COM) 21
FIGURE 3.2: ILLUSTRATION DEPICTING AN MFC ELEMENT (DARK BROWN) BODED TO A SURFACE (LIGHT BROWN) AND INDUCING BENDING. IMAGE CREDIT SMART MATERIALS CORP. (WWW.SMART-MATERIAL.COM) 21
FIGURE 3.3: SCHEMATIC STRUCTURE OF AN MFC ELEMENT. IMAGE CREDIT SMART MATERIALS CORP. (WWW.SMART-MATERIAL.COM) 22
FIGURE 3.4: CROSS SECTION OF AN MFC ELEMENT DEPICTING THE FLOW OF ELECTRICITY IN THE ELEMENT. IMAGE COURTESY OF SMART MATERIALS CORP. 23
FIGURE 3.5: PICTURE OF THE 85X28MM ACTIVE AREA BIMORPH TEST ELEMENT. 24
FIGURE 3.6: EXAGGERATED DRAWING OF THE CROSS-SECTION VIEW OF A BIMORPH. 25
FIGURE 3.7: SKETCH OF THE CROSS SECTION OF THE BIMORPH WITH POSITIVE BENDING ABOUT *Z*-AXIS 26
FIGURE 3.8: CIRCULAR ARC NOTATION FOR KINEMATICS EQUATIONS 27
FIGURE 3.9: SKETCH OF A CANTILEVERED THIN BIMORPH WITH NOTATION DEFINITIONS 29
FIGURE 3.10: CHART OF ANGLE OF ATTACK α VERSUS CAMBER (% CHORD). 30
FIGURE 3.11: 3D SKETCH OF THE THIN BIMORPH WITH AXLE AND TRAILING EDGE LINKAGE 31
FIGURE 3.12: CROSS SECTION OF THE BIMORPH AND LINKAGE CONCEPT. 32
FIGURE 3.13: PICTURE OF THE SMALL BIMORPH TEST ELEMENT WITH ATTACHED AXLE AND LINKAGE. 32
FIGURE 3.14: PICTURE OF THE ENDPLATE USED FOR THE BIMORPH AND LINKAGE CONCEPT. 33
FIGURE 3.15: PICTURE SHOWING THE CENTERBODY, CONTROL VANES, AND ENDPLATES OF A DUCTED FAN VEHICLE TO ILLUSTRATE HOW THE VANES ARE CONNECTED. 34
FIGURE 3.16: PICTURE OF THE FABRICATED BIMORPH AND LINKAGE CONCEPT WITH THE ENDPLATE. 35
FIGURE 3.17: PLOT OF ANGLE OF ATTACK (α) VERSUS CAMBER. 38
FIGURE 3.18: THE SERVO-ACTUATED SELIG S1210 AIRFOIL TEST ELEMENT. 39
FIGURE 3.19: THE BIMORPH ACTUATED SELIG S1210 AIRFOIL TEST ELEMENT. 39
FIGURE 3.20: (TOP) FUTABA S3156 SERVO WITH A U.S. QUARTER FOR SIZE REFERENCE. (BOTTOM) 3-VIEW OF THE FUTABA S3156 SERVO WITH DIMENSIONS IN MILLIMETERS. IMAGE CREDIT TO SERVOCITY (HTTP://SERVOCITY.COM/) 40
FIGURE 3.21: SKETCH OF THE MORPHING SELIG AIRFOIL CROSS-SECTION TO VISUALIZE THE UPPER AND LOWER SURFACE INTERACTIONS. (TOP) POSITIVE MORPHING CONDITION FOR INCREASING CAMBER, (BOTTOM) NEGATIVE MORPHING CONDITION FOR DECREASING CAMBER. 42
FIGURE 4.1: SMALL BIMORPH CLAMPED IN A VISE DURING STEADY-STATE TESTING. 44
FIGURE 4.2: EQUIPMENT SETUP DURING THE SMALL BIMORPH STEADY-STATE TESTING. 46
FIGURE 4.3: (LEFT) PICTURE OF THE VOLTAGE DIVIDER USED DURING THE STEADY STATE EXPERIMENTS. (RIGHT) SCHEMATIC OF A VOLTAGE DIVIDER CIRCUIT. 47
FIGURE 4.4: (TOP) TWO-POSITION SWITCH USED TO MAP THE HIGH AND LOW VOLTAGE CHANNELS TO THE MFC ELEMENTS ON THE BIMORPH. (BOTTOM) SCHEMATIC OF THE TWO-POSITION SWITCH DEPICTING POSITION 1 OF THE SWITCH. 48
FIGURE 4.5: PICTURE OF THE FABRICATED BIMORPH AND LINKAGE TEST ELEMENT TAKEN DURING PROOF-OF-CONCEPT TESTING. 50
FIGURE 4.6: EQUIPMENT USED DURING THE BIMORPH AND LINKAGE BENCH TEST. NOTE THAT THE TEST ELEMENT DEPICTED IS NOT THE BIMORPH AND LINKAGE, HOWEVER THE TEST SETUP IS STILL THE SAME. 52
FIGURE 5.1: CANTILEVERED BIMORPH TEST ELEMENT DURING STEADY-STATE EXPERIMENTS. 55

FIGURE 5.2: SCREEN CAPTURE OF THE IMAGE PROCESSING SOFTWARE TO MEASURE THE DISTANCE BETWEEN THE TE (FOREGROUND) AND THE STRAIGHT EDGE (BACKGROUND). 55
FIGURE 5.3: TRAILING EDGE DEFLECTION OF THE CANTILEVERED BIMORPH FOR 0V TO 5V (RISING SECTION), AND 5V TO 0V (FALLING SECTION). 56
FIGURE 5.4: ADDITIONAL TRAILING EDGE DEFLECTION OF THE CANTILEVERED BIMORPH. 57
FIGURE 5.5: HYSTERESIS LOOP OF THE CANTILEVERED BIMORPH SHOW THE RELATIONSHIP BETWEEN TE DEFLECTION (OUTPUT) VERSUS INPUT VOLTAGE. 58
FIGURE 5.6: FIRST TEST TO DETERMINE THE OVERSHOOT VOLTAGE NECESSARY TO REACH ZERO TRAILING EDGE DEFLECTION FOR THE BIMORPH. 59
FIGURE 5.7: SECOND TEST TO DETERMINE THE OVERSHOOT VOLTAGE NECESSARY TO REACH ZERO TRAILING EDGE DEFLECTION FOR THE BIMORPH. THIS TEST WAS PERFORMED TO DETERMINE IF THE INITIAL ACTUATION VOLTAGE WOULD AFFECT THE AMOUNT OF OVERSHOOT. 60
FIGURE 5.8: SCREEN SHOT OF THE POINT TRACKING SOFTWARE. 61
FIGURE 5.9: 0MM TE DEFLECTION MORPHING CONDITION WITH IMAGE PROCESSING DEPICTING THE CIRCLE FIT TO THE CLAY DABS. 62
FIGURE 5.10: 0% MORPHING CONDITION WITH IMAGE PROCESSING DEPICTING THE CIRCLE FIT TO THE CLAY DABS. .62
FIGURE 5.11: 100% MORPHING CONDITION WITH IMAGE PROCESSING DEPICTING THE CIRCLE FIT TO THE CLAY DABS. 63
FIGURE 5.12: -100% MORPHING CONDITION WITH IMAGE PROCESSING DEPICTING THE CIRCLE FIT TO THE CLAY DABS. 63
FIGURE 5.13: PICTURE OF THE IMAGE PROCESSING SOFTWARE DEPICTING THE MEASUREMENTS OF ANGLE OF ATTACK. 64
FIGURE 5.14: CALCULATED AND MEASURED ANGLE OF ATTACK VERSUS PERCENT MORPHING. 65
FIGURE 5.15: CALCULATED AND MEASURED ANGLE OF ATTACK VERSUS CAMBER (% CHORD LENGTH). 66
FIGURE 5.16: PICTURE OF THE BIMORPH AND LINKAGE DURING BENCH TESTING. 66
FIGURE 5.17: HYSTERESIS PLOT FOR THE BIMORPH AND LINKAGE CONCEPT. 67
FIGURE 5.18: MEASURED ANGLE OF ATTACK FOR THE BIMORPH AND LINKAGE CONCEPT. 68
FIGURE 5.19: MEASURED ANGLE OF ATTACK AND CALCULATED ANGLE OF ATTACK FOR THE BIMORPH AND LINKAGE CONCEPT. 69
FIGURE 5.20: PICTURE OF THE BIMORPH AND LINKAGE DURING TESTING AT DIFFERENT ACTUATIONS TO ILLUSTRATE THE TRAVEL OF THE SLIDE BEARING. 70
FIGURE 6.1: EXAMPLE BODE DIAGRAM [51]. 73
FIGURE 6.2: SINUSOIDS OF THE SAME FREQUENCY WITH DIFFERING AMPLITUDE AND PHASE [51]. 73
FIGURE 6.3: SCHEMATIC OF THE FREQUENCY RESPONSE EXPERIMENT FOR THE SERVO ACTUATED WING SECTION. .75
FIGURE 6.4: EXAMPLE PWM SIGNAL FOR ACTUATING A SERVO. 76
FIGURE 6.5: PICTURE OF THE SERVO IN THE AIRFOIL WITH THE WOODEN STICK ON ITS ARM (USED FOR THE LASER). 77
FIGURE 6.6: PICTURE OF THE CANTILEVERED BIMORPH DURING THE FREQUENCY RESPONSE TEST. 78
FIGURE 6.7: PICTURE OF THE BIMORPH ACTUATED WING SECTION DURING THE FREQUENCY RESPONSE TESTS. 78
FIGURE 6.8: FLOW CHART OF DATA DURING THE BIMORPH FREQUENCY AND TRANSIENT EXPERIMENTS. 79
FIGURE 6.9: LASER MEASUREMENT (BLUE) AND FITTED SINE WAVE (BLACK) FROM THE CANTILEVERED BIMORPH FREQUENCY RESPONSE AT 1HZ. 82
FIGURE 6.10: BODE DIAGRAM FOR THE SERVO IN UNLOADED AND LOADED CONDITIONS. 83
FIGURE 6.11: BODE DIAGRAM OF THE LOADED SERVO AND MODELED TRANSFER FUNCTION. 85
FIGURE 6.12: BODE DIAGRAM OF THE CANTILEVERED BIMORPH AND THE MODELED TRANSFER FUNCTION. 86
FIGURE 6.13: BODE DIAGRAM OF THE BIMORPH ACTUATED WING SECTION AND THE MODELED TRANSFER FUNCTION 87
FIGURE 6.14: BODE DIAGRAM OF THE MODELED TRANSFER FUNCTIONS FOR THE BIMORPH AND SERVO ACTUATED WING SECTIONS. 88
FIGURE 7.1: BLOCK DIAGRAM OF THE BIMORPH CONTROL SIMULATION IN SIMULINK 91
FIGURE 7.2: BLOCK DIAGRAM OF THE PID CONTROL SUBSYSTEM SHOWN IN THE BLOCK DIAGRAM IN FIGURE 7.1. 91
FIGURE 7.3: BODE PLOT OF A BUTTERWORTH FILTER WITH 30HZ CUTOFF FREQUENCY 92
FIGURE 7.4: SIMULATED STEP RESPONSE OF THE BIMORPH ACTUATOR WITH K_{CR} = 0.43 93
FIGURE 7.5: SIMULATED STEP RESPONSE OF THE BIMORPH WITH PI CONTROL 94
FIGURE 7.6: SIMULATED STEP RESPONSE OF THE BIMORPH WITH FULL PID CONTROL 94

FIGURE 7.7: DIAGRAM OF THE SETUP UTILIZED FOR THE CLOSED LOOP CONTROL EXPERIMENTS PERFORMED ON THE CANTILEVERED BIMORPH. 96
FIGURE 7.8: OPEN AND CLOSED LOOP STEP RESPONSE FOR A 10MM STEP INPUT 97
FIGURE 7.9: OPEN AND CLOSED LOOP STEP RESPONSE FOR A 20MM STEP INPUT 97
FIGURE 7.10: OPEN AND CLOSED-LOOP STEP RESPONSE FOR A -10MM STEP INPUT. 98
FIGURE 7.11: (LEFT) IMAGE OF A STANDARD POTENTIOMETER; (RIGHT) SKETCH OF A POTENTIOMETER. 101
FIGURE 7.12: (LEFT) IMAGE OF THE BIMORPH AND LINKAGE CONCEPT DURING TESTING, (RIGHT) CROSS-SECTION VIEW OF THE BIMORPH AND LINKAGE TO SHOW THEIR INTERACTIONS. 102
FIGURE 7.13: 85X15MM MFC ELEMENT WITH 85X3MM MFC FOR SENSING. 104
FIGURE 7.14: MODELED HYSTERESIS CURVES FOR THE CANTILEVERED BIMORPH WITH 85X28MM ACTIVE AREA MFC ELEMENTS. 105
FIGURE 7.15: BLOCK DIAGRAM ILLUSTRATING HOW THE INVERSE HYSTERESIS MODEL IS USED TO RESHAPE THE INPUT TO THE BIMORPH. 107
FIGURE 8.1: PICTURE OF THE BIMORPH AND LINKAGE CONCEPT TAKEN DURING STEADY STATE EXPERIMENTS 110
FIGURE 8.2: CANTILEVERED BIMORPH ANGLE OF ATTACK VERSUS INPUT VOLTAGE. 111
FIGURE 8.3: BIMORPH AND LINKAGE ANGLE OF ATTACK VERSUS INPUT VOLTAGE. 112
FIGURE 8.4: BODE DIAGRAM FOR THE SERVO ACTUATED WING SECTION. THIS MATERIAL IS PRESENTED IN CHAPTER 6. 113
FIGURE 8.5: BODE DIAGRAM FOR THE BIMORPH ACTUATED WING SECTION. THIS MATERIAL IS PRESENTED IN CHAPTER 6. 114
FIGURE 8.6: POSITIVE STEP RESPONSE OF THE BIMORPH IN OPEN AND CLOSED LOOP OPERATION. THIS MATERIAL IS PRESENTED IN CHAPTER 7 115
FIGURE 8.7: NEGATIVE STEP RESPONSE OF THE BIMORPH IN OPEN AND CLOSED LOOP OPERATION. THIS MATERIAL IS PRESENTED IN CHAPTER 7 115

List of Tables

TABLE 5.1: DATA FOR CIRCULAR FIT PARAMETERS FOR THE DEFLECTED BIMORPH ELEMENT.....61

1. Introduction

Morphing control surfaces offer many aerodynamic benefits over traditional hinged flaps. One such benefit of morphing control surfaces is efficiency due to lower drag. A testament to this fact is the aerodynamic shapes that naturally occur such as bird wings or the fins of a fish. Man-made flight has shied away from conformal surfaces in favor of rigid deflecting surfaces because they are much easier from a mechanical standpoint. However, the advent and understanding of so-called *smart materials* has inspired research in areas of morphing surfaces. The following chapter introduces a research project in which morphing control surfaces were investigated with a focus toward ducted fan UAVs. The feasibility of using smart materials for morphing control is presented. The ducted fan vehicle was chosen because it has unique control challenges that are not found with fixed wing or rotorcraft vehicles. Namely, ducted fan vehicles are unstable, and control is a crucial aspect to achieve a successful design. The developments set fourth in this thesis will show that morphing control surfaces can now be utilized for aircraft control.

The remainder of this chapter presents more detail on this research. Ducted fan vehicles and their control surfaces are discussed in more detail. An introduction to the morphing control surfaces used for this research is also presented. Lastly, the specific motivation and problem statement of this research is given.

1.1 Ducted Fan Micro Air Vehicles

Ducted Fan Micro Air Vehicles (DF-MAVs) are a relatively new type of unmanned aerial vehicle that are gaining interest in both military and commercial sectors. Over the past 10 years, much research has been conducted surrounding these vehicles and the military is currently using these vehicles in combat. Ducted fan MAVs have become popular because they have many benefits compared to traditional fixed wing and rotorcraft vehicles. Among these benefits are the abilities to hover and perch, fly at high speeds, and they are more transportable than their fixed wing and rotorcraft counterparts.

Elaborating on these benefits, VTOL capabilities make them easily deployable and retrievable from many locations, therefore removing the need to prepare a launch or landing site. Removing the dependence on a launch site allows the vehicle to be

deployed quickly when a threat arises or battlefield information is needed. Furthermore, DF-MAVs have the capability to hover and perch. Hover and stare capabilities are of great importance to today's infantry. This enables the vehicle to survey a battlefield or target for long periods of time, and a stable hovering platform can also be outfitted with a laser designator. The ability to perch on rooftops and other structures allows the vehicle to rest, thereby reducing power consumption. Perching permits the vehicle to reduce its engine to idle, extending its mission life by reducing fuel consumption.

The above outlines the DF-MAVs benefits over fixed wing vehicles, but what sets the DF-MAV apart from helicopters is its ability to fly at high speeds. Helicopters are hindered by a physical speed limit imposed by the advancing-retreating rotor blade phenomenon [1]. While DF-MAVs still exhibit this phenomenon, it is greatly reduced by the recessed fan inside the duct. Essentially, the duct channels the airflow so that the flow is nearly perpendicular with the fan. Furthermore, the duct generates lift due to the turning of the airflow around the duct's lip. This makes the DF-MAV more efficient at producing thrust compared to an open rotor of the same diameter. The added lift from duct lip can be as much as 50% greater when compared to the same open propeller [2].

Additionally, the DF-MAVs compact shape allows them to be easily carried in a backpack with minimal disassembly required. This is yet another advantage over fixed wing and rotorcraft vehicles, which tend to be awkward to carry due to appendages such as the wings or rotor. This is very beneficial to the soldier due to faster, easier, and more discrete deployment.

The Honeywell RQ-16 T-Hawk[1], depicted in Figure 1.1, is currently serving in the war in Iraq and Afghanistan. The T-Hawk is a platoon level asset meaning that it is owned and operated by an infantry or dismounted platoon. The T-Hawk's gross takeoff weight is roughly 20lbs, allowing it to be carried in a backpack by a soldier. Because the vehicle is a platoon entity, the chain of communication is greatly reduced, allowing it to communicate directly with the soldiers using it. Fast communication between the vehicle and soldiers is very important because the vehicle provides them with real-time battlefield information.

[1] http://www.thawkmav.com/system_features.php

Additionally, the T-Hawk can cruise at speeds up to 50mph. Thus, it has the ability to arrive on station shortly after it is deployed, and remove itself from hostile situations quickly when necessary. Sited missions for the T-Hawk include forward scouting and suspicious target surveillance with an endurance of about 40 minutes.

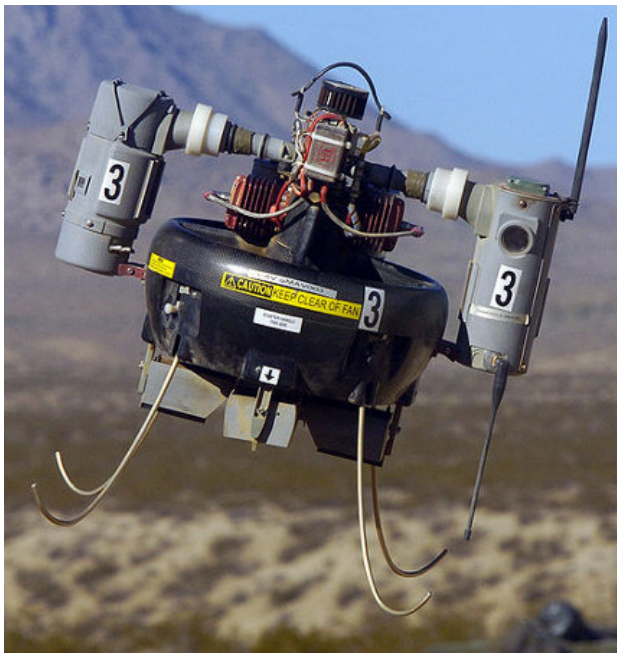

Figure 1.1: The Honeywell RQ-16 T-Hawk. (Public Domain, photo credit U.S. Navy)

1.2 DF-MAV Control Surfaces

A disadvantage of ducted fan vehicles is that they are inherently unstable, making vehicle control an active area of interest to researchers and designers. The instability arises for a two main reasons. First, consider an example of a ducted fan and neglect the aerodynamics. In this case, the vehicle's lift is exactly equal to the thrust the vehicle produces. If the thrust acts through the vehicle's CG, the vehicle is neutrally stable. Otherwise, the thrust causes a moment about the CG that must be countered by the control surfaces. The thrust-induced moment grows larger as the CG moves further away from the thrust line. If the moment is large enough that the control surfaces cannot counter it, the result is a statically unstable vehicle. Thus, the first cause of the instability arises if the CG is not located along the thrust line.

Now, assume the realistic condition when the vehicle's aerodynamics are *not* neglected. Now the vehicles lift is a combination of the thrust and the aerodynamic lift

on the duct. Furthermore, the ducted fan vehicle's Center of Pressure (CP) changes location depending on the flight condition. In fact, unlike standard fixed wing aircraft, the ducted fan's CP is very sensitive to flight condition. This means that the vehicle's total lift varies with the flight condition, because the lift acts through the CP. Therefore, the vehicle lift causes a moment about the vehicle's CG that must be counteracted by the control surfaces. This effect results in a dynamically unstable craft.

Traditionally, ducted fan vehicles are controlled via control surfaces known as vanes, which are located in the exhaust flow of the duct. Control vanes can be seen in Figure 1.1 at the bottom of the T-Hawk vehicle. Servomotors are the typical actuators that drive the vane deflections. Deflecting a vane causes a change in its Angle of Attack (AoA) relative to the exhaust flow of the duct, thus increasing the lift force on the vane. Because the control vanes are located away from the vehicles mass center (CG), the vane's lift induces a moment and causes the vehicle to rotate. The control vanes affect the DF-MAV in the same way that ailerons, elevator, and rudder affect a fixed wing aircraft.

Two vane configurations are depicted in Figure 1.2. The left picture depicts a standard vane configuration known as the *plus* configuration. Each vane is driven by a separate servo, therefore each vane actuates independently. The vanes located along the *y-axis* (red) cause a pitching moment when actuated in the same sense (depicted in Figure 1.3 left). Similarly, a rolling moment is achieved by deflecting the vanes oriented along the *x-axis* (green) in the same sense. Finally, a yawing moment is achieved by actuating all 4 vanes simultaneously, but differentially, shown in Figure 1.3 (right).

The right of Figure 1.2 depicts another type of vane configuration. This is a multiple vane configuration in which the vanes are spaced radially around the ducts circumference. Furthermore, the vanes are not located along the vehicles axes, but are clocked 45 degrees about the vehicles *z-axis*. This configuration is provided to show that many different vane configurations can be used to achieve the desired control authority. In this case, each vane pair is driven individually by servos located in the center of the duct at the root of the vanes. Images are taken from the design software AVID Organic Air Vehicle (OAV) [14].

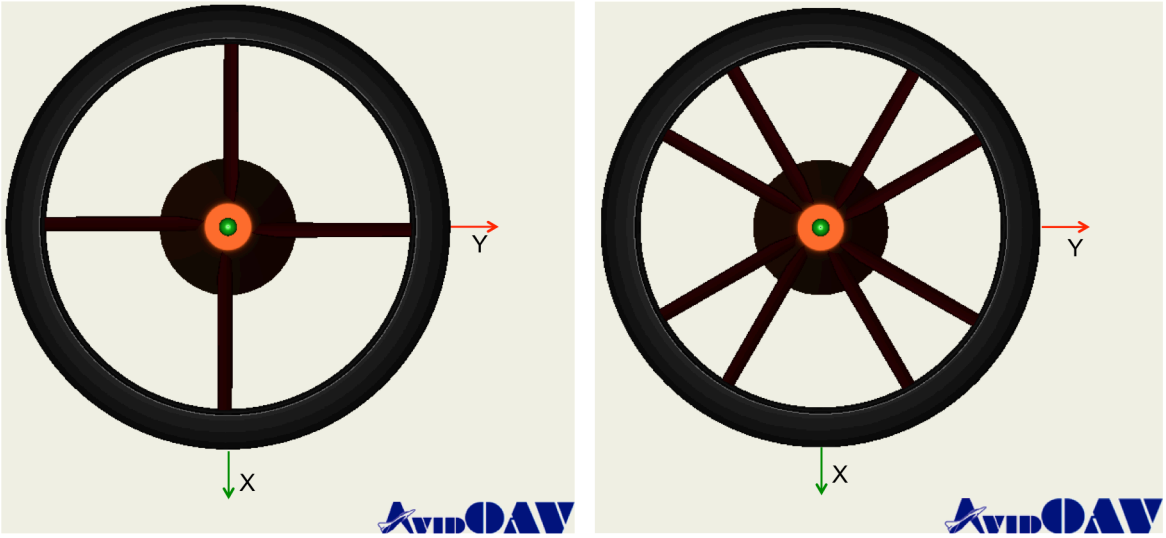

Figure 1.2: (Left) AVID OAV parametric geometry depicting traditional *plus* vane configuration; (Right) *X* vane configuration.

Some designs have utilized trailing edge flaps on the control vanes to yield even more control authority. Instead of the rigid flaps depicted in Figure 1.2 and Figure 1.3, envision a vane with a hinged flap at its trailing edge. Typically, a linkage is used to actuate the flap so that the flap deflects with the vane. Furthermore, other researchers have investigated non-traditional control effectors. These include leading and trailing edge blowing on the duct via synthetic jets, and active morphing control vanes [19,21,33]. It is the latter that the research presented here will explore. In this context, vane morphing implies changing the airfoil camber so that lift is generated by the control surface.

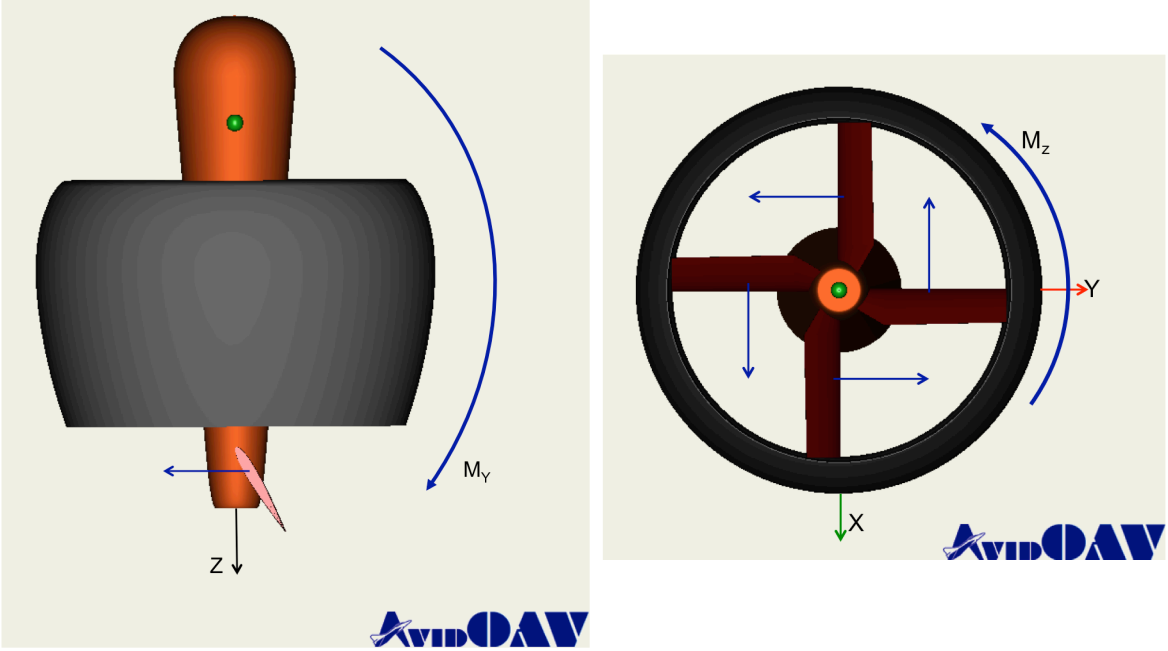

Figure 1.3: (Left) Vane deflections that produce a positive pitching moment about the vehicles *y-axis*; (Right) Vane deflections that produce a yaw moment about the vehicles *z-axis*.

1.3 Morphing Control Surfaces

Morphing control surfaces offer a drag reduction when compared to traditional hinged flap deflection [3]. Through the utilization of piezoelectric materials, the task of airfoil camber morphing has been made easy. Researchers have investigated using Macro Fiber Composite (MFC) elements as an actuator for active morphing [3,18,19,20,21,48]. MFCs are a type of actuator made up of piezoceramic material, typically Lead Zirconate Titanate (PZT). These piezoelectric devices exhibit the *direct piezoelectric effect*. This means that the MFC element produces an electric potential when a strain is applied. In this case, the MFC element is utilized for sensing. By mapping known strain values to known electric potential output (voltage), the MFC element is used to sense bending, stretching, or vibrations in a structure. Materials that exhibit the direct piezoelectric effect also exhibit the *indirect piezoelectric effect*, which is simply the opposite effect. The MFC exhibits strain (elongation) in the presence of an electric potential. Thus, applying voltage to the element causes expansion or contraction within the MFC, depending on the sense of the voltage. By embedding the MFC element

in a surface, the MFC is used as an actuator to induce bending. A single MFC patch is shown in Figure 1.4 below.

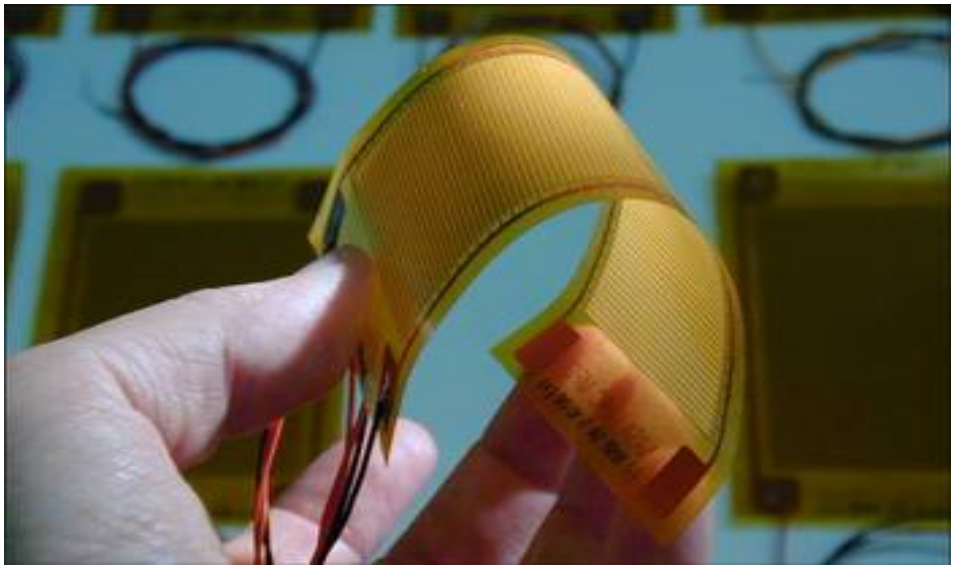

Figure 1.4: Sample MFC patch. Image credit Smart Materials Corp. (www.smart-material.com)

To drive bending in an element, a piezoelectric beam is constructed which is referred to within this research as a *bimorph*. The bimorph is made up of two MFC elements, stacked one on top of the other and bonded together so that no slip can occur at the interface between the elements. The bimorphs are sometimes referred to as *piezoelectric beams* in related literature. Applying a voltage to the two MFCs, both of the same magnitude but opposite polarity, causes contraction in one MFC and expansion in the other. The expansion and contraction causes bending, which is achieved because slip between the layers is prevented [4]. Here, bending provides the necessary actuation to drive airfoil camber morphing. This is described more thoroughly in Chapter 3 of this thesis.

A few disadvantages exist with MFCs: they require large voltages and they exhibit hysteresis. First, up to 1.5kV is required to fully actuate the MFC element. Fortunately, they require low current for actuation, resulting in low power consumption [18]. In the past, MFC elements have only been successfully used in lab environments or on large-scale systems. This is because the electronics necessary to produce the high voltages are heavy, reducing the benefits of using the MFC element as an actuator. However, recent research has shown that circuitry can be built that allows the use of MFCs on small

UAVs [18,20]. Here, MFC patches were successfully flown on a small (0.82 kg) fixed wing UAV. The MFC patches were embedded in the surface of the wing near the wing tips. The MFC actuation caused wing tips to morph, acting as the aircrafts ailerons to produce the roll moments.

Hysteresis, on the other hand, is a nonlinear behavior typically referred to as path-dependent output or *memory*. Hysteresis makes MFC elements difficult to use when precise control is required. This is because the exact state of the MFC element cannot be calculated by simply knowing the input voltage. Without a model of the hysteresis, sensing is required to determine the exact state of the MFC.

1.4 Objective and Motivation

The objective of this thesis is to address the use of morphing control vanes on ducted fan MAVs. Specifically, the problems addressed here are from that of a controls-engineering standpoint. Past research has shown that morphing control vanes may be able to produce the necessary amount of forces to adequately control a DF-MAV.

In the previous sections, both the benefits and shortcomings of DF-MAVs were outlined, along with problems surrounding MFC actuators and control vane morphing. Essentially, DF-MAVs are unstable and require a high level of control authority for adequate maneuverability and stable flight. Adequate control authority is achieved through proper design of the control vanes and many different configurations have been considered in the past. Thus, much emphasis is placed on control vane design during the preliminary and conceptual phases of ducted fan vehicle design. Proving that morphing control vanes are feasible on ducted fan provides the designer with another configuration.

Vane deflections are typically actuated via servomotors, however, research has shown that vane morphing via MFCs could be a viable substitute. For servo-actuated vanes, the servos are typically located near the control vanes in the aft portion of the duct. If heavy, the servos pull the vehicles CG aft resulting in a lack in control authority. Hence, designers also attempt to minimize the servos impact on the vehicle CG location. Research has shown that MFC elements could be used to morph the vane's camber, and that flight weight electronics can be fabricated that are suitable for MAVs [19]. Unfortunately, the same research found that morphing alone does not provide enough

control authority to adequately maneuver the vehicle throughout its flight envelope (unpublished). Therefore, morphing must be combined with changing the vanes angle of attack to achieve the desired level of control. To meet that end, a novel control vane and linkage mechanism has been conceptualized so that both morphing and vane deflections are achieved simultaneously.

Investigating the feasibility of implementing the MFC control vane and linkage mechanism on a DF-MAV is the primary objective of this research. Servomotors are currently employed on working DF-MAVs to drive deflection of rigid vanes. However, a few concerns exist with servos, which are addressed in the following:

- Loss of a servo during flight could compromise the entire vehicle mission.
    - ♦ Benefit: Redundancy can be added to the system by using multiple MFC patches along the span of the control vane.
- As the vehicles size and mass decrease, servo actuated systems become difficult to implement.
    - ♦ Benefit: MFCs are conformal to most any surface and can be custom manufactured for almost any size control vane.
- Servos are composed of small gears, which can be stripped if the servo is accidentally back-driven.
    - ♦ Benefit: MFCs do not require gears, and can be actuated by external forces without a negative impact.
- Servos, while relatively lightweight, may still have a negative effect on vehicle CG due to their location in the aft portion of the vehicle.
    - ♦ Benefit: The driver circuitry required for MFCs can be placed wherever needed based on CG or MOI constraints.
- Servos, while small, still take up a finite amount of volume.
    - ♦ Benefit: MFC elements are embedded in the control vane's skin, minimizing their impact on internal volume.

Recall that morphing and angle of attack must be used to achieve the necessary control authority for ducted fan vehicles. To meet that end, a linkage was added to the morphing vane to cause a change in angle of attack. The morphing vane and linkage concept is shown in Figure 1.5. Here, the morphing control vane is a simple flat plate

profile with a rounded leading edge and sharp trailing edge (blue). An axle located at the vane's quarter chord supports the lift force of the vane and allows the vane to rotate (green in Figure 1.5). The linkage (yellow) is rigidly fixed to the trailing edge of the vane, while the other end of the linkage is pinned into a slotted plate. This end of the linkage is fixed so that it can only rotate and translate within the confines of the slot. Figure 1.5 depicts the combined vane morphing and deflection starting from left to right. Essentially, morphing causes the vane to change camber, which causes an additional increase in angle of attack due to the linkage kinematics.

The specific aim of this research is to characterize the performance of the novel morphing vane and linkage concept, which could be implemented on a DF-MAV. It should be noted that the control vane and linkage concept is not limited to DF-MAVs, and is only the specific aim of this research. Both the advantages and disadvantages of this concept are presented, and its performance is characterized and compared to that of a servo actuated system.

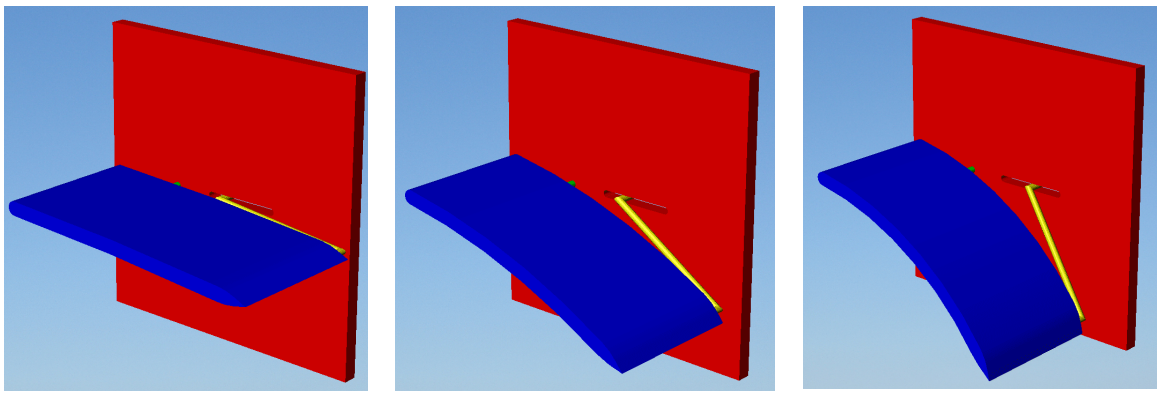

Figure 1.5: Sketch of a flat plate morphing vane with a passive linkage to control vane deflection. Left to right moves forward in time and shows vane morphing and deflecting.

1.5 Thesis Outline

Chapter 2 gives a detailed literature review of past and current research being performed in related areas. This chapter is broken down into sections pertaining to specific areas of this research. A section is given which focuses on research devoted to ducted fan MAVs, while another section is devoted active morphing using smart materials and MFCs.

Chapter 3 is devoted to describing the experimental hardware that was developed during the duration of this research. Here, more detail is given regarding MFC elements and the morphing vane and linkage concept discussed earlier.

Chapters 4 and 5 provide the experimental procedure and results of steady state experiments that were performed to characterize the control vane and linkage concept. Here, steady state means that no transient or dynamic behavior is measured during these experiments. The specific goal of these experiments was to measure the amount of angle of attack that can be achieved by the bimorph and linkage concept.

Chapter 6 describes some frequency response experiments that were conducted to characterize the bandwidth of both a servo and a bimorph. The servo and bimorph test specimens used for these experiments are also described in Chapter 3. From the frequency response experiments, models of the specimens are obtained in the form of transfer functions. Using these transfer functions, a simulation was created so that feedback control can be used to control the bimorph. Proportional-Integral-Derivative control is discussed in Chapter 7. Here, simulation was used to tune the PID gains, and the gains are then used during control experiments. Step responses are given for the bimorph in both open and closed loop operation. Finally, Chapter 8 summarizes the conclusions that are presented throughout this thesis.

2. Literature Review

There are many areas of research that are related to the work described within this thesis, and without which, this research wouldn't have been possible. This chapter presents some of the related work that concerns the research described within this thesis. This chapter is thus broken down into 3 sections. First, some research pertaining to ducted fan vehicles is provided. Next, a section concerning morphing control and macro fiber composite actuators is provided. Last, a section is given which discusses the mathematical modeling of the hysteresis behavior that piezoelectric devices exhibit. The references discussed in this chapter are provided in the Bibliography at the end of this thesis. The bibliography also provides references, which are not specifically discussed within this thesis, but were utilized and aided in the work performed here.

2.1 Ducted Fan Micro Air Vehicles

Ducted Fan MAVs are unique when compared to other aerial vehicles. These vehicles can hover and have Vertical Take-Off and Landing (VTOL) capabilities, and can also fly at high speeds comparable to fixed wing vehicles of relative size. Recognizing ducted fan MAVs benefits, many researchers have studied these vehicles in recent decades. However, the idea of using ducted fans for VTOL applications is not a new one. One of the first uses of Ducted Fan Vehicles, or DFVs, was the Piasecki VZ-8 Airgeep[2], which was a prototype vehicle that debuted around 1957. Researchers have since pushed the DFVs flight envelope to new levels, far surpassing that of the Airgeep. In the past decade, literature concerning ducted fan vehicles has been flooded with topics such as performance, stability and control, and design methodologies. A few of these are detailed in the following paragraphs.

2.1.1 Ducted Fan Dynamics and Control

Many texts address the subject of fixed wing aircraft stability and control. Stevens and Lewis [25] and Etkin [26, 27] are very well known authors whose books are found on most aerospace engineers shelves. Both present the 6 Degree Of Freedom (DOF) Equations Of Motion (EOMs) for fixed wing aircraft. They touch on both lateral and

[2] http://www.piasecki.com/geeps_pa59k.php

longitudinal stability, as well as aspects of closed-loop control. Etkin and Reid [27] is oriented toward students, and has a wealth of knowledge of fixed wing stability, while Stevens and Lewis is written toward simulation of the EOMs and both classical and modern control. Both texts explain the derivation of the EOMs for a rigid fixed wing aircraft and focus attention on linearizing those equations about trim, and obtaining traditional state and control matrices. Last, another great book, often considered a classic among control engineers, is McRuer *et. al.* "Aircraft Dynamics and Automatic Control" [28].

Most concerning to this research is ducted fan vehicle stability, dynamics, and control. As mentioned in Chapter 1, these vehicles are unstable over their range of flight conditions. Fleming *et. al.* [5] performed research to better understand the ducted fan vehicle *baseline* aerodynamics as well as the control vane aerodynamics. The research was also concerned with testing, aerodynamic modeling, and selection of new control device concepts for DFVs. From wind tunnel tests, the authors characterize the baseline vehicle and control vane performance in both hover and crosswind flight conditions. Additionally, Stiltner *et. al.* [6] presents a modal analysis of a generic ducted fan vehicle in various flight conditions. This paper presents the vehicle modes that comprise the ducted fans instability.

Other authors have addressed the control of ducted fan vehicles. Hess & Ussery [7] and Hess & Bakhtiari-Nejad [8] address using sliding mode techniques for control of a 6 Degree Of Freedom (DOF) model for a DFV linearized about hover. Through simulation, the authors show that the sliding mode control increases robustness characteristics compared to that of classical loop shaping when the vehicle is in hover.

Researchers also address controlling DFVs by employing dynamic inversion techniques. Johnson & Turbe [9] research the use of dynamic inversion with adaptation to control a small DFV developed at Georgia Tech called the GTSpy. The vehicle's duct has an 11" O.D., is 27" tall, and weighs 5.5 lbs. Here, the authors develop an aerodynamic model for the DFV and address the Equations of Motion (EOMs). Through flight testing, the authors show close matching of autonomous maneuvers with simulated results.

Smith *et. al.* [10] addresses control a 9" diameter DFV in the hover flight condition using a linear dynamic inversion technique. Spaulding *et. al.* [11] discusses using nonlinear dynamic inversion control for a small DFV. Here, the authors describe using both linear and nonlinear dynamic inversion for the specific application to control DFVs. The authors believe that nonlinear dynamic inversion greatly simplifies the design of the DFV control system for two reasons. It reduces the complex vehicle dynamics to that of a simple integrator and can cover the entire flight envelope without the need of gain scheduling. Finally, researchers have studied control and simulation of tandem DFVs. Tobias & Horn [12] create a generic simulation model for a tandem DFV that models the inflow of ducted rotors, control vane forces and moments, and the duct pitching moment. Specifically, the authors research using rotor cyclic and collective control in combination with control vanes to control a tandem DFV.

Lastly, Ozdemir & Horn [13] address the control of a tandem DFV and employ dynamic inversion techniques for closed loop control. Here, the authors study the vehicle dynamics in an attempt to achieve minimal tilt angles when performing translational maneuvers. The authors combine the use of traditional rotor craft control mechanisms such as collective and cyclic pitch control, and the use of control vanes down stream of the rotors. Through simulation, the authors show that the use of control vanes greatly decrease the pitch and roll angles considerably for lateral and longitudinal translation maneuvers.

2.1.2 Ducted Fan Design

Research has also been performed for DFVs in the areas of modeling and vehicle design. Ko *et. al.* [14] describe the ducted fan modeling and design software tool Organic Air Vehicle (OAV). OAV was developed by engineers at AVID LLC and is discussed in Chapter 1 of this research. OAV is a design tool for the conceptual and preliminary design phases that uses an Multi-Disciplinary Optimization methodology to allow the user to quickly model and perform trade studies with specific mission phases and requirements in mind. The software encompasses the prediction of vehicle aerodynamics, fan and stator performance, mass properties, control vane performance, among others. Furthermore, Zhang *et. al.* [15] discusses the geometric modeler called

Parametric Aircraft Geometry Engine (PAGE), which is used within OAV as the geometric modeler. PAGE is an aircraft modeling software that allows the user to rapidly generate a vehicle geometry within the scope of a day, rather than using a CAD software that is more accurate but also much more time consuming. Usually during the conceptual and preliminary design stages, many different vehicle concepts are being explored. Thus, PAGE is advantageous when compared to CAD as the user can quickly build multiple vehicle configurations to meet the rapidly changing vehicle design.

2.1.3 Ducted Fan Aerodynamics

The literature on DFVs also concerns aerodynamic modeling. Many of the authors above discuss various aerodynamic models used for simulation and vehicle flight controls [9, 12, 14]. Ohanian *et. al.* [16] goes into great detail to describe the ducted fan aerodynamics using a non-dimensional modeling scheme. The authors study a generic ducted fan configuration to obtain wind tunnel aerodynamic data. The wind tunnel data is then non-dimensionalized to obtain information about ducted fan vehicles similar to classical non-dimensional analysis for fixed wing and rotary winged craft. The authors were able to capture nonlinear characteristics of the force, moment, and power and represent these terms in simple equations, similar to the classical lift and drag equations. Avanzini *et. al.* [17] also develop a ducted fan aerodynamic model which is used to investigate performance and stability characteristics for DFVs. The authors provide a stability analysis in the form of open root-locus plots for various trimmed forward flight conditions.

2.2 Morphing and Macro Fiber Composite Actuators

Many researchers have addressed the topics of morphing and the aerodynamic benefits of morphing surfaces. Considering nature, most flying and swimming creatures utilize morphing and conformal surfaces for control, instead of rigid elements with hinged control surfaces typical of man-made aircraft. Furthermore, many researchers have addressed MFCs and piezoelectric materials for aerospace applications. MFC elements offer a cheap and light-weight alternative to other forms of actuation. MFCs come in many different shapes off-the-shelf, and can also be custom made if desirable.

They are also malleable and conform to many convex or concave surfaces. However, MFCs are not without drawbacks, as they require high input voltages to achieve their full range of actuation (up to 1.5kV). Luckily, while the driving voltages are high, the amplitude is quite low and thus resulting in low power draw.

Solecki & Conant [4] provide the reader with a brief overview of the electrical and material theory underlying piezoelectric and piezoceramic materails. In Chapter 8, the authors derive the structural equations to describe a piezoelectric bimorph, or piezoelectric beam. The authors derive the bending moment and strain associated with applying a voltage to the bimorph. Additionally, authors provide an example problem (8-13) in which they derive the vertical deflection of the free end of a cantilevered bimorph. This problem is very important as is shown later in this thesis.

Bilgen *et. al.* [18,19,20,21] has made significant contributions in the area of morphing wings using MFC actuators. In [20], the authors perform wind tunnel tests to compare a variable camber airfoil and a conventional, flapped airfoil. Both airfoils are chosen as thin circular arcs with 1.8% camber. The wind tunnel tests were performed in low Reynolds number ranges ($Re \approx 1x10^5$). The authors show that the L/D (lift-to-drag ratio) of the morphing airfoil is 10-50% greater than that of the conventional flapped airfoil. Furthermore, the authors discuss the design and flight tests of a fixed wing MAV (0.76 m wingspan) that utilizes embedded MFC patches on the wing tips for roll control via camber change. According to the authors, many incidents occurred during flight tests and even after the hardest landings, the MFC patches remained undamaged. In a later work, Bilgen *et. al.* further describes the flight tests of the fixed wing MAV [18]. A significant contribution from this work is the development of flight weight electronics to drive the MFC elements. The vehicles Gross-Take-Off-Weight (GTOW) is 851g and 103g of which is taken up by the electronics that drive the MFCs. Along with flight tests, measurements of roll moment were taken in an open jet wind tunnel that allowed the authors to predict a vehicle roll rate of 1.4rad/sec. During flight testing, the vehicle achieved a roll rate of 0.93rad/sec.

Other authors have also performed research in morphing surfaces and aerodynamics although not necessarily using MFC actuation [22, 23, 24]. Marques *et. al.* [22] address the affect of morphing through the use of a variable camber flap for a low speed UAV.

The authors use unique trailing edge, variable camber flap that extends as it is deflected and is similar to a fowler flap. The flap concept maintains continuity along the upper surface of the airfoil only. Most importantly, the authors show through experimentation a 40% decrease in actuation energy required to deflect the conformal flap when compared to a traditional hinged flap. Garcia *et. al.* [23] at the University of Florida have developed two small fixed wing aircraft for roll control testing via wing morphing. The first MAV, with a 24 inch wingspan, has a torsion rod imbedded along the span direction in the wing skin that is rotated via servos located in the fuselage. The second smaller MAV, with a 12in wingspan, morphs via threads strung between a servo (located in the fuselage) and attachment points near the outboard section of the wings. In a later work, the authors claim that a roll rate of 300 degrees per second is achievable via the wing *curling* type of morphing [24].

2.3 Hysteresis Modeling and Characterization

MFC elements are difficult to use as actuators when precise actuation is required due to hysteresis. For a short definition, Wolfram[3] claims that *hysteresis* is the response of a system that is defined not only by its current input, but its past history of inputs. Because hysteresis is present in MFC elements, the control engineer must somehow account for this behavior in the control system to control the actuator. This can be done in a number of ways. For the purposes of this research, only two general concepts are considered for dealing with actuator hysteresis. First, a sensor can be used to determine the state of the actuator, thus allowing feedback control of the MFC element or actuated device. Second, the hysteresis can be accurately modeled and accounted for mathematically within the control law or vehicle model, allowing for pseudo open-loop control of the MFC. The following papers discuss both modeling and controlling actuators that exhibit hysteresis.

The most well known hysteresis model is the Preisach model. This model was developed by a German mathematician named Franz Preisach around 1935 [30]. The Preisach model is essentially a system of parallel-connected non-ideal relays known as hysterons. A typical hysteron is shown in Figure 2.1.

[3] scienceworld.wolfram.com, keyword search *hysteresis*

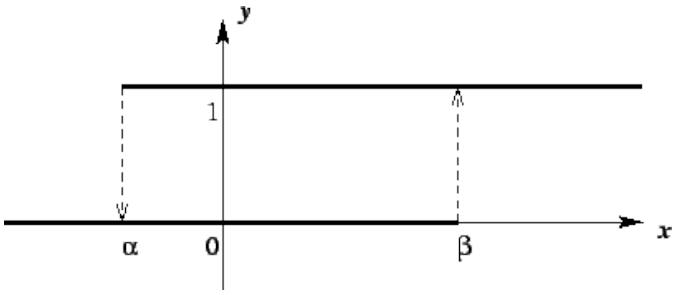

Figure 2.1: Non-ideal relay, known as a hysteron, which is a building block of the Preisach hysteresis model [http://euclid.ucc.ie/hysteresis/node1.htm].

The hysteron in Figure 2.1 has two outputs, either on (1), or off (0). The outputs are based on the both the current input value (x) as well as the past history of the input. For example, for x less than α, the output y is 0. As x is increased to a value equal to β, the output switches from off to on (0 to 1). The output then remains at 1 for all x greater than β. Likewise, as x decreases, the output remains at 1 until the value $x = \alpha$, when the output switches from on to off. The values of α and β are known as the *switch off* and *switch on* values, respectively. The Department of Applied Math at the University College, in Cork Ireland, provides a great interactive reference for understanding hysteresis[4].

Bilgen *et. al.* [19] performed research on variable camber airfoils using embedded MFC actuators and is essentially the forefather of the research described within this thesis. In the research, the authors perform wind tunnel tests for a flat camber, 12.6% thick, 127 mm chord airfoil at Reynolds numbers of $Re \approx 1.3 \times 10^5$. The airfoil section has MFC bimorph patches embedded in the upper and lower skin for actuation. Furthermore, the authors characterize the hysteresis loop for the embedded MFC airfoil segment in the form of tip deflection, lift, and drag plots.

Many authors have addressed mathematical models to characterize hysteresis. Papers by Kurdila and Webb [29] outline the use of the well-known Preisach model and the Krasnosel'skii and Pokrovskii (KP) models for hysteresis. These papers are concerned with modeling the hysteresis in active materials mostly directed toward Shape Memory Alloys (SMAs). Other work of note whom have addressed modeling and compensation for actuators that exhibit hysteresis with the Preisach model are [31,32,36]. One particular paper of note is Song *et. al.* [32] in which the authors characterize the

[4] http://euclid.ucc.ie/hysteresis/node1.htm

hysteresis loop of a piezoceramic actuator. The authors also discuss tracking control of the actuator with hysteresis compensation.

Other authors have investigated MFCs for active flow control and vibration control. Ohanian *et. al.* [33] presents a research wherein MFC bimorphs were used as Synthetic Jet Actuators (SJAs) as active flow control for ducted fan aerial vehicles. Viswamurthy & Gagnuli [34] investigate the use of piezoelectric actuators for helicopter vibration control through the use of trailing edge flaps on the main rotor. The authors intend to use embedded piezo-ceramic materials for Individual Blade Control (IBC). One interesting quote from the authors that has a significant impact on the research described within this thesis is summed as follows: "*Piezo-ceramic materials are fundamentally nonlinear in their response… exhibiting a hysteresis effect between the electric field and the displacement. Mechanical linkages designed to amplify the stroke of piezoceramic actuators further amplify this hysteresis effect.*"

3. Experiment Test Specimens

The following chapter provides a description of the hardware and technologies used throughout the duration of this research. The hardware ranges from piezoceramic materials, to using the piezo-elements to fabricate thin-plate test elements. The author also provides a description of a commonly used servo for UAV control. The remainder of the chapter is broken down into four parts.

Section 3.1 gives a description of the piezoceramic elements used for this research which are known as Macro Fiber Composites (MFCs). Section 3.2 gives a description of two, thin-plate bimorph test elements. The term *bimorph* is used extensively throughout this thesis, which is better defined within the section. Section 3.2 also defines some geometric relationships that govern the thin test elements. Section 3.3 describes the thin test element and the linkage combination. As mentioned in Chapter 1, a linkage was added to the trailing edge of the bimorph to achieve larger deflections. And last, Section 3.4 provides a description of two airfoil test elements that were used during this research. Here, one of the airfoil test sections has a servo that actuates a trailing edge flap. The second airfoil utilizes piezoceramic actuators embedded in the upper surface that change the airfoil's camber.

3.1 Macro Fiber Composite Elements

Macro Fiber Composite (MFC) devices are a piezoelectric device made by Smart Material Corp.[5] A picture of an MFC element is given in Figure 3.1. The uses of these devices range from sensing strain or vibrations in structures, to actively deforming aircraft structures, to harvesting energy from vibrations in buildings and bridges. In one instance, researchers embedded MFCs in the skin of the vertical tail fins of a fighter aircraft [35]. The goal of that research was to reduce in flight bending stresses experienced on the vertical tail due to aerodynamic buffeting.

MFCs are made of the piezoceramic material Lead Zirconate Titanate (PZT), and exhibit the *direct piezoelectric effect*. This means that the MFC element will produce an electric potential when strain is applied. In this case, the MFC element is utilized for sensing. By mapping measured strain values to voltage output, the MFC element can be

[5] http://www.smart-material.com/

used to sense bending, stretching, or vibrations in a structure. Fortunately, these materials also exhibit the *indirect piezoelectric effect*, which is the opposite of the direct effect. Here, the MFC exhibits strain (elongation) in the presence of an applied voltage potential. So, applying voltage to the element causes expansion or contraction within the piezoceramic element, depending on the sense of the voltage. By bonding the MFC element to a surface, the MFC can be used as an actuator to induce bending. This process is depicted in Figure 3.2 below.

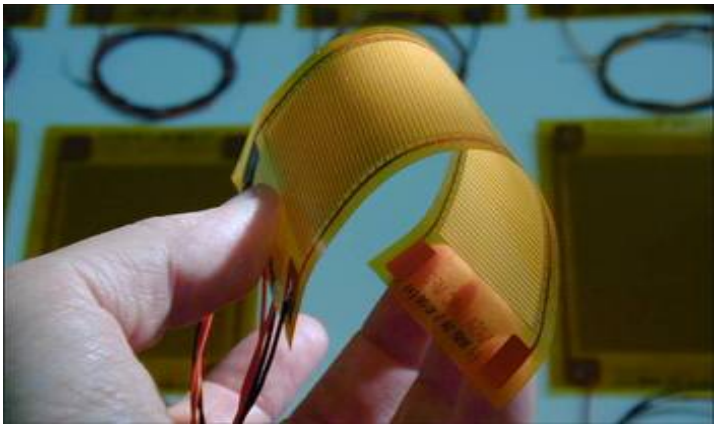

Figure 3.1: Picture of the M8528 P1 d33 MFC element made by Smart Material Corp. Image credit Smart Material Corp. (www.smart-material.com)

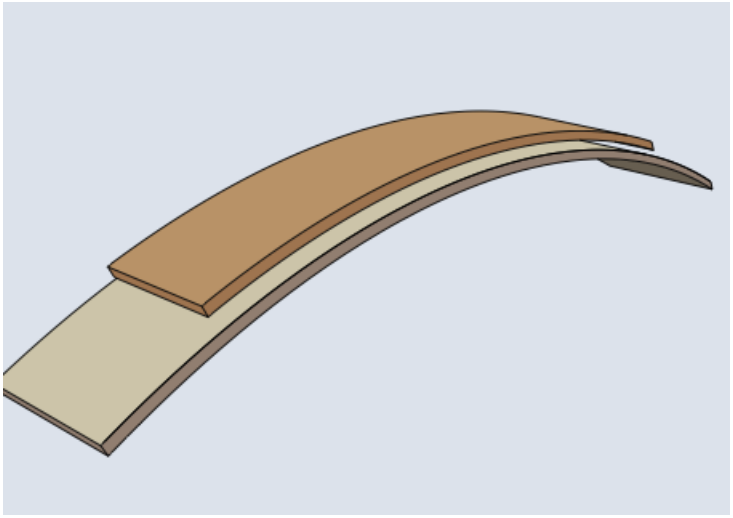

Figure 3.2: Illustration depicting an MFC element (dark Brown) boded to a surface (light brown) and inducing bending. Image credit Smart Materials Corp. (www.smart-material.com)

One specific element used for this research are type M8528-P1-d33. Here, the designation is as follows: the first numbers 8528 are the dimensions of the MFC element in millimeters (85mm x 28mm), the P1 designation means that the ceramic fibers are

oriented so that elongation of the element is the mode of operation. Finally, the d33 designation means that the MFC is designed for maximum actuation and elongation along the elements length, as opposed to its width or thickness. Figure 3.1 depicts a M8528-P1-d33 MFC element.

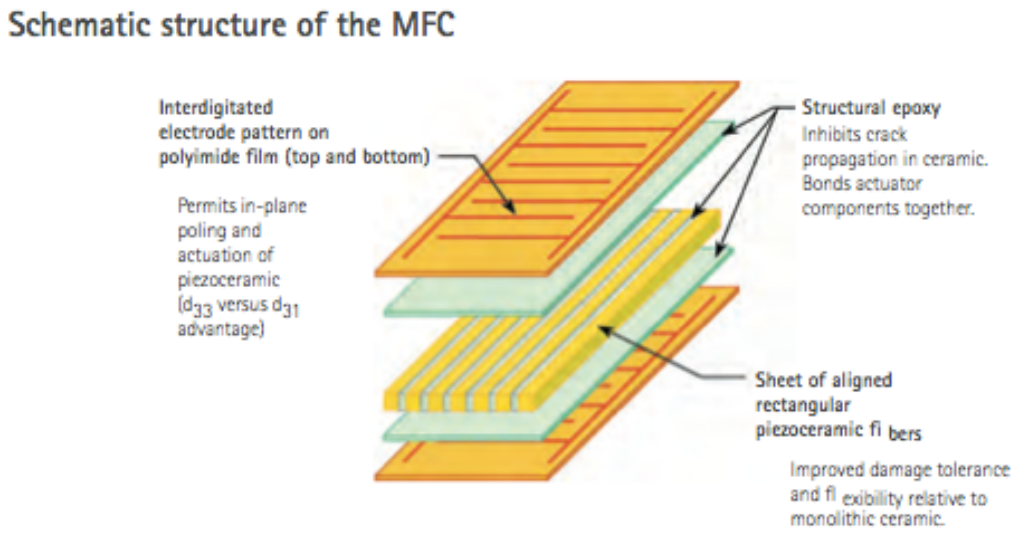

Figure 3.3: Schematic Structure of an MFC element. Image credit Smart Materials Corp. (www.smart-material.com)

Figure 3.3 provides a buildup view of an MFC element. The outer most layers (orange) of the MFC is made up of Interdigitated Electrodes (IDEs). The middle layer is the PZT material (yellow), and the sandwich is held together by the two epoxy layers (light blue). Finally, the entire element is environmentally sealed with kapton.

The PZT fibers make up the center of the sandwich and expand or contract when voltage is applied. The voltage is applied to the IDEs that make up the outer layer of the element. As can be seen, there are two electrodes that span the length of the element (dark orange lines). These electrodes have perpendicular branches that span the width of the MFC element. When connected to a voltage source, one of these electrodes will be positively charged, while the other is negatively charged. The electricity tries to flow from positive to negative voltage, but cannot because the circuit is not closed. An electric field is created between each of the IDEs, which cause expansion or contraction in the PZT material. This is better visualized in Figure 3.4.

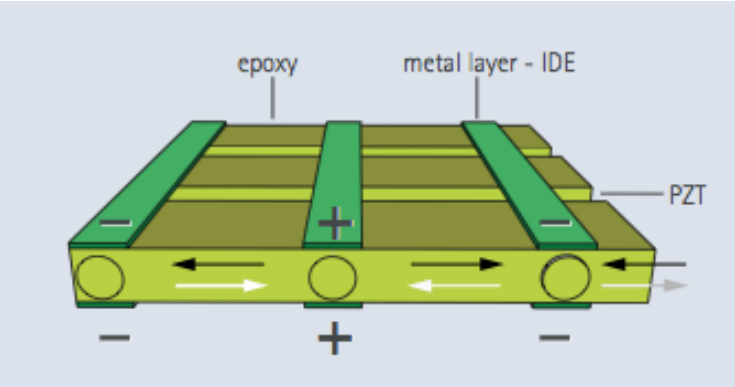

Figure 3.4: Cross section of an MFC element depicting the flow of electricity in the element. Image courtesy of Smart Materials Corp.

In Figure 3.4, the bars oriented left to right represent the PZT fibers. The vertically oriented bars (labeled with '+' or '-') represent the perpendicular IDE branches discussed above. As mentioned above, an electric field is created between each of the IDE branches. A positive charge causes the PZT fibers to expand, and the black arrows illustrate this in the figure. This expansion occurs between each IDE over the length of the MFC element. On the contrary, applying a negative voltage to the MFC causes contraction in the element. The white arrows in Figure 3.4 depict the mode of contraction for the element.

This research is mainly concerned with the high level aspects of the MFC element. This can be summed up into four questions. First, how much voltage is required to actuate the MFC elements? Second, how fast can the MFCs actuate (*i.e.* their bandwidth)? Third, what is the amount of actuation force that the MFCs provide? Lastly, how much power is required to actuate the MFC elements?

The first question has already been answered. As mentioned earlier, the MFCs require up 1500V (DC) to achieve maximum expansion. However, they only require up to 500V in a negative sense for contraction. Furthermore, the MFCs contract much less than they expand. For this reason, two MFCs are combined to form a *bimorph*, which is discussed in the following section.

The MFCs actuation bandwidth is answered within this thesis. It is shown that the bandwidth of the bimorph actuators is much higher than that of a servo. Unfortunately, the remaining two questions are not answered withing this thesis. However, some authors have discussed the amount of power consumption from the bimorph actuators

[3,18,19,20,21]. Although not presented within this thesis, the author would like to note that research is ongoing concerning the power consumption of the bimorph actuators. Preliminary results show that the bimorphs consume roughly the same amount of power as servos over their range of operating frequencies.

3.2 Thin Bimorph Test Elements

Two thin piezoelectric test elements were used during this thesis. For the remainder of the thesis, these elements will be called *bimorphs*. The author calls them bimorphs because they are piezoelectric beams made up of *two* MFC elements, and because they can morph symmetrically about their equilibrium state. One of the bimorphs can be seen in Figure 3.5.

The remainder of this section describes the bimorph elements that were used during this research. The author provides a brief description of how the bimorphs were fabricated, along with their physical dimensions. Furthermore, some geometric relationships that govern the bimorphs are given.

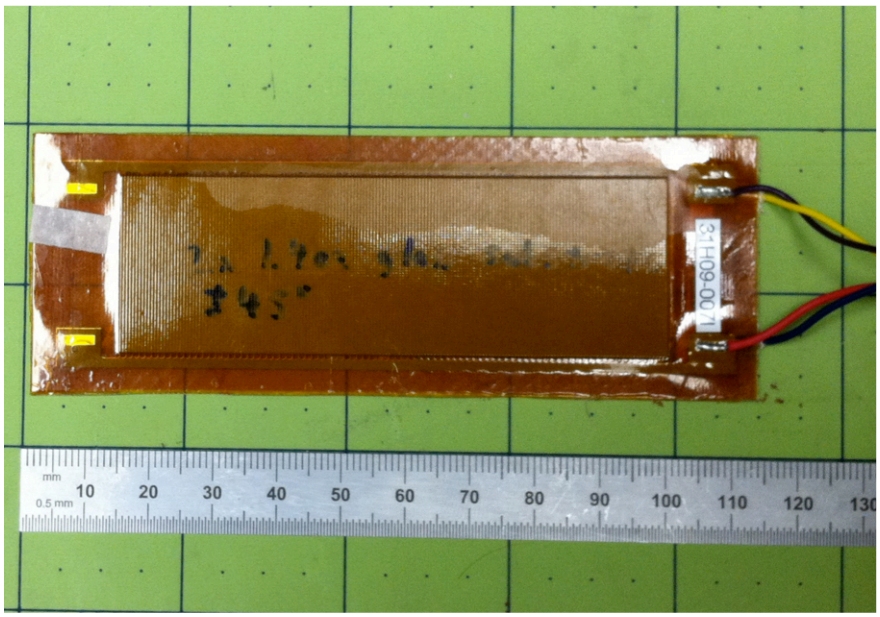

Figure 3.5: Picture of the 85x28mm Active Area Bimorph Test Element.

3.2.1 Bimorph Specifications

Bimorphs are made up of two MFC elements that are bonded together via epoxy. In some cases, the bimorphs also have a substrate material, which is material sandwiched

between the two MFCs. Both bimorphs used in this research had substrates that were made up of two plies of 1.4oz/sq. yard fiberglass. An exaggerated cross section view of a bimorph better visualizes this concept in Figure 3.6. Note that the figure depicts the bimorph in a morphed state, and that the bimorphs length and thickness dimensions are shown.

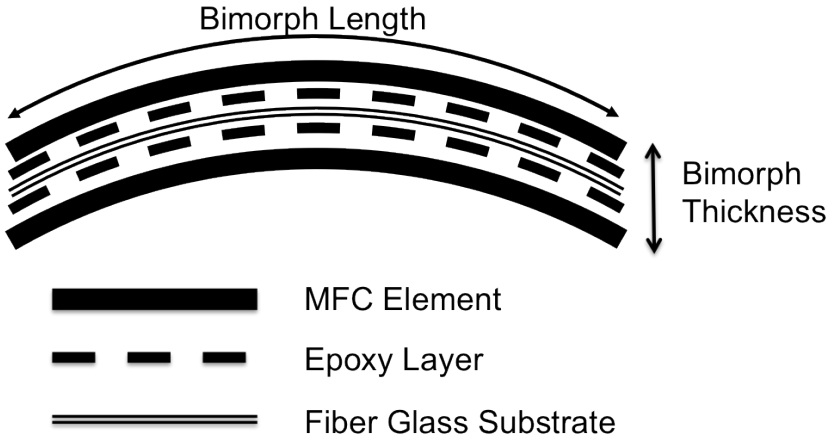

Figure 3.6: Exaggerated drawing of the cross-section view of a bimorph.

Figure 3.5 provides a picture of one of the bimorphs used during this research. Specifically, this is a picture of the 85x28mm active area bimorph. In the figure, the dark area is known as the active area of the MFC, which is the MFC element. The lighter, outer area is the fiberglass substrate of the bimorph. And last, the wires are soldered to the IDEs on each MFC element. The overall length of the bimorph is 113.0mm (4.45 inches), while the length of the active area is 85mm (3.35 inches). Furthermore, the total width of the bimorph is 40.6mm (1.6 inches), while the width of the active area is 28mm (1.1 inches).

The second bimorph test element used was slightly smaller than the bimorph shown in Figure 3.5. The smaller bimorph was used for bench testing and was outfitted with the linkage concept. Pictures of this bimorph are shown later in Section 3.3 where the bimorph and linkage combination is described. The dimensions of this bimorph are as follows. Its overall length is 108mm (4.25 inches), while the active area length is 85mm (3.45 inches). The width is 16.5mm (0.65 inches), while the active area width is 10mm (0.4 inches).

To actuate the bimorph, voltage is supplied to the MFC elements via wires that are connected to the IDEs. For expansion, the MFCs require up to 1500 volts (DC) in a positive sense, and negative 500 volts for contraction. Therefore, to actuate the bimorph, positive voltage is applied to the top MFC element to cause expansion in that element. The expansion causes tension stresses in the beam above its Neutral Axis (NA). Simultaneously, negative voltage is applied to the bottom MFC element, causing contraction. Contraction causes compression stresses in the beam below the NA. The result is a couple about the centerline of the bimorph. As shown in Figure 3.7, applying voltage in this manner causes a positive bending moment about the *z*-axis. In the reverse case, applying negative voltage to the top element, and positive voltage to the bottom creates a negative bending moment about the *z*-axis.

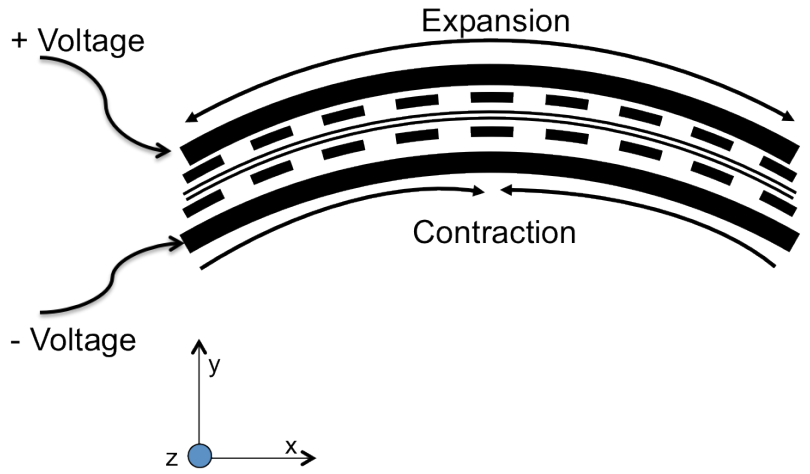

Figure 3.7: Sketch of the cross section of the bimorph with positive bending about *z*-axis.

3.2.2 Bimorph Geometry

The geometric relationships that describe a circular arc are used to describe the morphed shape of a bimorph. Essentially, this assumes that the deflected shape of the bimorph will approximate a circular arc for all applied voltages. Figure 3.8 depicts a circular arc and defines the notation used to describe the bimorph. Here, c is the chord length of the bimorph, and the arc length is unity. So, the un-deflected case results in $c = 1$. The radius is denoted by r, and y is the camber of the arc defined as the maximum thickness measured between the arc and the chord line. In the un-deflected case, the camber is zero.

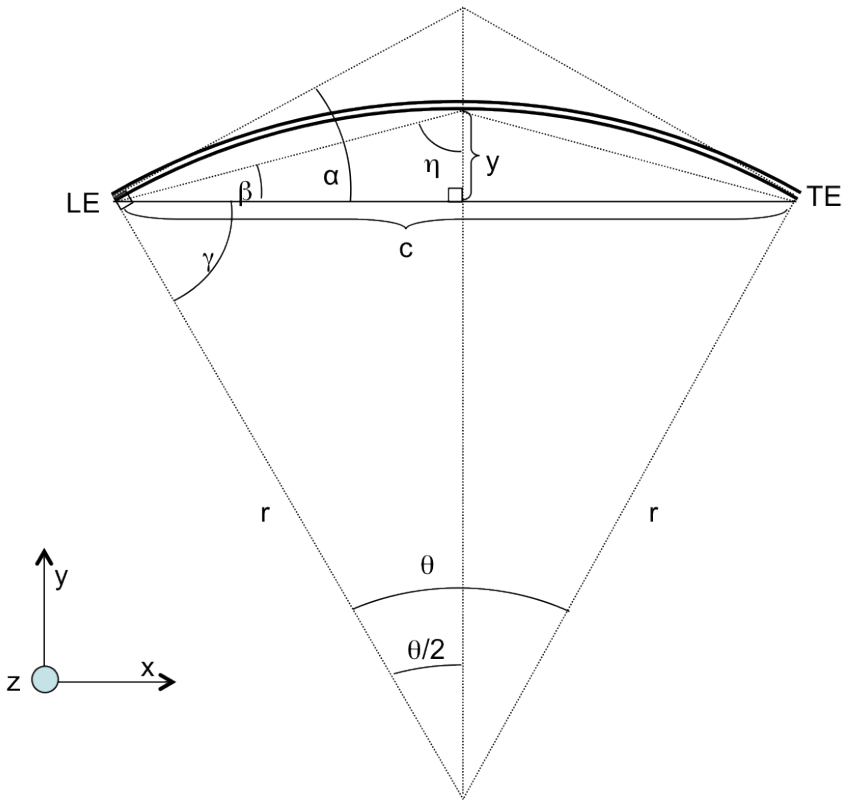

Figure 3.8: Circular Arc Notation for Kinematics Equations.

The value of camber is given as a percentage of the chord length. This makes the camber ill defined due to the changing chord length when the bimorph changes shape. Given the previous statement, a second assumption is drawn that the camber *y* remains small enough such that *c* is approximately 1 for all morphing conditions. This assumption essentially states that *r* remains sufficiently large for all morphing conditions.

From the assumptions and Figure 3.8, the following kinematics equations are derived.

$$\eta = \arctan\left(\frac{0.5}{y}\right)$$

Equation 3-I

$$\frac{\theta}{2} = 180^{\circ} - 2\eta$$

Equation 3-II

$$r = \frac{1}{\theta}$$

Equation 3-III

$$c = 2r\sin\left(\frac{\theta}{2}\right)$$

Equation 3-IV

$$\alpha = \frac{\theta}{2}$$

Equation 3-V

Equation 3-I through Equation 3-V are defined in all but one morphing condition. As the bimorph approaches its un-morphed neutral position (*i.e.* zero camber), the radius grows infinitely large. For all other morphed conditions, the equations above can be used to describe the steady-state morphing of a bimorph.

While these equations provide interesting results, the case used to derive the equations is not very useful (*i.e.* a beam under pure bending and free at both ends). So, the example is extended to a case that is more meaningful to aerospace engineers. Figure 3.9 depicts a cantilevered bimorph undergoing actuation. This case can be likened to a morphing flap that is attached to a wing, such as a morphing elevator or aileron.

Given Figure 3.9, the definition of angle of attack (α) is made as the angle between the un-deflected condition (horizontal) and the chord line. From Figure 3.9 and the equations, a relationship is derived between angle of attack and camber which is written as

$$\alpha = \frac{\theta}{2} = 180^\circ - 2\eta = 180^\circ - 2\arctan\left(\frac{0.5}{y}\right)$$

Equation 3-VI

Using Equation 3-VI, α is plotted against camber to show the angles of attack that are achieved by the cantilevered bimorph. Figure 3.10 shows a linear relationship between angle of attack and morphing. The same assumptions are used for Equation 3-VI that were used for defining the circular arc equations. Again, note that a singularity exists in the equation when the bimorph is un-deflected, or when camber is zero.

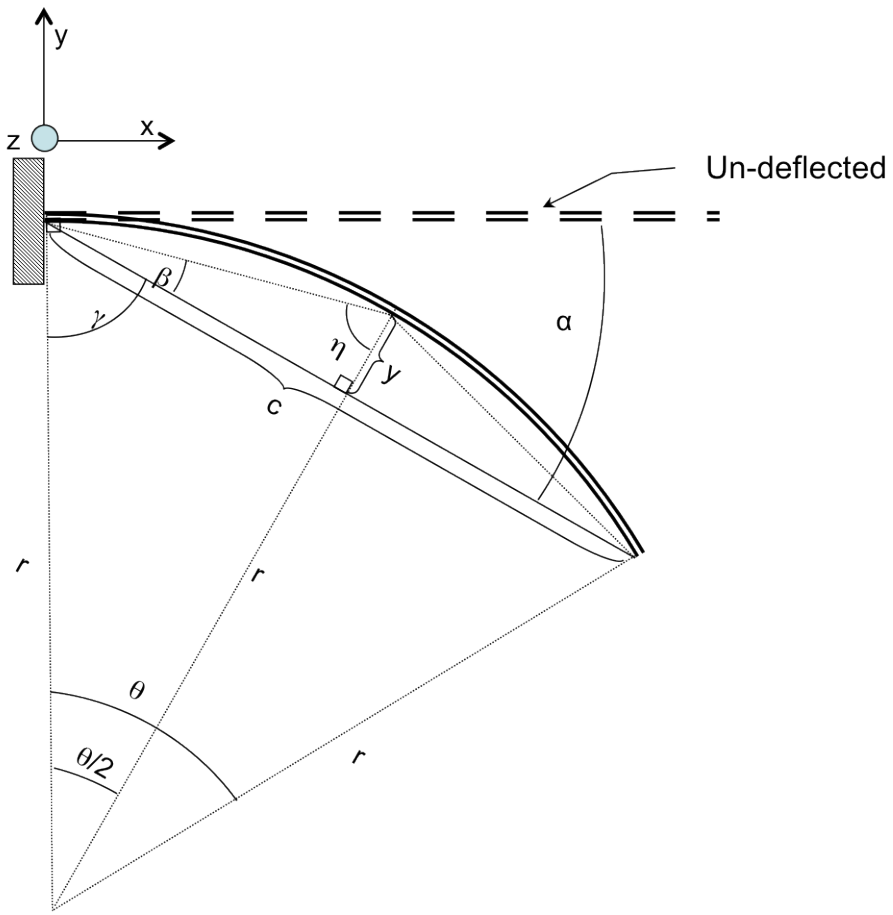

Figure 3.9: Sketch of a Cantilevered Thin Bimorph with Notation Definitions

From Figure 3.10, some important information is deduced. Recall that this example is an approximation of a morphing trailing edge flap such as an aileron. Assuming that the cantilevered bimorph achieves 8% camber, the best angle of attack that can be achieved is about 17°. Experience has shown that rigid flaps on ducted fan vehicles achieve about 25° before stall occurs. As mentioned in Chapter 1, this reinforces the fact that morphing alone cannot provide the desired control for ducted fan vehicles. Which is why a mechanism is desired that passively causes the bimorph to rotate (*i.e.* change α) while it undergoes morphing. Effectively increasing the bimorphs total angle of attack.

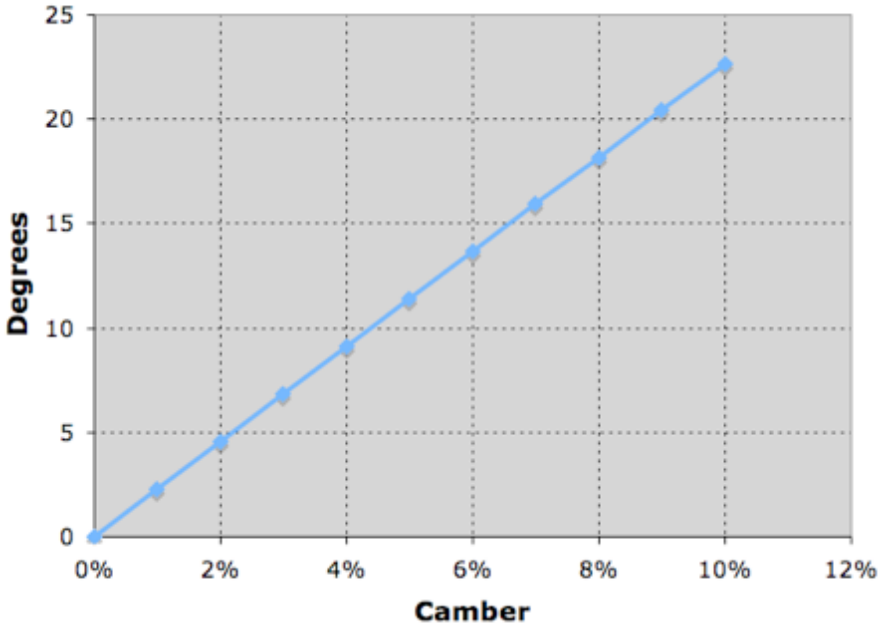

Figure 3.10: Chart of Angle of Attack α versus Camber (% Chord).

3.3 Novel Bimorph and Linkage Element

In the previous section, it is shown that morphing alone does not provide enough angle of attack to produce the control authority required for UAVs. So, a method was sought to improve the angle of attack (α) of the bimorph by utilizing the mechanical output of the morphing. To do this, the author proposed attaching a linkage to the trailing edge of the bimorph. A picture of this design is shown in Figure 3.11. In the following section the author discusses adapting the small bimorph element with a linkage so that α is controlled through morphing.

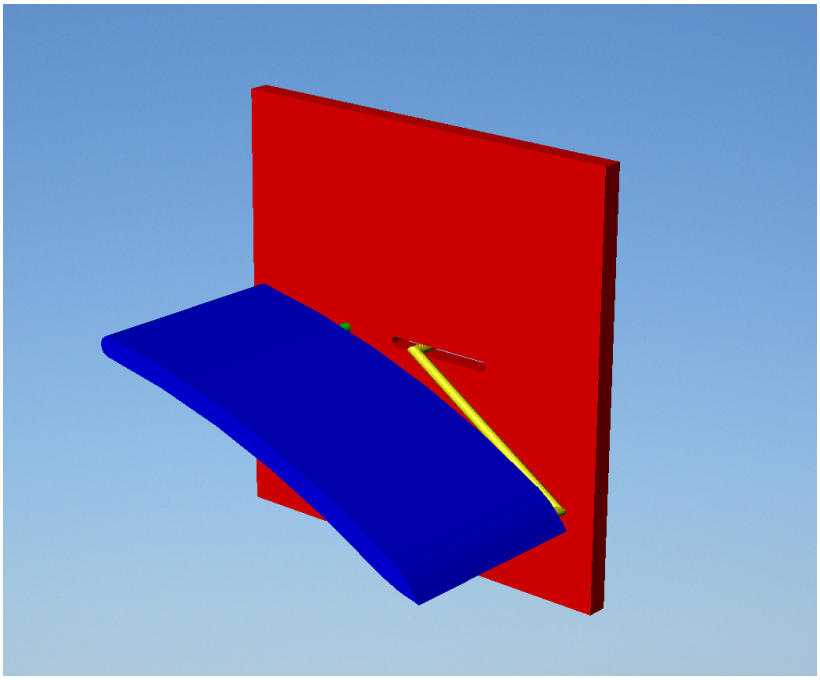

Figure 3.11: 3D Sketch of the Thin Bimorph with Axle and Trailing Edge Linkage

3.3.1 The Bimorph and Linkage Combination

The small bimorph element discussed in Section 3.2 was retrofitted with the trailing edge linkage. The linkage is added to the bimorph so that it can achieve larger angles of attack while undergoing morphing. Adding the passive linkage may potentially allow the ducted fans control vane to achieve angles of attack up to 60°, thus achieving higher lift than morphing only. Figure 3.12 provides a cross-section sketch of the thin bimorph and linkage concept, and also provides the notation used within this section. The remainder of this section describes how the small bimorph was retrofitted with the linkage, and describes how the linkage allows the vane to change angles of attack.

The bimorph was first given an axle about which it can rotate (B). The axle allows the vane to rotate freely about the *z-axis* (out of the page) shown in Figure 3.12. Here, the axle was placed at the quarter chord location of the vane ($h = 0.25c$) and serves as both the spar and a hinge point. The quarter chord was selected for convenience in this case, and is not representative of a specific design characteristic. However, it will be shown later that the location of the vane axle (h) is a design parameter that affects the achievable amount of angle of attack. The opposite end of the axle is supported by an endplate via a bearing so that the axle may rotate but not translate. The axle can be seen

attached to the small bimorph in Figure 3.13. Last, the angle of attack is denoted by α in Figure 3.12, and is the angle between the chord line and the horizontal.

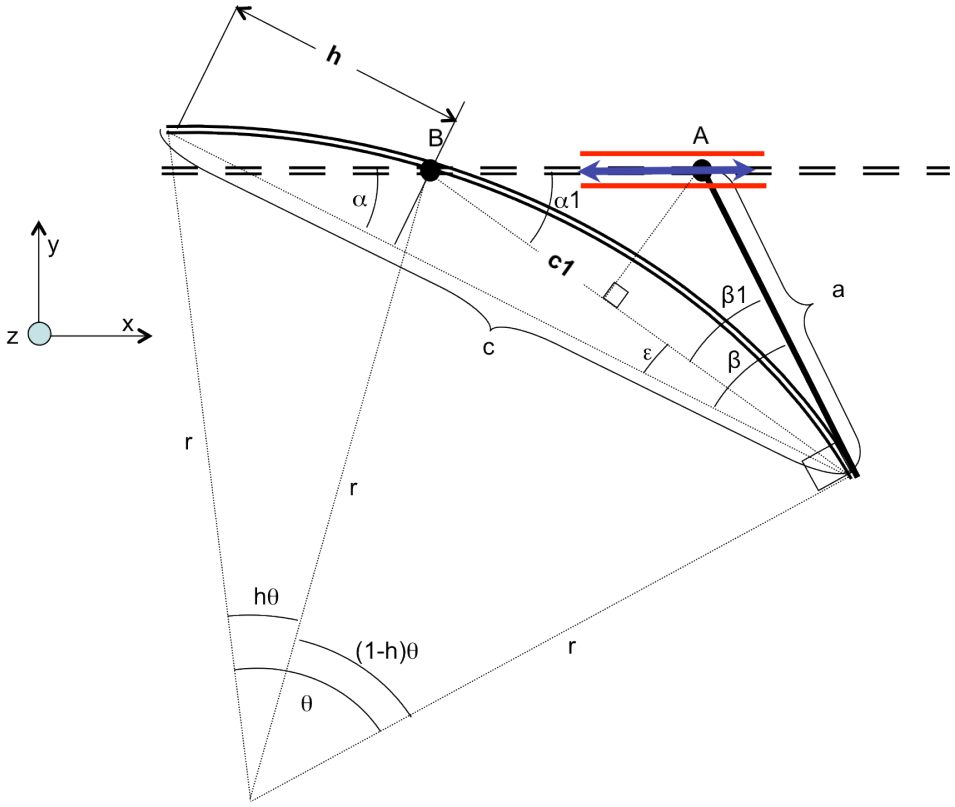

Figure 3.12: Cross section of the bimorph and linkage concept.

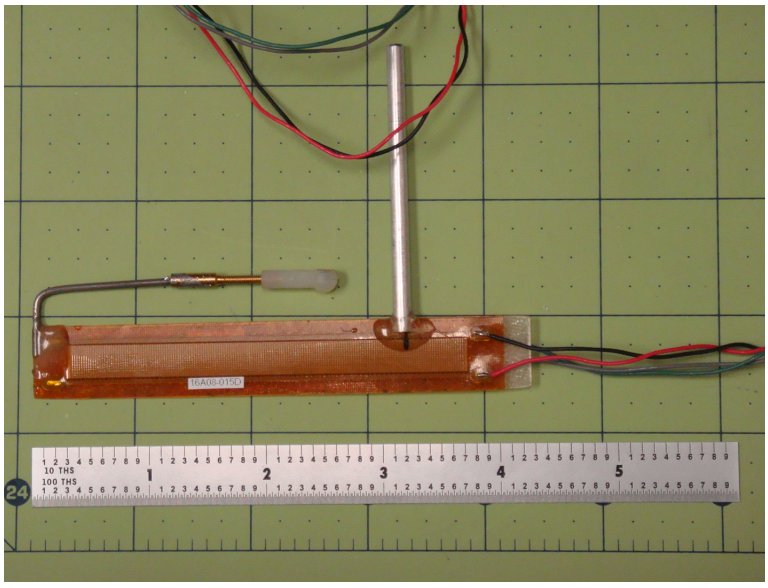

Figure 3.13: Picture of the small bimorph test element with attached axle and linkage.

In Figure 3.13, the axle was a small aluminum tube with approximately one-quarter inch outer diameter. A small slit was made in the end of the axle so that the bimorph fit in the slit. The axle is attached to the bimorph with epoxy. A wooden plate supported the opposite end of the axle, and a larger diameter aluminum tube is glued to the plate and is used as a bearing for the axle. A picture of the endplate is provided in Figure 3.14.

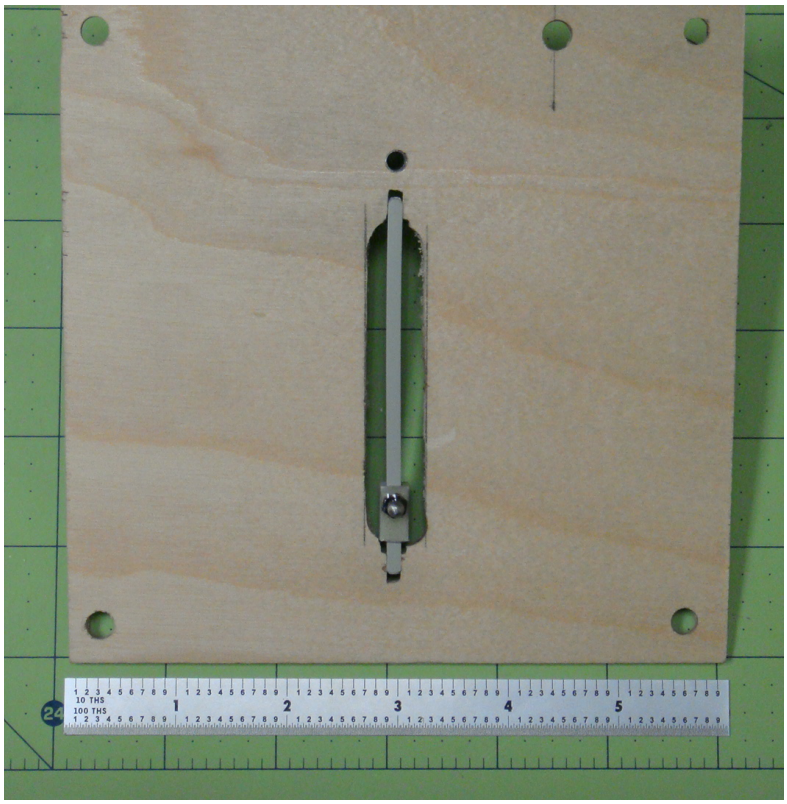

Figure 3.14: Picture of the endplate used for the bimorph and linkage concept.

Recall that the bimorphs are used as control vanes for ducted fan vehicles. In ducted fan applications, the control vanes are traditionally located directly aft of the duct. This is better visualized in Figure 3.15. They are attached to the duct via the duct centerbody and endplates. The centerbody is structure that extends down beneath the fan and inside the duct. The endplates extend down from the ducts outer wall, and serve as second mounting point for the control vanes. The endplate is an integral part of the proposed system, because the endplates provide the slot for the linkage. In Figure 3.14, the bearing for the vanes axle is located just above the slot. Here, the red lines in Figure 3.12 represent the slot, the small black ball joint represents point *A*, and the axle bearing represents point *B*.

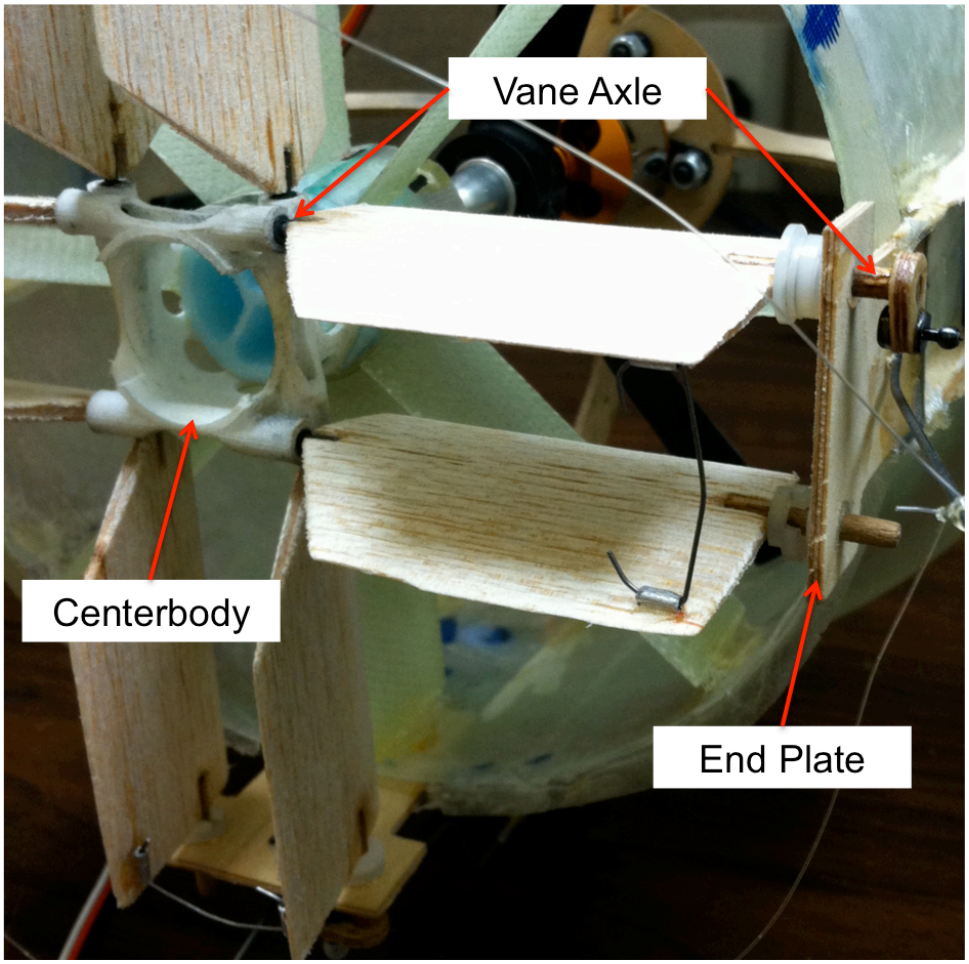

Figure 3.15: Picture showing the centerbody, control vanes, and endplates of a ducted fan vehicle to illustrate how the vanes are connected [55,56].

Last, the linkage is shown attached to the bimorph's trailing edge in Figure 3.13. The linkage is represented by the length *a* in Figure 3.12. Here, the linkage is made of spring steel (commonly know as music wire), and was glued to the trailing edge of the bimorph. The linkage is attached to the bimorph so that it remains tangential to the curvature of the bimorph at the TE. The opposite end of the linkage is connected to the endplate at *A*. This end of the linkage is constrained so that it can only translate via the slot in the endplate. It is the translation of point *A* inside the slot that allows the bimorph to change angle of attack during morphing. The combined bimorph, linkage, and endplate are shown in Figure 3.16. Notice the resemblance between Figure 3.12 and Figure 3.16 and that the linkage remains tangential to the curvature of the bimorph.

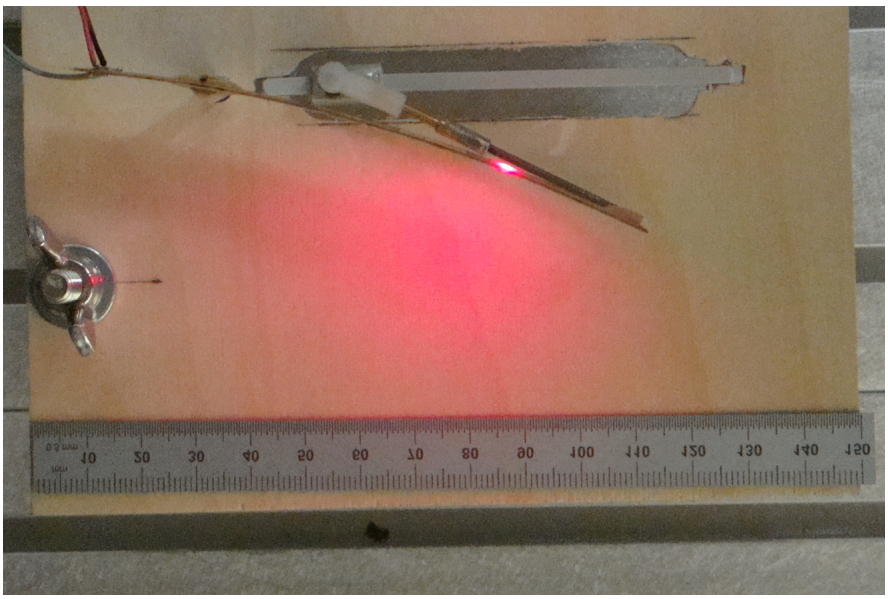

Figure 3.16: Picture of the fabricated bimorph and linkage concept with the endplate.

An example of how the bimorph and linkage work together is as follows. The bimorph will morph as shown in Figure 3.16 when voltage is applied to the MFC elements. The linkage (a) must remain tangential to the curvature of the bimorph at the trailing edge. So, as the vane morphs, the linkage end (A) must slide in the slot, moving in the positive x direction. Because the linkage has a fixed length a, the vane is constrained to rotate about its axle B. The linkage length a and the location of the bimorphs axle B can be changed to affect the amount of angle of attack that is achieved over the range of morphing. This is discussed further in the following subsection.

3.3.2 Bimorph and Linkage Geometry

In the following, kinematics relationships are derived that show how the thin bimorph and linkage behave in unison. These kinematics relationships are extended from those derived in Section 3.2.2. The assumptions taken in the previous derivations are restated here.

1. Morphed shape of the bimorph is approximately a circular arc
2. Camber change remains small enough that chord length remains unity, or $c \approx 1$
3. The linkage (a) is attached to the TE of the bimorph so that it remains tangential to the curvature of the bimorph at the TE

In Chapter 5, the author shows through experimentation the validity of the circular arc assumption.

The desired equation relates the change in angle of attack to the bimorph's change in camber. Using Figure 3.12, the following equations can be written from trigonometric relationships. By visual inspection, the first relationship can be made for the angles β and β1.

$$\beta = \frac{\theta}{2}$$
$$\beta 1 = \frac{(1-h)\theta}{2}$$

Equation 3-VII

Recall the assumption that the morphing is small, such that the chord length *c* and the arc length remain approximately equal. This assumption means that the length *h*, the distance of the axle *B* from the leading edge of the bimorph, remains the same distance. Again, recall that *h* was selected to be at the quarter chord location for the test element.

Next, because the linkage *a* is tangent to the trailing edge, the length c_1 is defined as the following.

$$c_1 = 2r \sin(\beta 1)$$

Equation 3-VIII

Given c_1 and using trigonometry rules for right triangles, the equation for α_1 is derived, which is given in Equation 3-IX.

$$\tan \alpha_1 = \frac{a \sin \beta 1}{c_1 - a \cos \beta 1}$$

Equation 3-IX

Last, the angle ε is written as the difference between β and β1. Given ε and Equation 3-IX, the angle of attack is written as that given below.

$$\alpha = \alpha_1 - \epsilon$$

Equation 3-X

To compare the bimorph and linkage combination to the results provided in Figure 3.10, the angle of attack must be written in terms of the bimorphs camber. This is first done by substituting Equation 3-VII into Equation 3-II, which results in the following.

$$2\eta = 180 - \beta$$

Equation 3-XI

Then, substituting Equation 3-I into η results in the following.

$$\beta = 180 - 2\tan^{-1}\left(\frac{0.5}{y}\right)$$

Equation 3-XII

Finally, substituting Equation 3-XII into Equation 3-IX results in the final equation with the angle of attack written explicitly as a function of camber.

$$\alpha = \tan^{-1}\left(\frac{a\sin\beta 1}{c_1 - a\cos\beta 1}\right) + 2\tan^{-1}\left(\frac{0.5}{y}\right) + \frac{(1-h)\theta}{2} - 180$$

Equation 3-XIII

It should also be noted that the angle of attack is dependent on the linkage length a and the axle location h. As mentioned earlier, these values are design parameters and can be varied to achieve the desired amount of angle of attack for a known range of morphing.

Figure 3.17 provides a plot of angle of attack versus change in camber for varying axle locations (*h*) and linkage lengths (*a*). Both values are normalized over the chord length of the control vane. So, *h* = 0.25 means that the vane axle *B* was located at the quarter chord, and *a* = 0.5 means that the hinge is half the chord length. The plot of angle of attack change for morphing only (Figure 3.9) is plotted again to show the theoretical benefits of adding the linkage.

According to Figure 3.17, as the linkage length *a* gets larger, the values of achievable α also become larger. Furthermore, moving the axle toward the trailing edge also has positive effect on angle of attack. But, there are physical limits that bound the maximum values of *h* and *a*. Specifically, the combination of *h* and *a* must satisfy the following inequality, which simply states that the linkage and vane axle cannot impact one another.

$$a \geq c - h$$

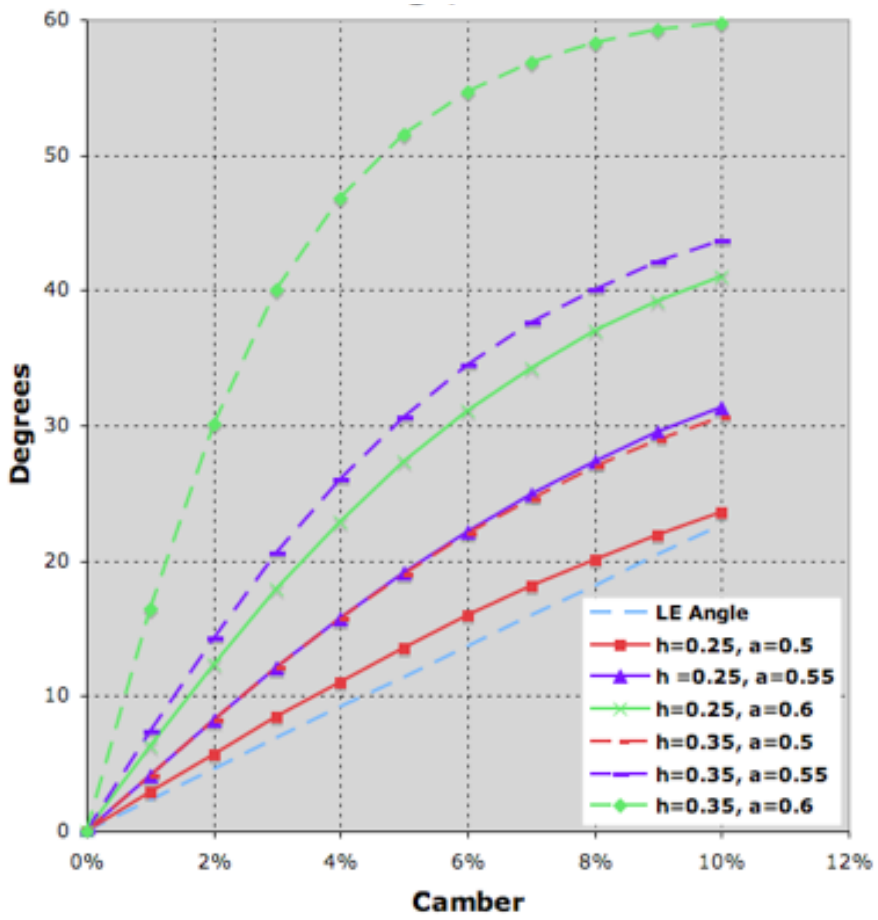

Figure 3.17: Plot of Angle of Attack (α) versus Camber.

3.4 Airfoil Test Elements

Two Selig airfoil test elements were also used during the course of this thesis. The specific airfoil section was a Selig S1210. The airfoils were originally built for wind tunnel testing, but were also used for frequency response testing during this research. The first of the two test elements was standard airfoil section with a 30% trailing edge flap. The flap is driven by a servo that was embedded in the airfoil. The servo driven airfoil test element is shown in Figure 3.18.

The second of the airfoil test elements changes camber by utilizing bimorphs (Section 3.2) bonded to its upper surface. Unlike the servo-actuated airfoil, this airfoil has a rigid leading edge, while the aft 65% of the airfoil is hollow and flexible. This airfoil was fabricated so that the un-morphed (neutral) shape of the airfoil was the Selig S1210 airfoil. Figure 3.19 depicts the bimorph actuated airfoil test element. As is shown, two bimorphs are bonded to the upper surface of the airfoil. Specifically, the

85x28mm active area bimorphs are used. Actuating the bimorphs causes the airfoil to increase or decrease camber.

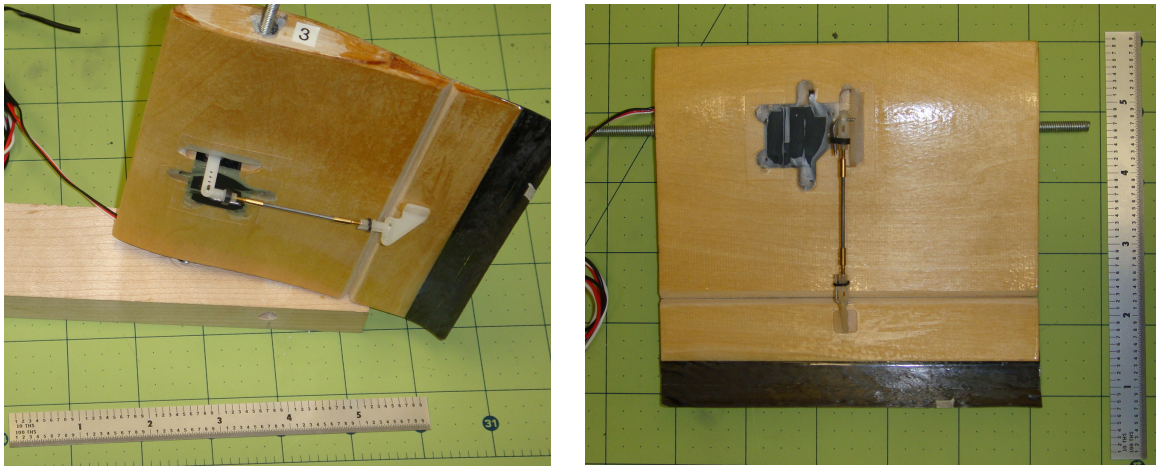

Figure 3.18: The servo-actuated Selig S1210 airfoil test element.

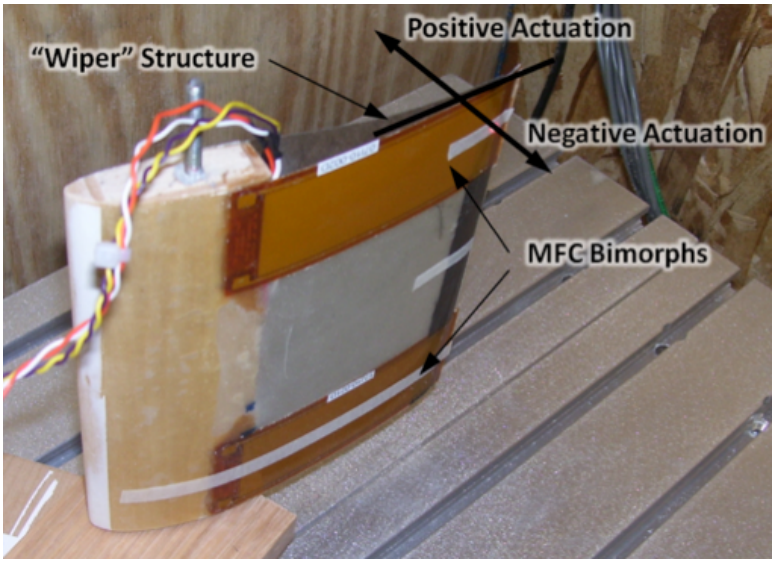

Figure 3.19: The bimorph actuated Selig S1210 airfoil test element.

In the remainder of this section, the two test elements mentioned above are discussed in better detail. First, the servo-actuated airfoil is discussed, along with a description of the specific servo that was used. This is followed by a discussion of the bimorph-actuated airfoil.

3.4.1 Servo-Actuated Airfoil Details

The servo-actuated airfoil is shown in Figure 3.18. This airfoil is made of wood that was cut using a Computer Numeric Controlled (CNC) mill. Two threaded rods protrude

from each end of the test element, which are used for mounting in a wind tunnel. The entire airfoil was cut at the same time, and the flap was fabricated as a post process. A single ply of fiberglass (1.4 oz./sq. yard) was bonded to the upper surface of the airfoil to function as the flap's hinge. Then, some wood on the bottom surface of the airfoil was removed to create the joint, allowing the flap to rotate. This hinge line cutout is shown in Figure 3.18. Last, the trailing edge of the S1210 was too thin to cut from wood, so carbon fiber was added to make up the aft portion of the trailing edge.

Another cutout was made in the bottom surface of the airfoil to embed the servo. Specifically, the servo is a Futaba S3156, and is shown in Figure 3.20. The servo-actuated airfoil section is only used for frequency response testing in this research, which is discussed in Chapter 6. As mentioned in Chapter 1, a goal of this research is to compare the performance of bimorph-actuated systems with servo-actuated systems.

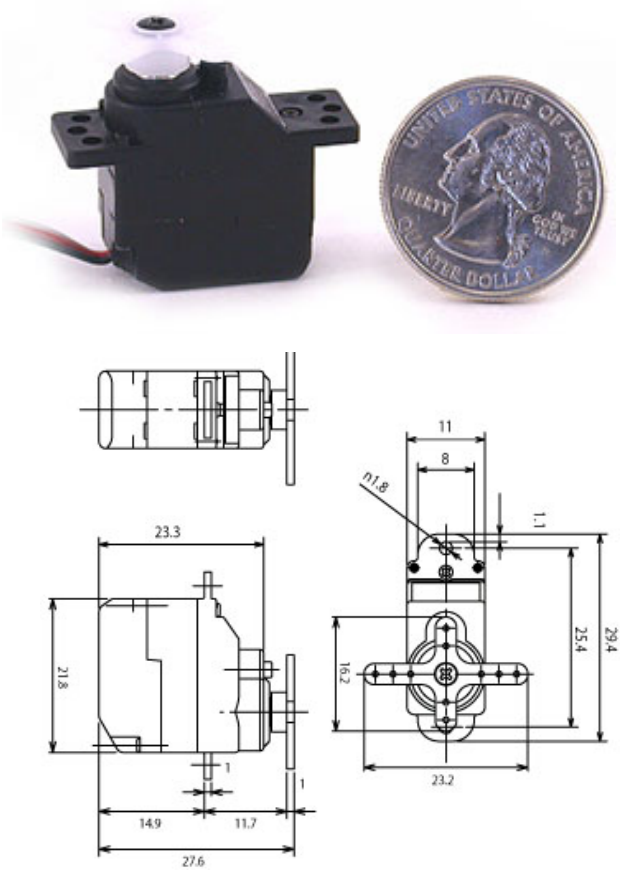

Figure 3.20: (Top) Futaba S3156 Servo with a U.S. quarter for size reference. (Bottom) 3-view of the Futaba S3156 servo with dimensions in millimeters. Image credit to ServoCity (http://servocity.com/).

3.4.2 Bimorph-Actuated Airfoil

The bimorph-actuated airfoil is shown in Figure 3.19. As mentioned earlier, two bimorphs are bonded to the upper surface of the airfoil and cause the airfoil to increase or decrease camber. The neutral position of its cross section is the Selig S1210 airfoil. As mentioned earlier, the aft portion of the airfoil is hollow. The top surface is composed of 2 plies of 1.4oz/sq. yard fiberglass. The bottom surface (wiper) consists of 1 ply of the fiberglass, and 1 ply of carbon fiber mat. The carbon fiber mat is essentially a thin layer of carbon fiber wool, as opposed to the standard woven or unidirectional carbon fiber cloth. Also, note that the upper and lower surfaces of the airfoil are not connected at the trailing edge. This allows the airfoil to change camber by morphing without any hindrance from the lower surface. This is better visualized in Figure 3.21.

Figure 3.21 shows both the positive and negative morphing conditions for the airfoil. As shown, the wiper surface does not extend all the way to the trailing edge of the airfoil. When the upper surface increases camber, the bottom surface is forced to bend down. The bottom surface is fabricated so that its trailing edge remains in contact with the upper surface for all bending conditions. Again, the bottom surface is not connected to the upper surface so that the airfoil changes camber freely.

Now that the different hardware and test elements are known, the following chapter describes some of the steady state experiments performed on the bimorphs. As is discussed, the bimorph is given a fixed voltage and its resulting morphed shape is measured. The results of these tests show the amount of hysteresis that the bimorphs exhibit. Furthermore, these tests provide a proof of concept for the linkage and bimorph element.

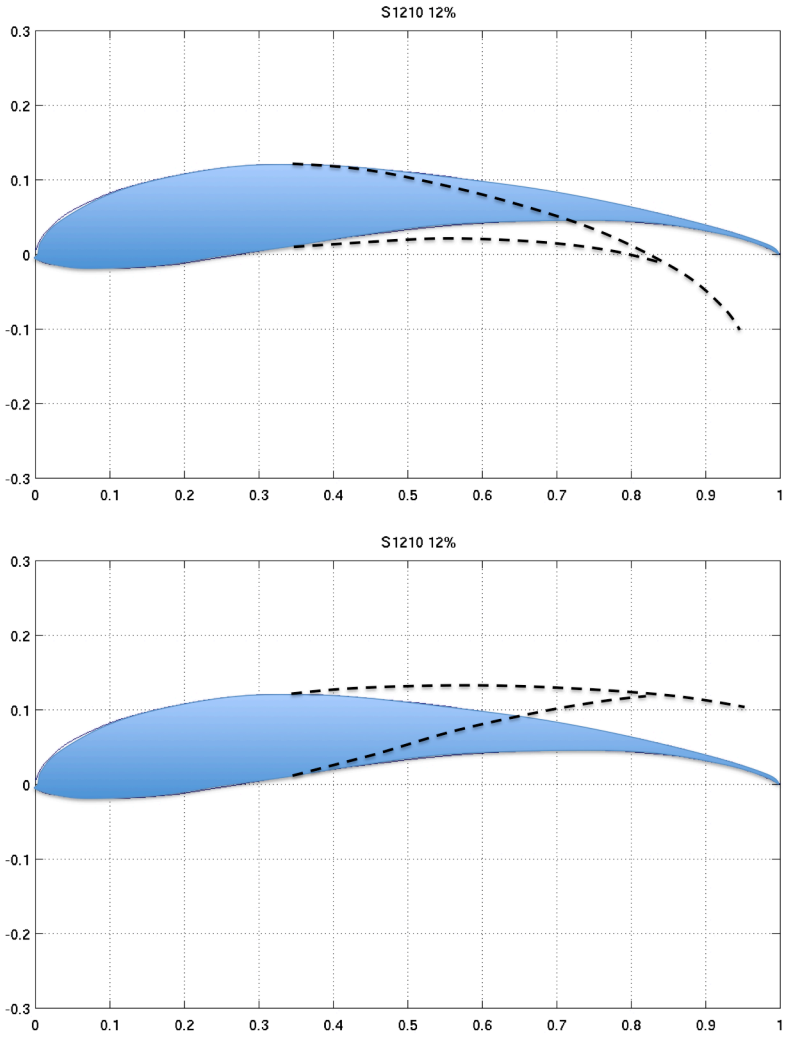

Figure 3.21: Sketch of the morphing Selig airfoil cross-section to visualize the upper and lower surface interactions. (Top) Positive morphing condition for increasing camber, (Bottom) negative morphing condition for decreasing camber.

4. Steady State Experiments

Two different types of experiments were conducted during this research: experiments that measured the steady-state shape of the test elements, and experiments that measured the dynamic response of the test elements. This chapter discusses experiments that were performed to characterize the steady-state response of the test elements. The specific test elements used for the steady-state experiments were the two bimorphs described in Chapter 3. It should be noted that this chapter is only intended to describe the experiment and test procedure, and the results are provided in Chapter 5. Two experiments were performed. The first measured the hysteresis exhibited by the small bimorph element (Chapter 3). The results from this experiment also allowed the author to check the validity of the assumptions made to derive the geometric relationships in Chapter 3. The second experiment was performed as a proof of concept test for the bimorph and linkage combination.

The first experiment was a bench test of the small bimorph that was described in Chapter 3. The small bimorph is the 85x14mm active area bimorph, and is referred to as the small bimorph throughout this thesis. Here, bench testing implies that the tests are performed in a no-load configuration. Therefore, no external loads or moments were acting on the bimorph. The author desired to characterize the hysteresis exhibited by the bimorph, and to characterize the morphed shape of the bimorph. Recall from Chapter 3 that the morphed shape is assumed to be a circular arc.

The second experiment is a bench test conducted to analyze the bimorph and linkage combination, also described in Chapter 3. This test serves as a proof-of-concept test for the bimorph and linkage, and answered the question, "*Are the geometric relationships viable based on the assumptions made in Chapter 3?"* Through this test, observations are made about how the hysteresis of the MFC is amplified by the linkage. Lastly, this experiment sheds light on any problems that are present in the bimorph/linkage and linkage/endplate interactions.

4.1 Small Bimorph Bench Test

As mentioned above, this experiment is a bench test of the small bimorph element. The test element used for this experiment is described at length in Chapter 3. Figure 4.1

provides a picture of the bimorph element during testing. This experiment provides knowledge about the following attributes of the bimorph:

1. Quantify the Trailing Edge (TE) deflection due to morphing
2. Characterize the hysteresis exhibited by the bimorph
3. Characterize the morphed shape of the bimorph (circular arc)
4. Determine the amount of overshoot necessary to zeroize the bimorph

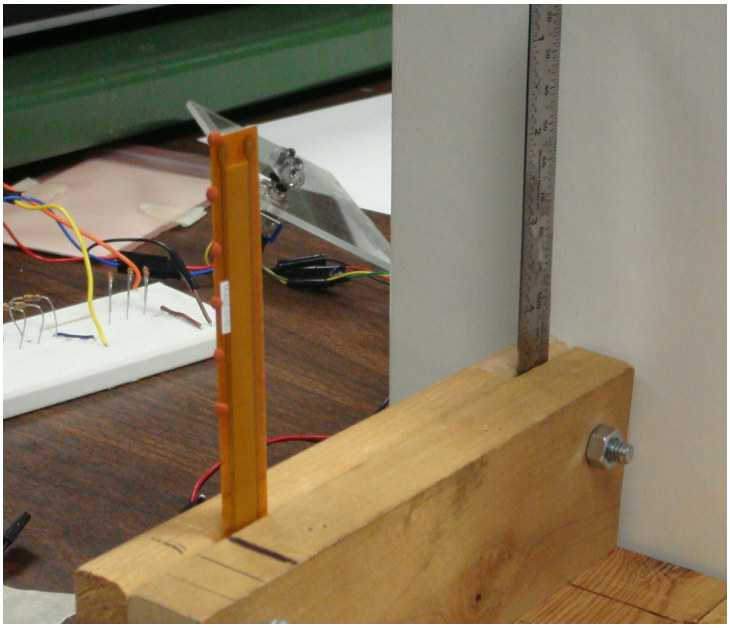

Figure 4.1: Small bimorph clamped in a vise during steady-state testing.

The above list merits further discussion. Item 1 is directly related to an example given in Chapter 3. Assuming that the Leading Edge (LE) of the bimorph is fixed, applying voltage causes the TE to deflect. This deflection leads to a change in angle of attack for the bimorph, which is defined as a function of camber in Chapter 3.

Item 2 mentions the hysteresis that is exhibited by the bimorph, which is caused by the hysteresis in the individual MFC elements. Understanding the hysteresis exhibited by the bimorph is crucial to being able to precisely control the bimorph. Consider the following example. The angle of attack depends on the TE deflection of the bimorph, and the deflection is a hysteretic process. Therefore, the angle of attack is also hysteretic. Without sufficient modeling or feedback, the TE deflection is unknown in open-loop operation. A hysteresis model is formed by using empirical data from deflection measurements.

Item 3 mentions characterizing the morphed shape of the bimorph. In Chapter 3, the researcher provides the kinematics equations that describe the morphed shape of a bimorph element. One of the underlying assumptions is that the morphed shape of the element is a circular arc. By taking measurements of the morphed shape of the bimorph, the validity of these assumptions is tested.

Last, item 4 mentions zeroing the bimorph. Again, recall that the TE deflection is a hysteretic process. Even when no voltage is applied to the bimorph, it can still have a non-zero TE deflection. Therefore, voltage is applied to drive the bimorphs trailing edge to zero. For this experiment, it is desired to know how much *voltage overshoot* is required to bring the TE deflection to zero.

From the above paragraphs, two different tests are described to answer the questions posed in the list:

1. Measure the hysteresis exhibited by the bimorph element by measuring the TE deflection and input voltage
2. Determine the amount of overshoot voltage required for TE deflection to be zero.

4.1.1 Equipment and Initial Setup

Figure 4.1 shows the small bimorph test element clamped in a wooden vise. Small pieces of clay are located along the edge of the bimorph at half-inch increments and are used as markers for an image processing software. A straight edge is also shown in the vise behind the bimorph to provide a vertical reference line. This allows the TE deflection to be measured as a displacement from vertical. The white background is used so that the image processing software could easily distinguish the markers, and a web camera recorded video of the bimorph element. The web camera records video at the standard frame rate of about 30 frames per second (fps), which was later reduced to 10fps to reduce the image processing time. This process is discussed more thoroughly in the following chapter.

Figure 4.2 provides a picture taken during the experiment and captures all of the equipment used to conduct the experiment. The equipment on the green table is a power supply (upper left corner), a multimeter (yellow), and a Trek amplifier (black). The

power supply provides the voltage input to the amplifier (0 to 5 volts DC). The amplifier receives a 0 to 5V input, and magnifies the signal up to 1500V. The gain on the amplifier was set so that its output was 1400V for a 5V input signal; allowing a 100V margin so that the bimorph was not supplied with too much voltage. A dial was used to manually change the voltage input to the amp. The multimeter measures the input voltage to the amplifier to ensure that no more than 5 volts are input to the amp. Therefore, no more than 1400V is input to the MFC element.

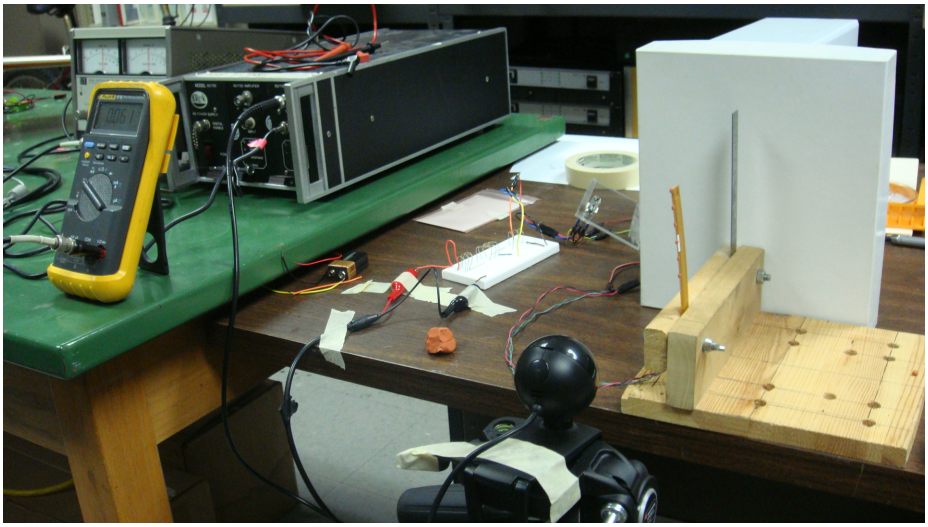

Figure 4.2: Equipment setup during the small bimorph steady-state testing.

Recall from Chapter 3 that for a bimorph to achieve maximum bending, the top MFC element is supplied 1500 volts while the bottom element is supplied -500V. The voltages are then swapped to achieve bending in the opposite direction. Therefore, a high channel and a low channel are required, along with a way to switch the channels between the upper and lower MFC. With the high voltage channel supplied by the amplifier, a voltage divider circuit was built to obtain the low voltage channel (Figure 4.3). Essentially, the circuit splits the amplifier output into two signals with a common ground.

In Figure 4.3 (left), electricity is thought flow from left to right in the picture. Starting in the upper left, the input voltage (red) comes from the amplifier output. In the lower left, the ground channel is connected to the circuit board (brown). The combination of *red* and *brown* make up the high voltage channel. The high voltage channel is passed through the circuit, and leaves the circuit on the right via the *red* and *black* wires (upper right and lower right, respectively).

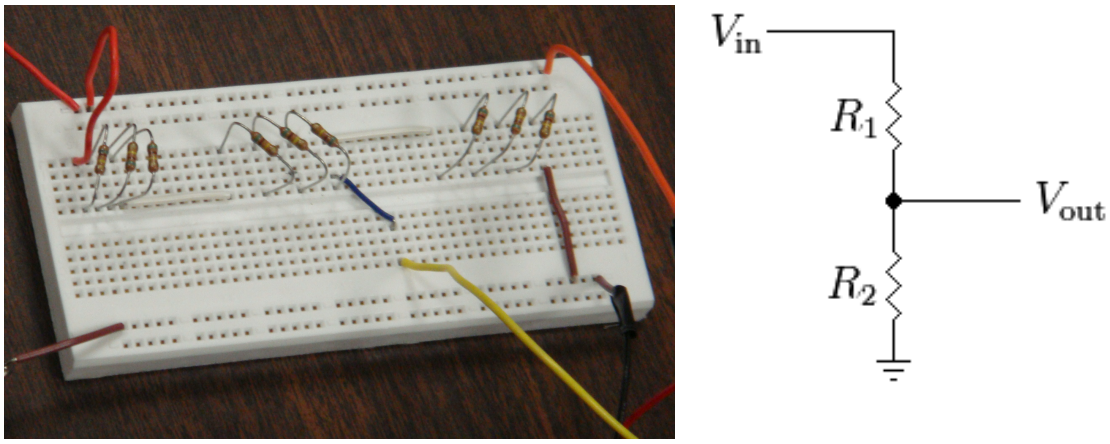

Figure 4.3: (Left) Picture of the voltage divider used during the steady state experiments. (Right) Schematic of a voltage divider circuit.

Nine resistors are wired in series in the middle of the circuit board. Each resistor in the circuit has the same resistance value. Therefore, each resistor reduces the voltage by one ninth, or approximately 11.1%. Each set of three resistors reduces the voltage by one third (33.33%). Tapping into the circuit after the second set of resistors forms the low channel, where the high voltage channel is reduced by 66.6%. With this circuit, when the high channel voltage is 1400V, the low channel output is 467V.

Once the high and low channels were present, the next step is to route these signals to the individual MFC elements of the bimorph. To do this, the switch shown in Figure 4.4 is used. In the figure, voltage flows from top to bottom. The three-wire set at the top of the figure is the high and low channels, with a common ground wire. *Red* is again the high channel, *Blue* is the low channel, and *Black* is ground. At the bottom of the picture are two sets of wires, one set being the red/black wires, and the other is the green/yellow set. Each set of output wires go to an individual MFC element on the bimorph. The first position for the switch routes the high channel and ground to the red/black wire set. This position also flips the polarity of the low channel, and routes the low channel to the green/yellow wire set. The second position performs the opposite function. Thus, it routes the high voltage channel to green/yellow, and routes the low voltage channel to red/black. Thus, the switch provides the ability for the bimorph to easily actuate in both directions.

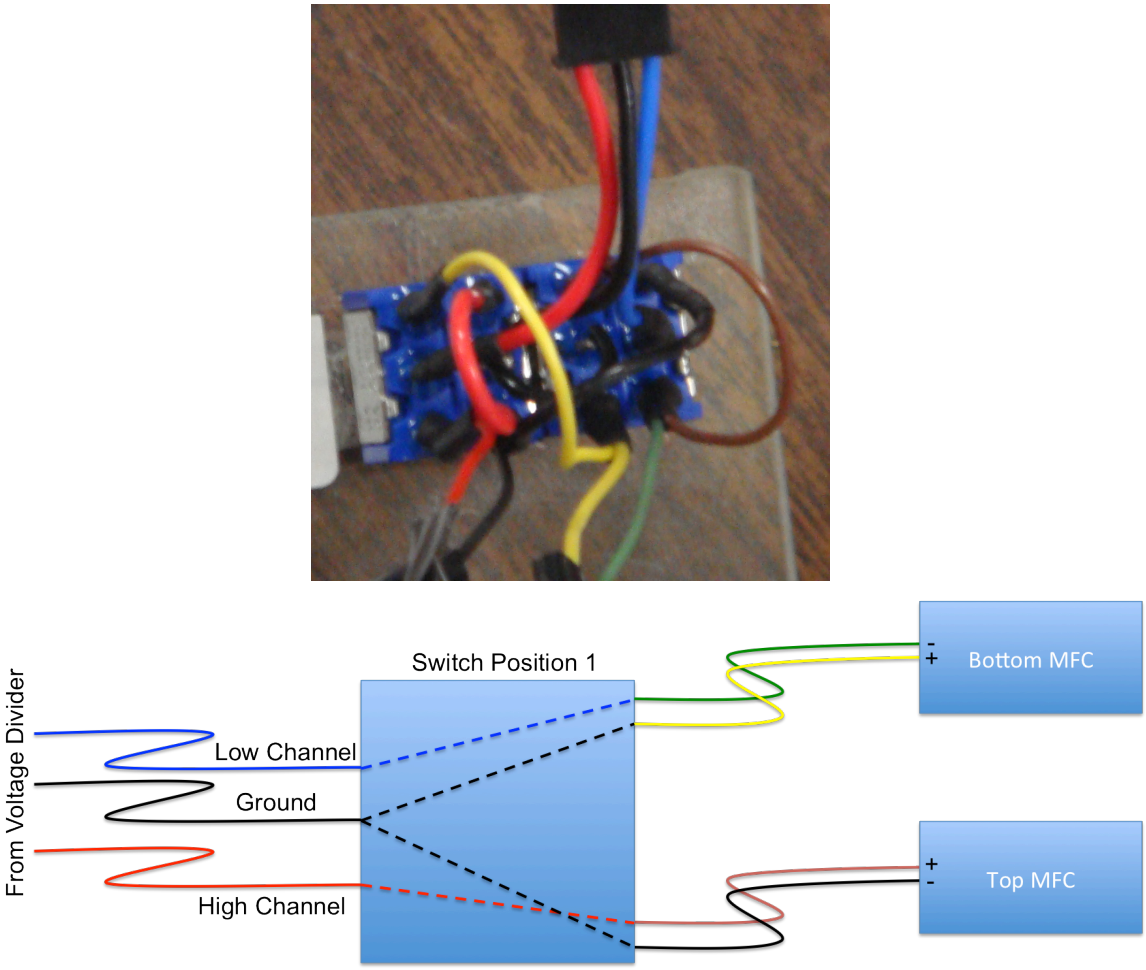

Figure 4.4: (Top) Two-position switch used to map the high and low voltage channels to the MFC elements on the bimorph. (Bottom) Schematic of the two-position switch depicting position 1 of the switch.

4.1.2 Hysteresis Experimental Procedure

Recall from above that two experiments are discussed. The first is an experiment to better understand the hysteresis exhibited by the small bimorph. The detailed procedure taken to perform this experiment is as follows:

1. Beginning with the bimorph test element in the vise at 0V, begin recording video, and apply +10% voltage increment to the element.
2. Allow a few seconds to record roughly 100 frames of video and apply another 10% voltage increment (now at 20% of max).
3. Repeat steps 1-2 until 100% input voltage (5V) is obtained, resulting in the maximum TE deflection of the bimorph element

4. After 100% voltage is obtained, apply -10% voltage increments until -100% voltage is obtained (*negative input voltage indicates position 2 of the switch*)
5. After -100% voltage is obtained, apply +10% voltage increments until 100% voltage is obtained once again. (full hysteresis loop is now completed)
6. Apply -10% voltage increments until 0% voltage is obtained.

4.1.3 Voltage Overshoot Experimental Procedure

As mentioned earlier, an experiment was conducted to determine the amount of voltage overshoot required to drive the bimorph's TE to zero deflection. The detailed procedure taken to perform this experiment is as follows:

1. Beginning with the bimorph test element in the vise at 0V, begin recording video and apply 100% voltage increment to the element.
2. Allow the video to capture roughly 100 frames at 100% voltage, then reduce the voltage back to 0%.
3. Again, allow a few seconds of video capture at 0%, and apply a -2% voltage increment to the element.
4. Continue applying -2% voltage increments until TE deflection has crossed the zero deflection mark. Allow a few seconds of video capture at each -2% voltage increment.
5. After crossing the zero deflection state, apply -100% voltage, and allow a few seconds of video capture.
6. Increase the voltage back to 0%, again allowing a few seconds of video capture at 0 voltage.
7. Add +2% voltage increments until TE deflection crosses the zero mark and the deflection becomes positive.
8. Repeat steps 1-7 except with voltage steps of ±50% rather than 100%.

4.2 Small Bimorph and Linkage Bench Test

Upon completing the tests described in Section 4.1, the small bimorph was retrofitted with a trailing edge linkage to build the bimorph and linkage test element. This process is described in Chapter 3, and Figure 4.5 shows the bimorph and linkage combination

during testing. In this section, an experiment is described that serves as a proof of concept test for the bimorph and linkage. Here, the author first desired to show that the bimorph and linkage concept would work as anticipated. This test also ensures that the kinematics relationships (Chapter 3) are an accurate representation of the test elements behavior. The following describes an experiment to answer the questions posed above.

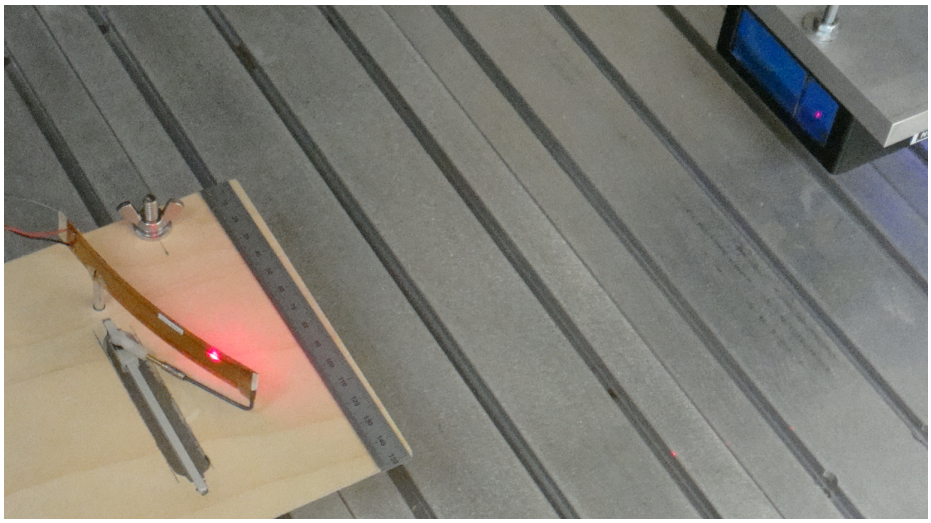

Figure 4.5: Picture of the fabricated bimorph and linkage test element taken during proof-of-concept testing.

Like the experiments described in Section 4.1, the experiments here are also bench tests. Furthermore, this experiment only shows that the bimorph and linkage interactions work, and only steady-state data is presented. It should also be noted that this experiment used better experimental and measurement techniques than those described in Section 4.1. Specifically, a laser measurement unit measured the deflection of the bimorph. Unfortunately, this equipment was not available at the time that the first experiment was performed.

The experiment discussed here is intended to answer some questions concerning the bimorph and linkage concept's performance. Specifically, the questions are as follows:

1. Quantify the Trailing Edge (TE) deflection
2. Characterize the hysteresis exhibited by the bimorph and linkage system
3. Determine the amount of angle of attack that the bimorph can achieve with the linkage

The first item is to quantify how much trailing edge deflection can be achieved by the bimorph and linkage system. If the system works as anticipated, the TE should

achieve much larger deflections than the cantilevered bimorph. Therefore, the bimorph and linkage also achieves larger angles of attack. The second item is about quantifying how the hysteresis in the bimorph affects the angle of attack. The desired relationship between input voltage and angle of attack is linear. However, the hysteresis exhibited by the bimorph will cause the input voltage and angle of attack relationship to be nonlinear. Finally, the third item lists the desire to quantify the maximum amount of angle of attack that is achievable by the bimorph based on the particular design. Recall from Chapter 3 that the linkage length and vane axel locations are design parameters. These values can be modified to achieve larger or smaller angles of attack.

4.2.1 Equipment and Hardware

Figure 4.6 provides a diagram of the equipment used during this experiment. Note that the picture depicts an airfoil as the test element. However, here the bimorph and linkage element was used. The same equipment setup depicted in Figure 4.6 is used for all of the subsequent experiments, and only the test element is different for each experiment.

First, a LabView program is used to command the input voltage to the bimorph and measure the output from the laser measurement unit. LabView sends command signals to the amplifying circuitry labeled AMPS MFC Driver Board in the figure. This circuitry was built for a separate research, and is intended to be a potential flight weight circuit board for UAVs to utilize MFC actuators. The circuit amplified the constant 12V DC signal to the high voltages required for the MFCs. The command signal is a 0-5V DC signal. Here, 2.5V input signal commands 0V to the MFC elements, and so the bimorph is in its neutral state. An input signal of 5V commands the bimorph to its positive 100% morphing condition, while a 0V input signal commands the bimorph to negative 100% morphing.

As shown in the figure, the bimorph is mounted in the bed of a CNC machine. The laser measurement unit is mounted to the gantry of the CNC machine, and measures the distance between it and the bimorph. The laser is also shown in Figure 4.5. To perform the experiment, a voltage input command is input to the amplifying circuitry, which sends the amplified signal to the bimorph. This causes the bimorph to morph to a new

steady state morphing condition. The laser measures the distances at discrete locations along the bimorphs length. This process is better visualized in Figure 4.5. The laser records deflection measurements at discrete locations along the bimorphs length, starting at the bimorph's leading edge and moving toward the trailing edge. The details of the experimental procedure are described in the following subsection.

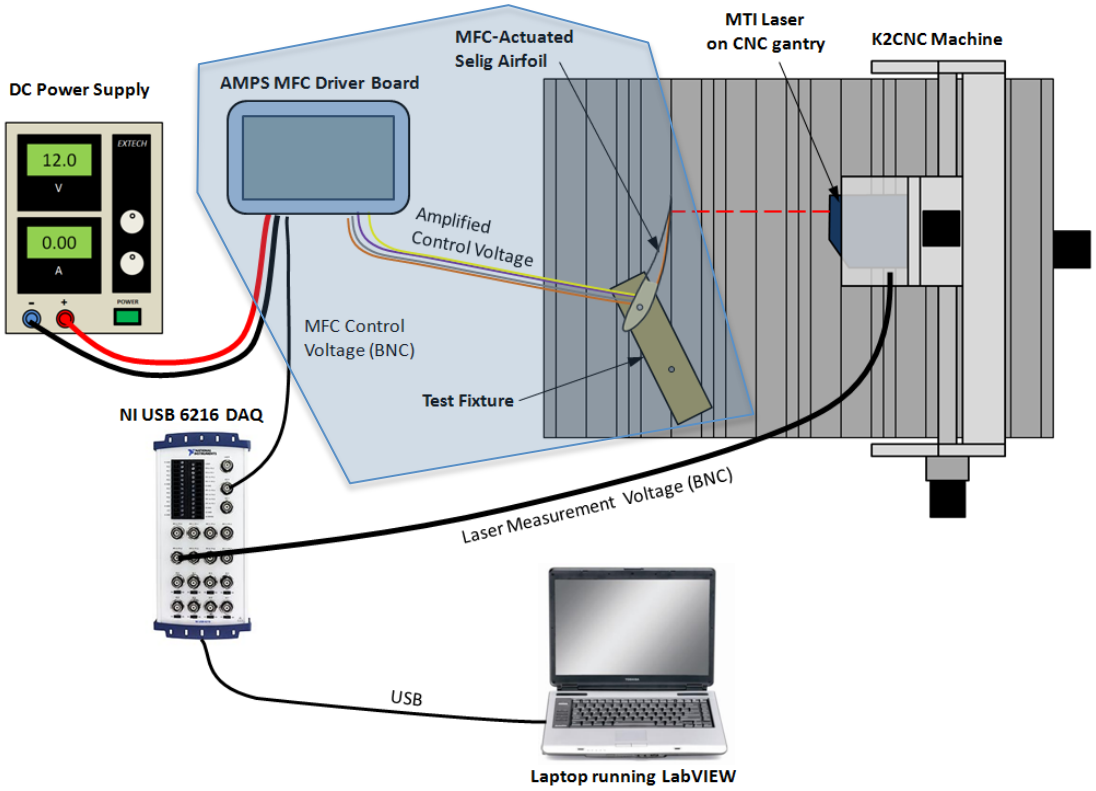

Figure 4.6: Equipment used during the bimorph and linkage bench test. Note that the test element depicted is not the bimorph and linkage, however the test setup is still the same.

4.2.2 Procedure

This subsection provides a detailed procedure for the experiment that was conducted for the bimorph and linkage combination.

1. First the bimorph and linkage test element was bolted to the bed of the CNC machine.
2. The laser measurement unit was attached to the CNC's gantry and was positioned so that the laser was focused near the leading edge of the bimorph.
3. The input signal to the bimorph was first set at 2.5V, which means that the MFC elements received 0V. Thus, the bimorph was at its neutral position.

4. The laser measured the distance between it and the bimorph's leading edge, then the CNC moved the laser toward the bimorphs trailing edge in 0.2 inch increments.
5. Step 4 was repeated until the laser had moved beyond the trailing edge of the bimorph.
6. Then the laser was moved back to its starting position at the leading edge of the bimorph, and the input voltage was incremented by 0.83V (a third of the morphing condition).
7. Steps 4-6 were repeated until 5V input was reached, resulting in the 100% morphing condition.
8. Then the voltage was decreased by 0.83V until 0V was reached (-100% morphing). At each morphing condition, the laser measured the distances between itself and the bimorph in 0.2 inch increments.
9. Finally, the voltage was increased back to 5V which completed the full hysteresis loop.

5. Steady-State Experiment Results

This chapter is devoted to discussing the results from the experiments described in Chapter 4. The results are presented in the same order as they were discussed in Chapter 4. First, the results from bench tests of the small bimorph are provided. In this section, four different results are provided. First, the bimorph's Trailing Edge (TE) deflection and hysteresis loop are provided. Then, the overshoot voltage required to obtain zero TE deflection is presented. Third, the circular fit of the morphed shape of the bimorph is presented. Finally, the cantilevered bimorphs angle of attack is presented.

Section 5.2 provides results from the bench test of the small bimorph and linkage concept. This test specimen is discussed in Chapter 3. Here, the trailing edge deflection and the measured angle of attack are both presented. The angle of attack for the bimorph and linkage concept is compared to the cantilevered bimorph to show the advantages of the linkage. Last, some observations made during testing are provided

5.1 Small Bimorph Bench Test

5.1.1 Hysteresis Loop

As described in Chapter 4, this test allows for better understanding of the hysteresis exhibited by a bimorph. Briefly reiterating the content from Chapter 4, the test element was placed in a wooden vice such that it was fixed at its leading edge and its trailing edge was free to deflect. Voltage was applied to the bimorph element and its morphing was recorded using a small camera. Figure 5.1 provides two pictures of the bimorph test element taken during this experiment. The video captured was post processed to track the clay dabs on the test element. LabVIEW was used to post process the video and measure the bimorphs TE deflection.

Here, the image processing software determines both the TE deflection of the morphed element, and determines the morphed shape of the element (*i.e.* circle fit). The software measures the distance between the clay dab at the TE and the straight edge. Specifically, the LabVIEW software counts the pixels between the straight edge and the clay. This process is shown in Figure 5.2. In the figure, the green boxes are created by the user and are bounding boxes. Thus, this tells the software where to look for the clay pieces. The red box is the area where the software thinks the pixel is located, and the red

cursor inside the box is the specific pixel. The bottom most box is used to define the leading edge (LE), while the top most box defines the TE.

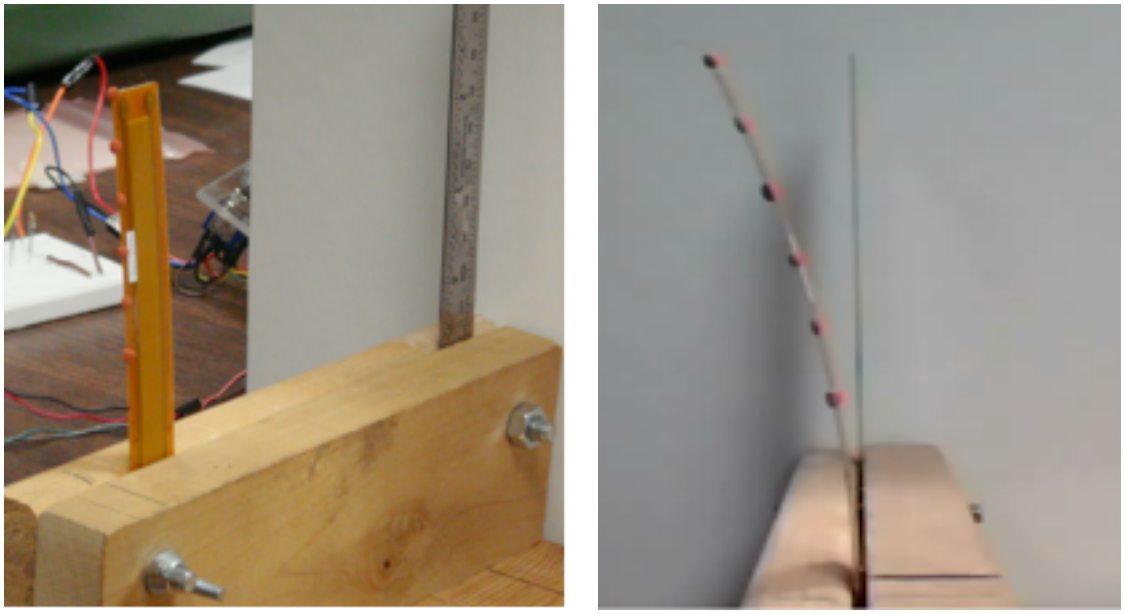

Figure 5.1: Cantilevered bimorph test element during steady-state experiments.

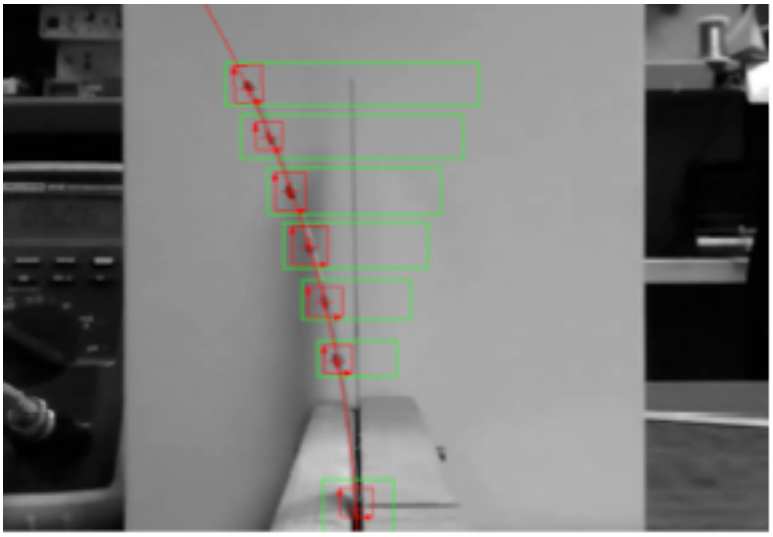

Figure 5.2: Screen Capture of the Image Processing Software to Measure the Distance between the TE (foreground) and the straight edge (background).

Figure 5.3 is a plot of the processed data taken from this experiment. The plot shows the measured TE deflection for input voltages from 0 to 5V (the rising side of the plot), and then from 5V back to 0V (the falling side). Recall that input voltages from 0V to 5V represent 0% and 100% morphing conditions for the bimorph. Likewise, negative 5V represents the -100% morphing condition. Recall that the data is collected at the standard

frame rate of 30 frames per second, but is down sampled to 10fps. The frames are down sampled to reduce the time required to process the data. LabVIEW processes each frame of data as discussed above. In Figure 5.3, the total number of frames shown is roughly 1650 frames, or roughly a video length of about 2 minutes and 40 seconds.

Also seen in the plot are plateaus in increments of about 60-90 frames. This is due to the experiment procedure. As described in Chapter 4, the input voltage was varied in 0.5V increments during the experiment. At least five seconds elapsed at each increment, resulting in the plateaus seen in the data.

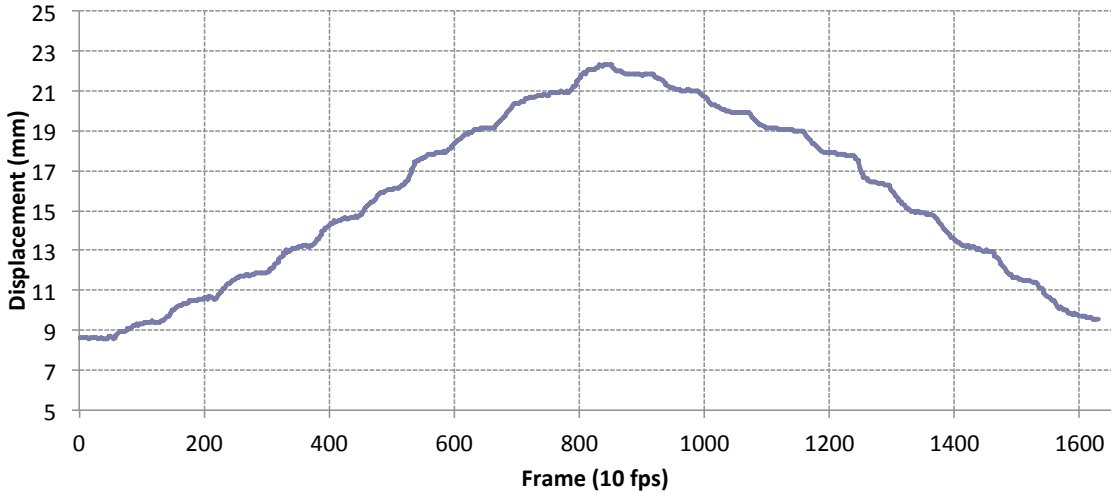

Figure 5.3: Trailing edge deflection of the cantilevered bimorph for 0V to 5V (rising section), and 5V to 0V (falling section).

Figure 5.4 shows the remainder of the collected data to complete the hysteresis loop. Here the input voltage varies from 0V to -5V (initial falling section), negative 5V to positive 5V (middle rising section), and finally 5V back to 0V. Figure 5.3 and Figure 5.4 show that the trailing edge deflection reaches a maximum of about 22 mm, while only reaching -10 mm for the -5V input case. The reason for the bias toward positive morphing conditions is not known, however, the author believes that the bias is due to the measurement techniques used.

The bimorph should deflect symmetrically about its zero morphing condition. The bias may have been caused by the camera's viewing angle during testing. For example, to get the best results, the camera must be aligned so that it is looking straight on at the bimorph and straight edge. Any movement to the left or right of the bimorph would

result in a bias like the one shown here. From this theory, the camera is viewing the bimorph from the left. Because the camera was aligned by sight, it is very likely this caused the bias shown in the data.

The data is averaged at each voltage increment in Figure 5.3 and Figure 5.4 so that a hysteresis loop is obtained. The hysteresis loop for the data is provided in Figure 5.5. Here, the *Legs* are broken down as follows: Leg 1 (0% to 100%), Leg 2 (100% to 0%), Leg 3 (0% to -100%), etc. The largest standard deviation from the averages is 0.25mm in the noisy areas shown in Figure 5.3 and Figure 5.4. The smallest deviation is 0.03 mm in the smooth plateaus, and the mean standard deviation is approximately 0.1mm.

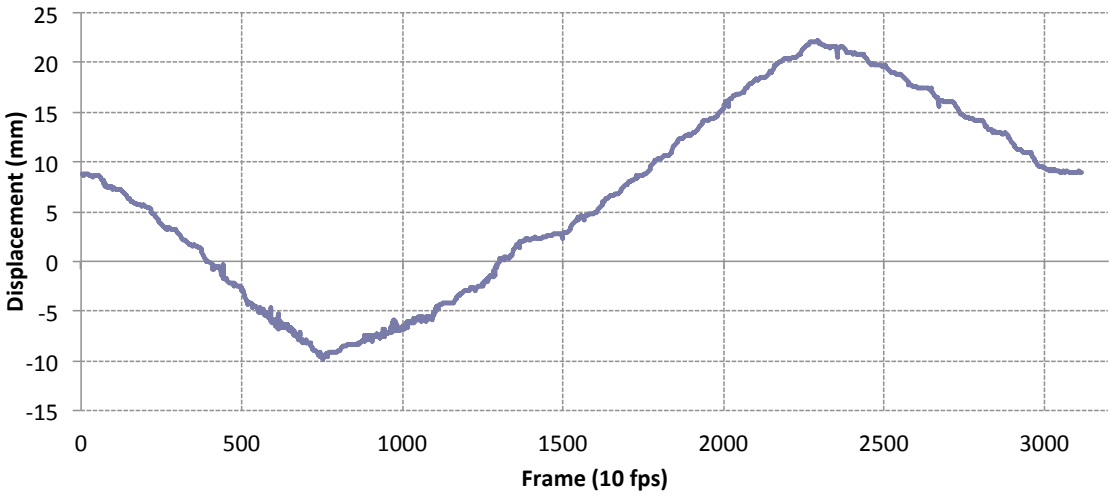

Figure 5.4: Additional trailing edge deflection of the cantilevered bimorph.

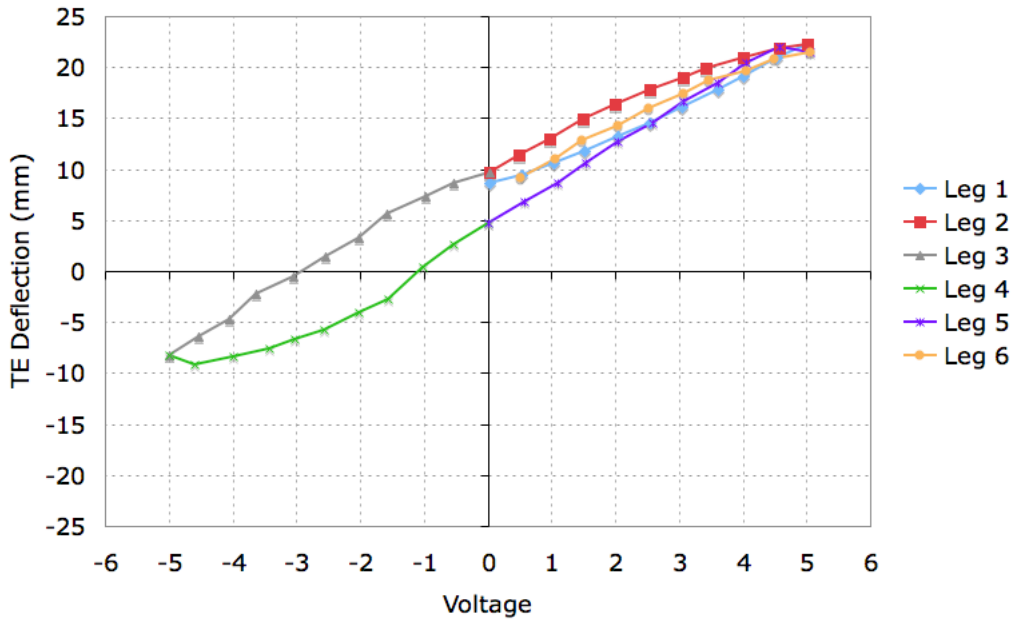

Figure 5.5: Hysteresis loop of the cantilevered bimorph show the relationship between TE deflection (output) versus input voltage.

5.1.2 Overshoot Voltage

It is easily noticed in the above plots that the bimorph element is biased toward the positive deflections (based on the axis system chosen). This is an undesirable effect, and must somehow be taken into account if a bimorph is to be utilized as a control surface. The major concern is that voltage must be added to the bimorph so that the zero deflection is achieved. To meet that end, a second experiment was devoted to measure the *overshoot voltage* required to reach zero TE deflection.

As described in Chapter 4, two tests were performed to measure the required voltage to reach zero TE deflection in the bimorph element. In the first test, the input voltage is ramped up to 5V (100% morphing condition), and then slowly ramped down to 0V. At zero input voltage, the TE is still at a non-zero deflection. So the voltage polarity was reversed to drive the TE deflection in the opposite direction. This effect is thought of as inputting negative voltage, causing the bimorph to morph in the opposite direction. The voltage is then incremented down from 0V until zero TE deflection occurred. The second test repeated this method, but with an initial ramp up to 2.5V instead of 5V.

The data recorded for the first test is shown below in Figure 5.6. Here, the initial peak in the data is the ramp up 5V. The voltage is then quickly ramped down 0V where

the polarity is switched at about frame 450. An input of -2.3V is required to achieve zero TE deflection, which is 46% of the total input voltage. This result agrees with the hysteresis loop in Figure 5.5. After achieving zero deflection, the input is ramped down to -5V (lower peak in Figure 5.6). The voltage is incremented up again (frame 2050 to the end) until the second zero crossing occurs. Here, zero TE deflection occurs at a relatively smaller input of -0.8V, or 16% of the maximum voltage. This result also agrees with the hysteresis loop in Figure 5.5, which shows the zero crossing (Leg 4) at about -1V.

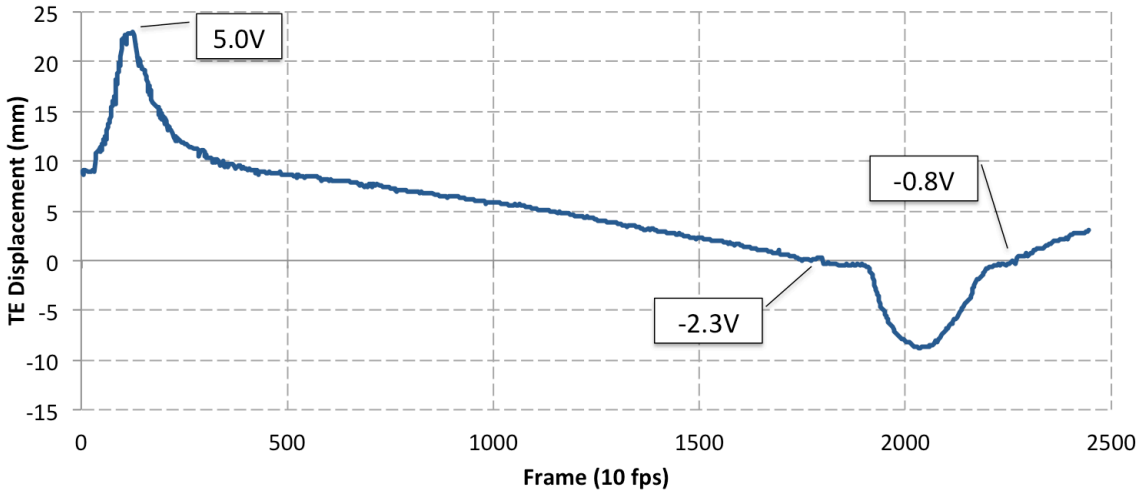

Figure 5.6: First test to determine the overshoot voltage necessary to reach zero trailing edge deflection for the bimorph.

The second test is a repeat of the first except that the peak voltages are 2.5V. This test determines the effect of the peak amplitude on the amount of over shoot voltage required to reach zero deflection. The recorded data from this test is shown below in Figure 5.7. As shown, the initial zero crossing occurs at nearly the same voltage as the first test (-2.05V), whereas the second zero crossing occurs at -1.1V. Though this test is only one data set, it shows that the amplitude of the peak voltage may have little effect on the amount of overshoot required to reach zero deflection.

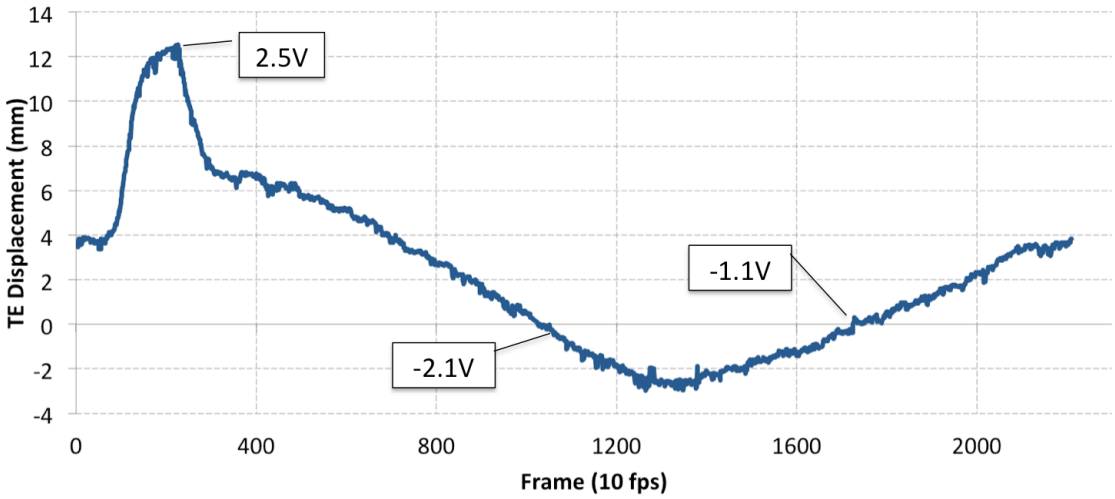

Figure 5.7: Second test to determine the overshoot voltage necessary to reach zero trailing edge deflection for the bimorph. This test was performed to determine if the initial actuation voltage would affect the amount of overshoot.

5.1.3 Circular Arc Assumption

The data from the hysteresis experiment is also used to determine if the bimorph's shape approximates a circular arc when morphed. Again, this is an assumption made in Chapter 3 for the derivations of the geometric relationships for the bimorph. This assumption is made so that the morphed shape of the bimorph is easily described by the geometry of a circular arc.

To perform this check, the image processing software was utilized to fit a circle through the clay markers placed along the bimorph element. This process is shown in Figure 5.8. Pixels are selected by the user, which in this case are the pixels made up by the clay markers. The green boxes are the expected areas for the clay dabs in each processed frame. The smaller red boxes show the location where the software finds the desired clay marker, and the cursor is the marker where the exact pixel is found.

Figure 5.9 and Figure 5.10 show the cases for TE deflection equal 0mm and the 0V input condition, respectively. Furthermore, Figure 5.11 and Figure 5.12 depict the 100% and -100% input voltage morphing conditions, respectively. Table 5.1 lists the circular fit parameters of each of the figures. Note that the deviation is the mean deviation of each clay marker from the circle fit. The table shows that the largest deviation is about 0.5 mm. The largest relative error in the measured data is 0.11%, which occurs at the

100% input voltage condition in Table 5.1. This result is expected because it should best approximate a circle at low input voltages and low morphing conditions (*i.e.* where the radius is largest).

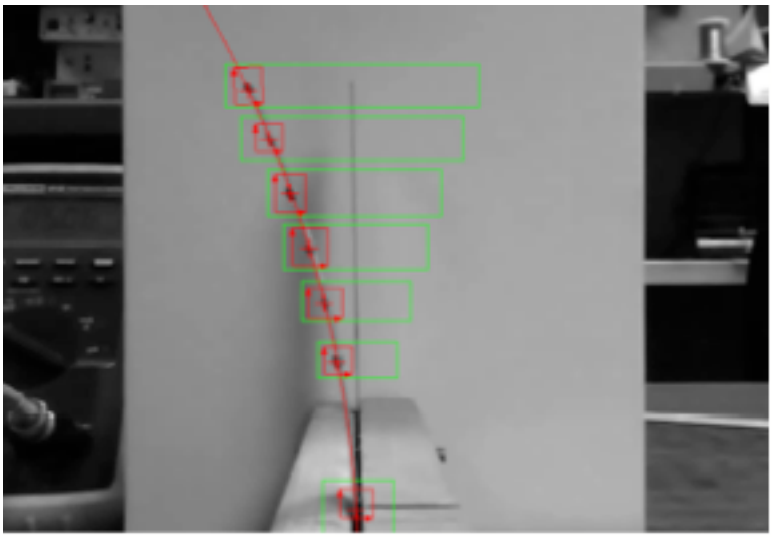

Figure 5.8: Screen Shot of the Point Tracking Software.

Table 5.1: Data for Circular Fit Parameters for the Deflected Bimorph Element.

Figure	Morphing Condition	Radius	Deviation
Figure 5.9	0% Morphing	1108.54 mm	0.15 mm
Figure 5.10	0% Voltage	727.67 mm	0.49 mm
Figure 5.11	100% Voltage	245.49 mm	0.27 mm
Figure 5.12	-100% Voltage	277.4 mm	0.27 mm

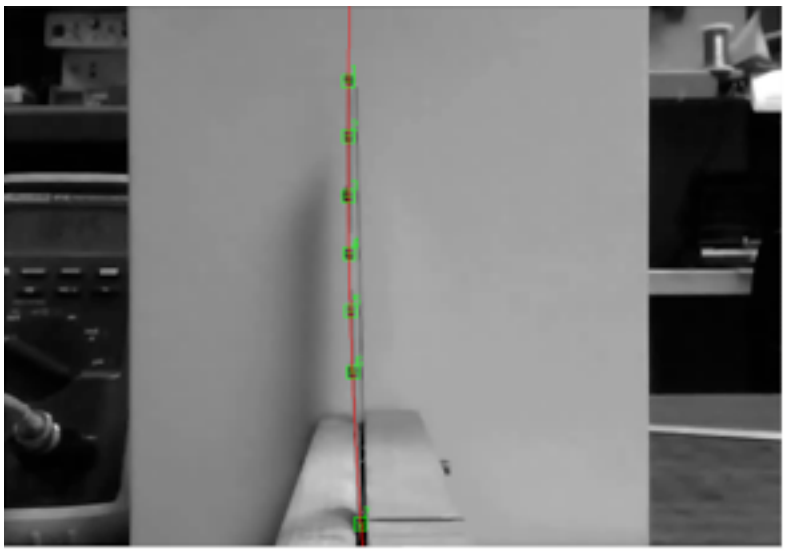

Figure 5.9: 0mm TE deflection morphing condition with image processing depicting the circle fit to the clay dabs.

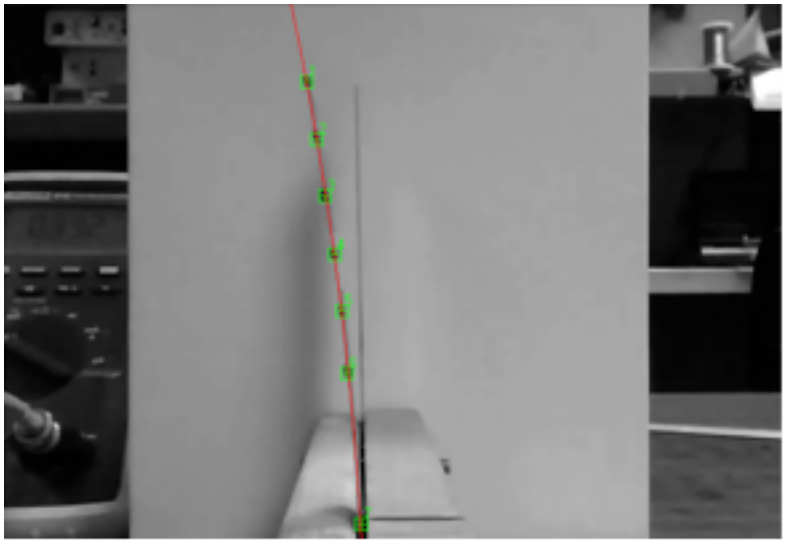

Figure 5.10: 0% morphing condition with image processing depicting the circle fit to the clay dabs.

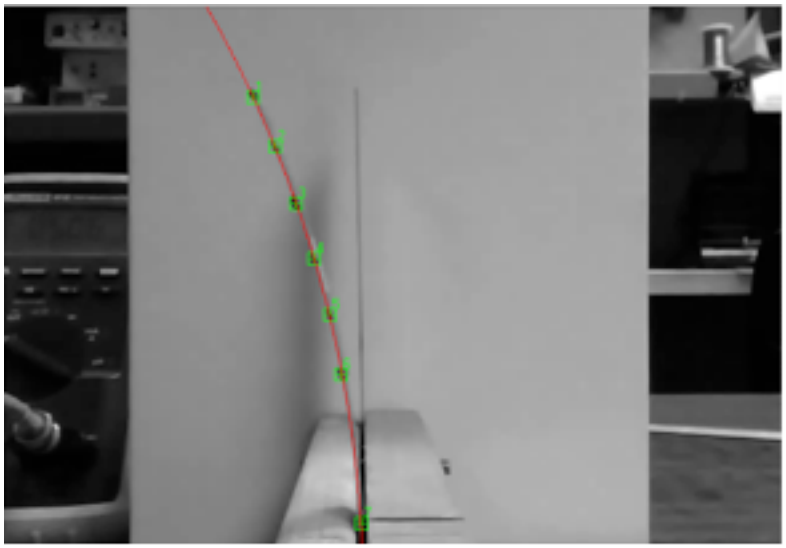

Figure 5.11: 100% morphing condition with image processing depicting the circle fit to the clay dabs.

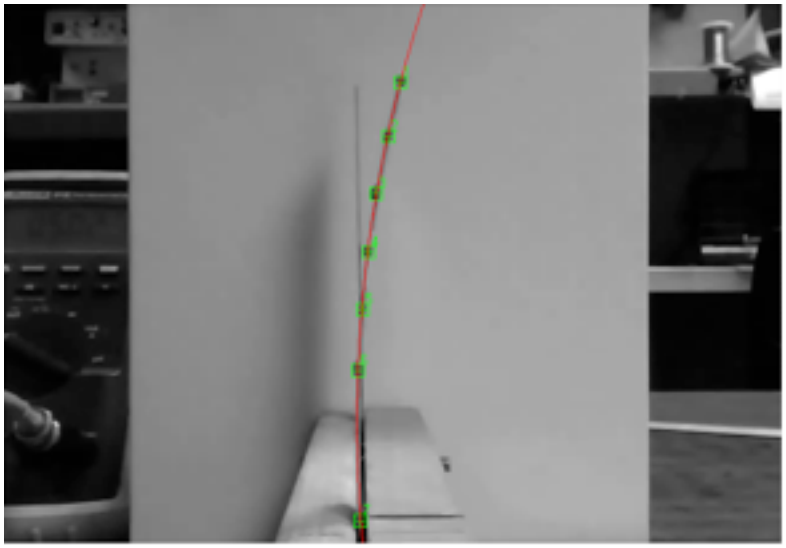

Figure 5.12: -100% morphing condition with image processing depicting the circle fit to the clay dabs.

5.1.4 Bimorph Angle of Attack

Similar to the previous section, it is desired to know how well the geometric equations describe the bimorph's morphed shape. To do this, the image processing software is again used to measure data from the captured video. Here, both the bimorph's Angle of Attack (AoA) and maximum camber are measured. Recall that one

of the assumptions made in Chapter 3 is that the maximum camber change is ≤ 8%, which means that the chord length is approximately equal to the length of the bimorph.

Figure 5.13 depicts how the angle of attack and camber are measured using the image processing software. Relative to the figure, the AoA is the angle between the chord line and the vertical. The camber is the maximum thickness measured from the chord line to the clay markers.

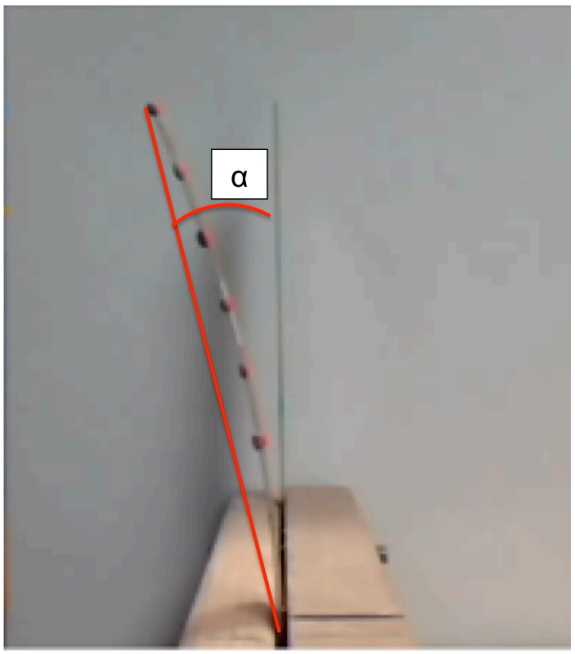

Figure 5.13: Picture of the image processing software depicting the measurements of angle of attack.

Again, the goal here is to quantify how well the equations (Chapter 3) match the experimental data. Figure 5.14 shows the calculated AoA and the measured AoA versus percent morphing. To calculate AoA, the only value required is the radius of curvature of the bimorph at the morphed state. Therefore, the radius is also measured by LabVIEW. The equation to calculate AoA is based only on the radius of curvature, and is reiterated here.

$$\alpha = \frac{S}{2r}$$

In the equation, *r* is the radius of curvature and *S* is the arc length (bimorph length). Last, Figure 5.15 shows the measured and calculated angle of attack versus camber. The figure shows that the calculated angle of attack is under predicting the real angle of attack

by roughly 2 degrees. It is believed that this is due to the bias that is shown in the hysteresis plot (Section 5.1.1). Also note that the maximum camber is only about 4.75% of the chord length. Given a bimorph length of 96.5 mm, the maximum camber is about 4.6 mm. Although no redundancy is provided from these tests, the experimental data matches the equations in Chapter 3 relatively well. These results show that the geometric equations can be used to describe the morphed shape and angle of attack for a cantilevered bimorph.

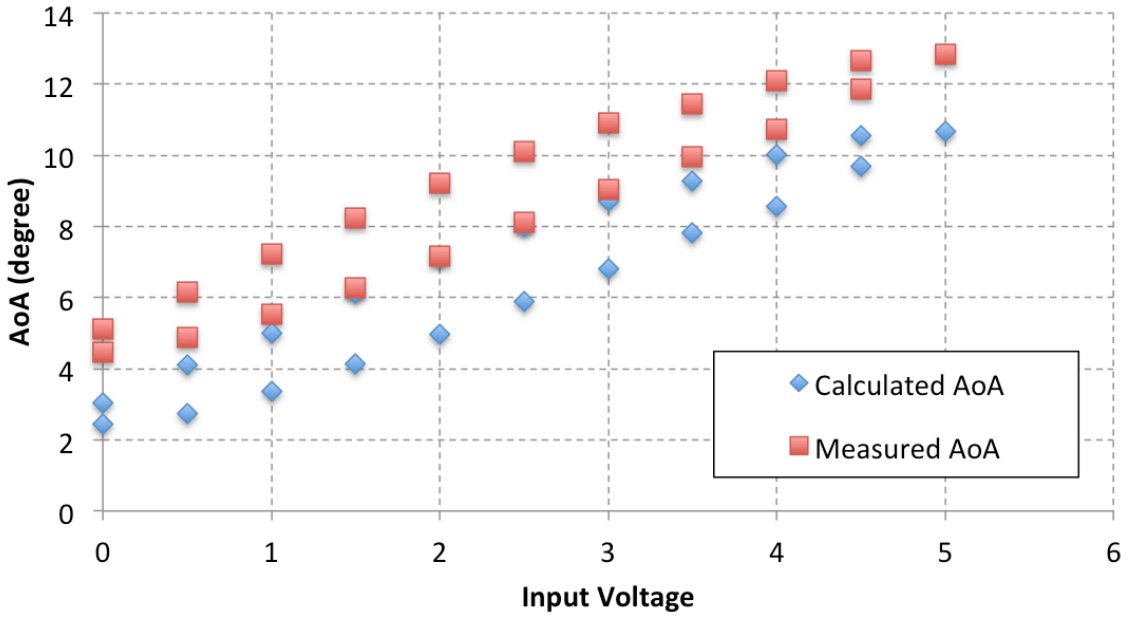

Figure 5.14: Calculated and measured angle of attack versus percent morphing.

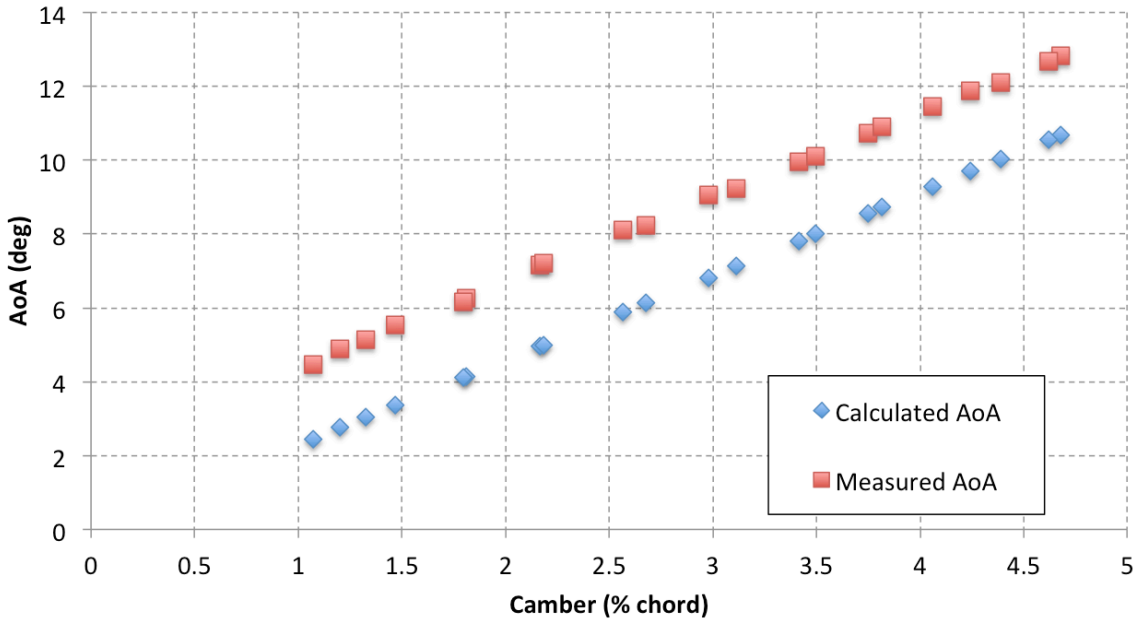

Figure 5.15: Calculated and Measured Angle of Attack versus Camber (% chord length).

5.2 Small Bimorph and Linkage Bench Test

The results from the bimorph and linkage bench tests are presented in the following sections. The experiment procedure is described in Chapter 4, and the bimorph and linkage test specimen is described in the Chapter 3. A picture of the bimorph and linkage during testing is provided in Figure 5.16 below.

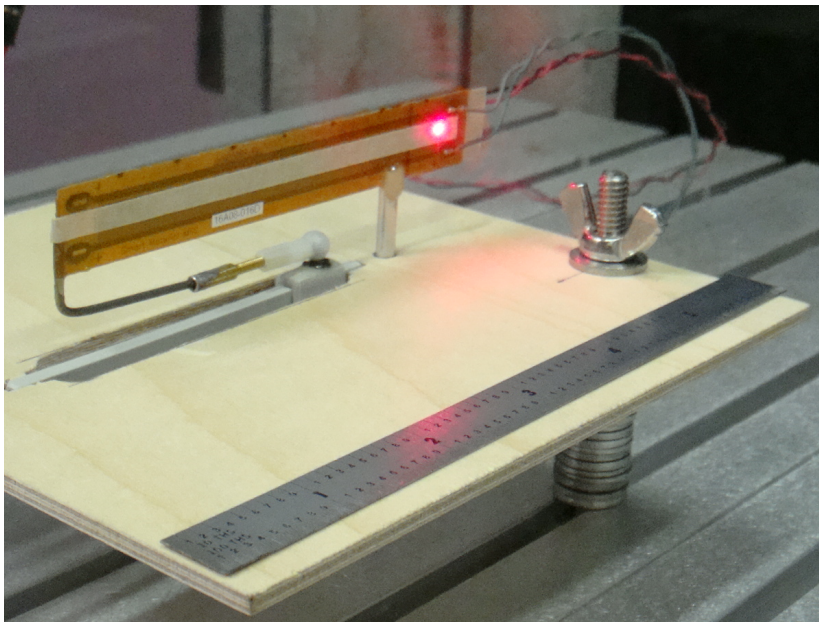

Figure 5.16: Picture of the bimorph and linkage during bench testing.

The bimorph and linkage were tested to evaluate several characteristics of the bimorph system. Three different results are provided in the following subsections. First, the hysteresis plot of the trailing edge deflection is given. Recall from earlier that this is a plot of TE deflection versus input voltage. Second, the angle of attack versus camber change is given and compared to the results found from the cantilevered bimorph. Finally, some general observations made during testing are discussed.

5.2.1 Bimorph and Linkage Hysteresis

Figure 5.17 depicts hysteresis loop for the bimorph and linkage combination. With the linkage, the bimorph now achieves TE deflections of approximately ±40mm (about 1.6in). This is nearly twice the amount of trailing edge deflection that the cantilevered bimorph achieves.

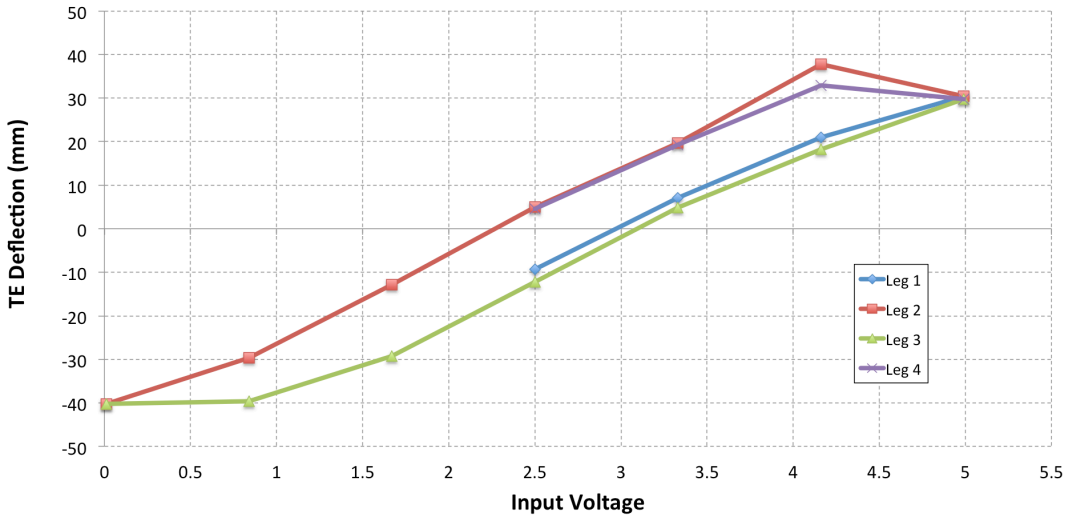

Figure 5.17: Hysteresis plot for the bimorph and linkage concept.

In the figure, the independent axis is the input voltage to the bimorph, which was a 0V to 5V signal. The dependent axis is the trailing edge deflection in millimeters. The hysteresis plot is broken down into separate legs. The Leg 1 is from 2.5V to 5V, Leg 2 is 4.16V to 0V, Leg 3 is 0.83V to 5V, and Leg 4 is 4.16V to 2.5V. The data shows that the bimorph achieves higher deflection at 4.16V (Leg 2 and 4), than at 5V. This is not expected because the bimorph should have its largest deflection at 5V. Currently, it is believed that this is not a physical property of the bimorph but an effect caused by the linkage. This may also be due to another phenomenon that the bimorphs exhibit called

creep. The creep behavior is discussed in Chapter 7 of this thesis. Further investigations will be made to understand the cause of the anomaly.

5.2.2 Bimorph and Linkage Angle of Attack

Figure 5.18 depicts the angle of attack versus percent morphing for the bimorph and linkage combination. Like Figure 5.17 in the previous section, the data is plotted in terms of Legs. The figure shows that the bimorph and linkage achieves a positive angle of attack of about 25 degrees, and achieves a negative angle of attack of about -28 degrees. This is an interesting result, as these values are nearly twice as large as the measured angle of attack for the cantilevered bimorph (Section 5.1.4). Similar to the hysteresis data, an unusual spike occurs at about 66% morphing. Again, this is the same anomaly seen with the trailing edge deflection, and the reason for this value is not know.

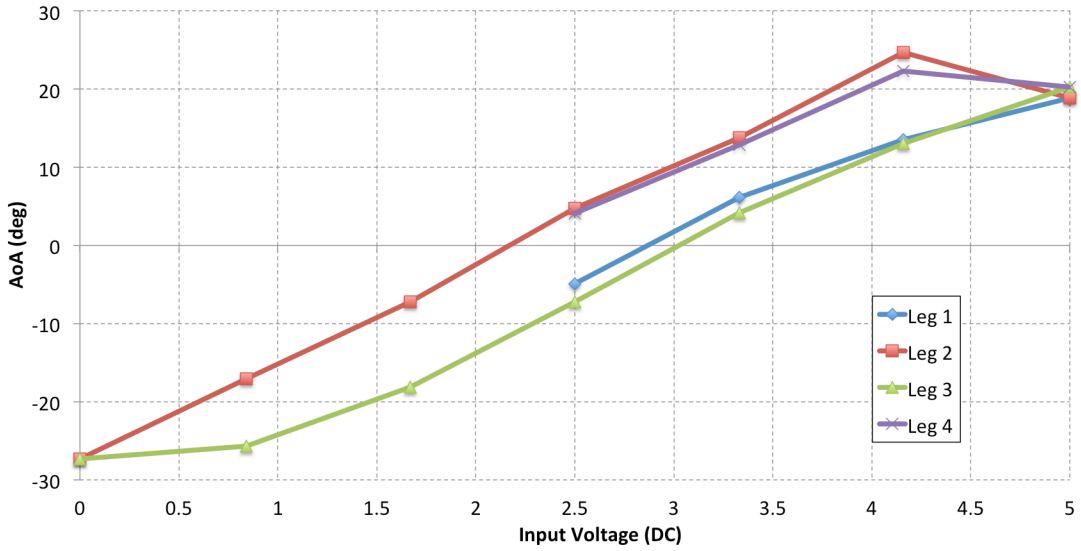

Figure 5.18: Measured angle of attack for the bimorph and linkage concept.

Figure 5.19 shows a comparison of the measured and calculated angle of attack. Here, the values of measured angle of attack are those shown above for Leg 3. Also, the values of negative camber represent the camber when the trailing edge deflection is negative. The angle of attack is calculated using the equations defined in Chapter 3. The angle of attack is calculated by using only the measured value of the maximum camber. As shown, the equation matches the measured data very well for negative TE deflections. However, the measured angle of attack is lower for positive camber. It is believed that

this is not due to the equation, but is due to the bimorph and linkage interactions. This is discussed in the following section.

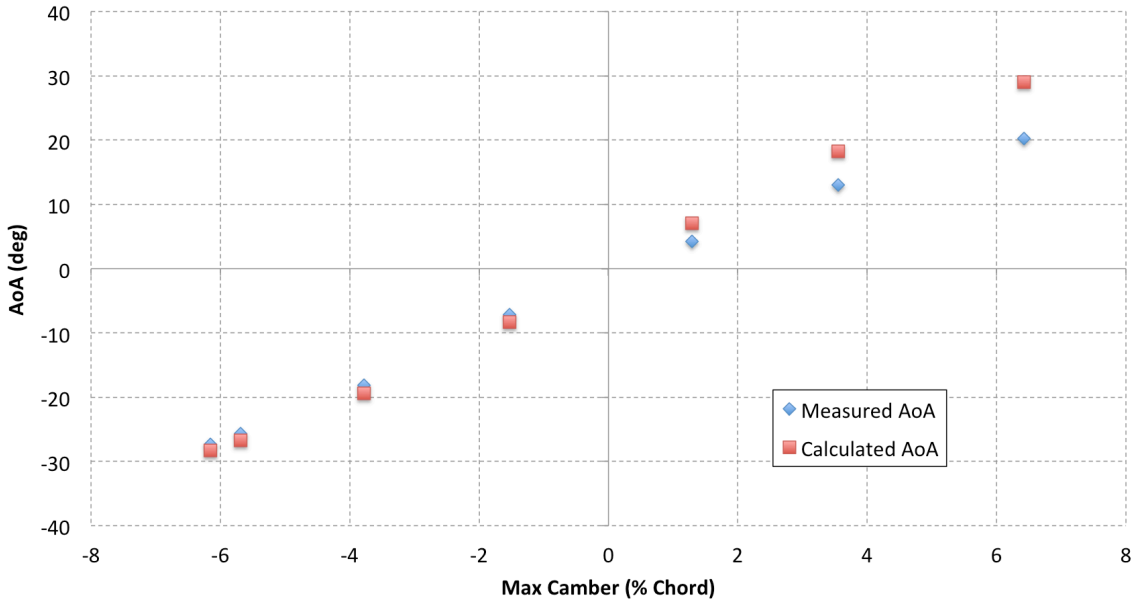

Figure 5.19: Measured angle of attack and calculated angle of attack for the bimorph and linkage concept.

5.2.3 Bimorph and Linkage Interactions

Observations of the bimorph and linkage interactions were made during testing and are discussed in this section. One of the most important discoveries is the actual movement of the linkage along the slot. The TE linkage and slide (grey) is shown in Figure 5.16. Figure 5.20 illustrates the travel of the slide. The figure shows that for a 20mm trailing edge deflection, the slide only deflects about 5mm. This shows that the slot can be much shorter than the one used here. Thus, greatly reducing the weight of the slide and linear bearing.

Another observation was the interactions with the linkage and the linear bearing. As shown in Figure 5.16, the linkage attaches to the linear bearing via a ball joint. It was noticed during testing that the bearing attempts to rotate first, rather than translating along the slide. This rotation is due to the poor manufacturing qualities of the plastic slide and bearing (*i.e.* the inner dimension of the bearing, and outer dimension of the slide are not exact). This manifests itself as *play* in the system, and the trailing edge deflection does not occur as desired. This effect is most evident at low actuation voltages. A better design will eliminate this by tighter tolerances on the slide and bearing.

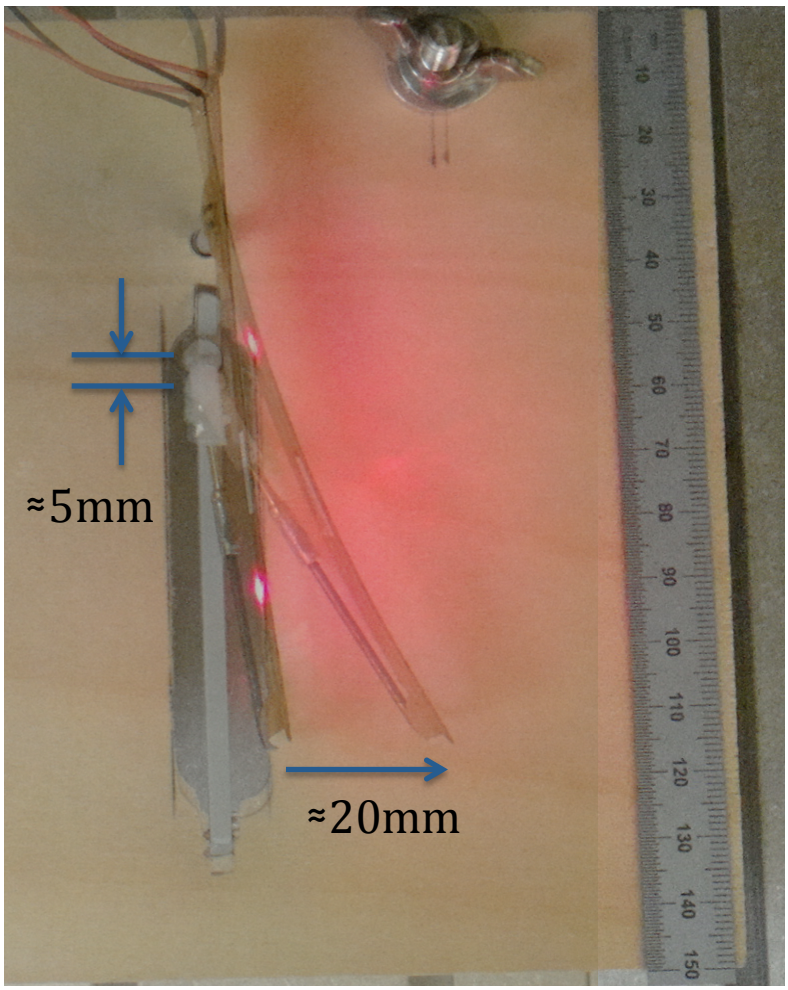

Figure 5.20: Picture of the bimorph and linkage during testing at different actuations to illustrate the travel of the slide bearing.

6. System Identification

This chapter is devoted to describing work performed to model both a bimorph actuator and a servo actuator. Specifically, frequency response tests were performed for a cantilevered bimorph, a bimorph actuated wing section, and for a servo. Given the frequency response of an actuator, a transfer function is found that best fits the experimental data. A few tests were performed to properly model the bimorph. For testing, two Selig airfoil sections were fabricated: one with bimorphs embedded in the upper surface skin, the other with a standard flap actuated by a servo. A more thorough description of the airfoil sections is given in Chapter 3.

Frequency response is a well-known and widely used technique for modeling the response of actuators. To perform a frequency response analysis, the actuator is driven with a sinusoid input signal. Recall that DC voltage is the input to the bimorph's MFC elements. For a bimorph, the input was a voltage signal that was sinusoidal in time with a fixed frequency. For linear systems and low input frequencies, the output should match the input sinusoid in both amplitude and phase. As the input signal frequency is increased, the actuator will have a harder time "keeping up", and the desired sinusoidal output will diminish.

The result of this portion of the research was to obtain a mathematical model of the new proposed actuator. A servo was also tested and modeled so that comparisons can be made between the two actuators. Servos are widely used and are industry standard actuators in small UAVs. Thus, servos are the baseline for performance comparisons.

The remainder of this chapter is organized as follows. First a background is given concerning frequency response. Section 6.2 describes the experiments performed on all of the test specimens mentioned above. This is followed by a discussion of how the measured data was analyzed. Lastly, results are presented in the form of Bode diagrams for the servo and bimorph actuated wing section.

6.1 Frequency Response Theory

Ogata [51] defines frequency response as the steady-state response of a system to a sinusoidal input. In the present case, sinusoidal input signals were input to both the servo and bimorph, and their response was measured with a laser measurement unit. Given the

input signal, the measured output of the system, and time, we gain valuable information about the system. A major advantage of frequency response is that the engineer can model a system by using empirical data. This is opposed to deriving a mathematical model of the system *a priori*. Using frequency response to model a system is very advantageous when considering the challenges of deriving a model for complex systems.

A second advantage of using frequency response to obtain a mathematical model of a system is that it captures the dynamics of the entire system. Take for example the bimorph. First one must model the bimorph beam, which is challenging due to the coupled electrical and mechanical nature of the bimorph. Then, a second model is required to capture the dynamics of the amplifying circuitry that supply the bimorph with voltage. On the other hand, by performing frequency response both the dynamics of the bimorph beam and the dynamics of the circuitry are captured simultaneously.

To understand the results of a frequency response experiment, engineers typically employ the Bode diagram. A sample Bode diagram is provided in Figure 6.1. Here, the top plot is gain (dB) versus frequency (rad/sec) on a logarithmic scale. Gain is used here because it allows the viewer an easy way to decipher the information found during the frequency response.

Gain is computed by comparing the amplitudes of the input and output sine waves from the frequency response test. Take for example, the two sine waves provided in Figure 6.2. The amplitude ratio (*X/Y*) is converted to gain (decibels) via the following relationship.

$$G = 20log_{10}\left(\frac{X}{Y}\right)$$

Equation 6-I

An amplitude ratio of one will have a gain of 0dB. An amplitude ratio larger than one will have positive gain values, while an amplitude ration less than one will have negative gain values. Looking at the example Bode diagram (Figure 6.1), it can now be seen that the input and output of the system match at low frequencies, and diverge as the system begins to resonate (the peak).

The bottom chart of the Bode diagram is the phase angle of the output sinusoid with respect to the input. It is also plotted against frequency (rad/sec) on a log scale, and is relatively easy to calculate. A phase *lag* can be seen in the sample plot given in Figure

6.2. Phase is found by computing the time of zero-crossing for the two sinusoids, and then applying the following relationship.

$$\phi = 360(t_{output} - t_{input})f$$

Equation 6-II

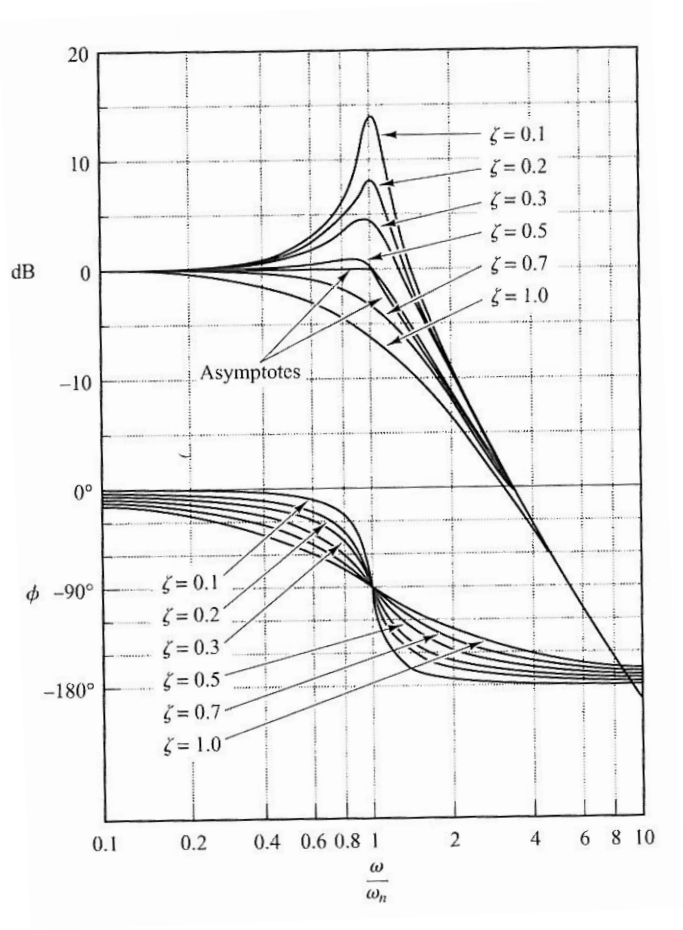

Figure 6.1: Example Bode diagram [51].

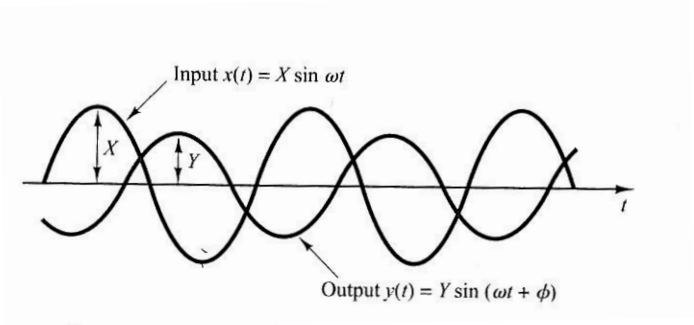

Figure 6.2: Sinusoids of the Same Frequency with Differing Amplitude and Phase [51].

In Equation 6-II, t_{output} is the zero crossing of the output sine wave, t_{input} is the zero crossing of the input sine wave, and f is the frequency of the two sinusoids. Once the measured data has been plotted on a Bode diagram, a transfer function can be found that fits the data, which will serve as a model for the system. This will be discussed in the following sections.

6.2 Description of Experiments

In this section, the reader is given a brief description of how the frequency response experiments were performed. In short, two experiments were performed. The first was a frequency response test to better understand the bimorph and a bimorph actuated wing section. The second was a frequency response test performed to understand a servo and a servo actuated wing section.

The end results of these tests were two fold. First, the author desired to compare the performance between a servo and a bimorph. The servo is the industry standard actuator for small UAVs and serves as a good baseline for comparison of the new proposed bimorph actuator. Second, the author desired to model the servo and bimorph actuators empirically. Deriving a model from scratch is daunting, and in this case would still have required testing to obtain parameters for the model. It was quickly decided to use frequency response to find a transfer function that best fit the measured data from frequency response tests.

6.2.1 Servo (Futaba S3156) Frequency Response

The wing section model and servo are described in Chapter 3. Two tests were performed, one with the servo in a loaded configuration, and the other with the servo unloaded. For the loaded tests, the servo was actuating the trailing edge flap of the wing section. The unloaded tests were simply the servo actuating its arm.

Figure 6.3 depicts the experimental setup used during the frequency response tests. LabVIEW was used to generate the input signal to the servo. The wing section with embedded servo was mounted in the CNC bed. The laser measurement unit was mounted to the CNC head, and the laser was focused on the servos arm extension discussed later. The laser measured the distance between it and the actuator at the same frame rate of the

input signal to avoid triggering issues. Once returned to LabVIEW, the input and output data, and their time stamp, were compiled into a text file.

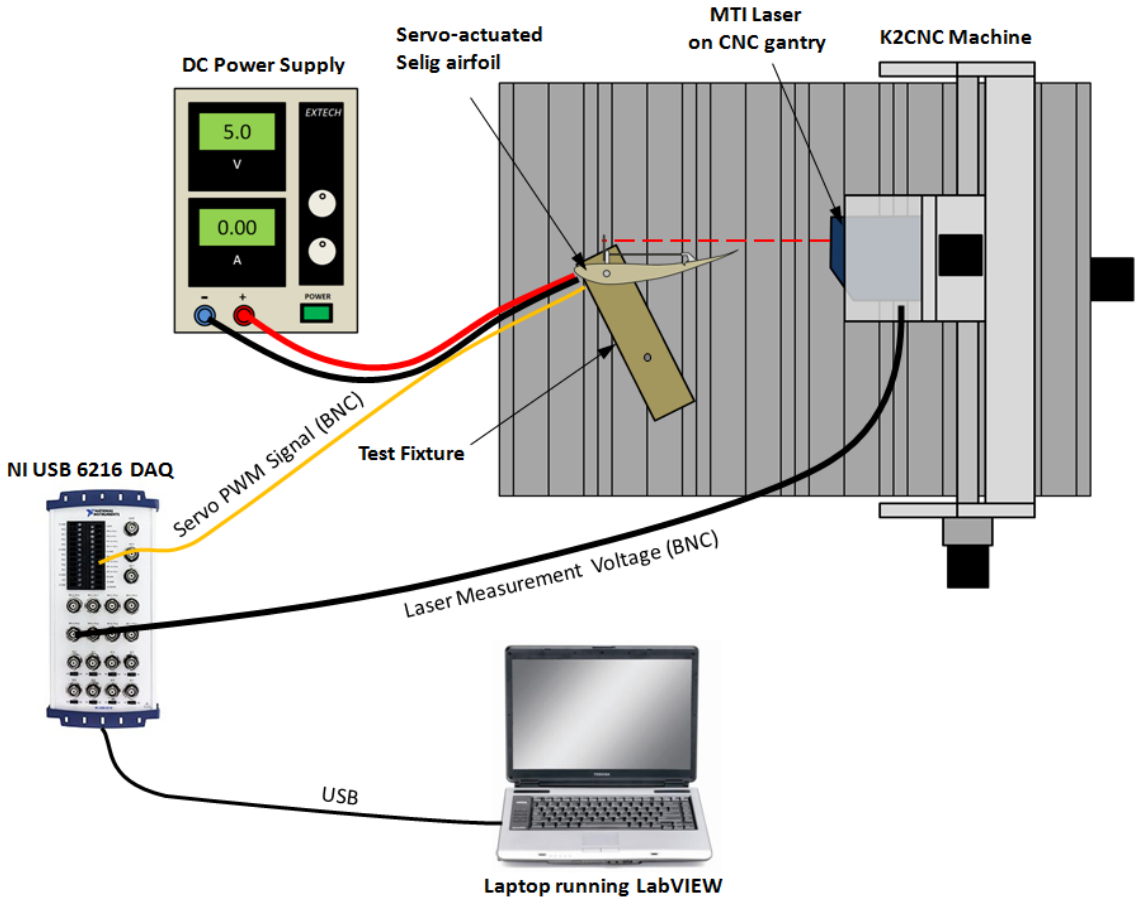

Figure 6.3: Schematic of the Frequency Response Experiment for the Servo Actuated Wing Section.

A Pulse-Width-Modulated (PWM) signal is used to actuate the servo. A sample PWM signal is given in Figure 6.4. In short, a PWM signal is a rectangular wave having either a value of on or off for small durations of its period, hence *pulse*. The typical voltage for a servo is 5V DC. The period of the PWM for the servo tested during this research is 20 milliseconds, with 1 to 2 millisecond pulse widths. Thus, the period of the rectangular wave is 20 milliseconds, and the pulse has an ***on*** value for about 10% of the signals period (<= 2 milliseconds). At the receiving end, the servo measures the length of the ***on*** time versus the duration of the ***off*** time over each period of the signal. The duration of the pulse defines an angle for the servo. Thus, a 1.5 millisecond pulse actuates the servo to 0 degrees, a 2 millisecond pulse to +45 degrees, and a 1 millisecond

pulse to -45 degrees. The resolution is roughly a 0.005 millisecond pulse (about 0.5 degrees).

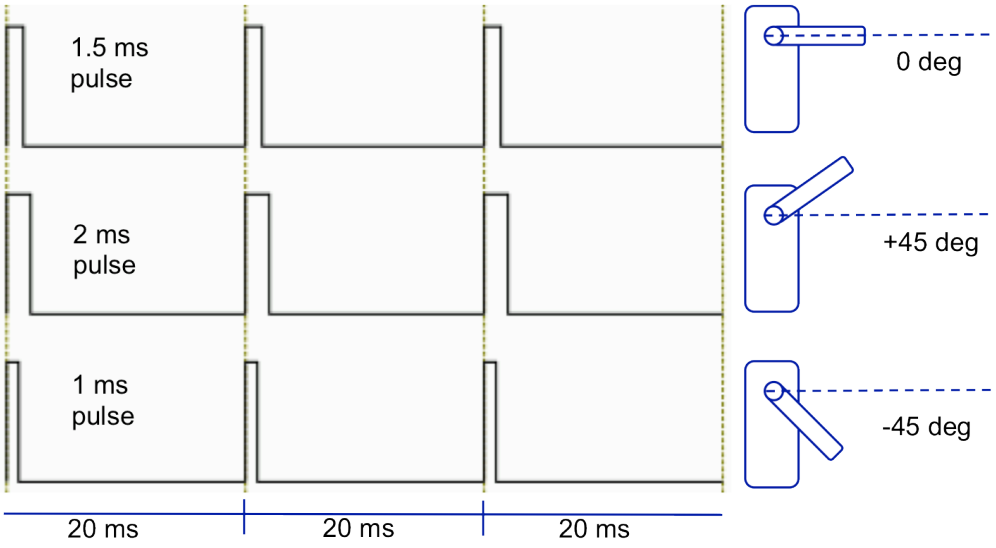

Figure 6.4: Example PWM Signal for Actuating a Servo.

The important thing to understand regarding PWM commands is that the servos actuation speed is limited by its input signal. This limit is directly related to the period of the PWM signal, which in this case is 20 milliseconds (the standard PWM for UAV servos). In other words, the PWM is refreshing at a rate of 50Hz. The servo would not be able to track a 50Hz sine wave input, as only 1 point of the sine wave would be received by the servo during each period. Similarly, a sine input of 25Hz would be more like a triangular wave, as only two points of the input sinusoid would be received by the servo. This corresponds to the Nyquist frequency (half of the sampling frequency) as the theoretical limit for frequencies that can be tracked. In reality, the servo is limited to frequencies much lower than 25Hz.

Figure 6.5 depicts the servo and wing section as it was during testing. A flat wooden stick was attached to the servo's arm that provided a reflective surface for the laser. The wooden attachment was used only as a target for the laser measurement unit.

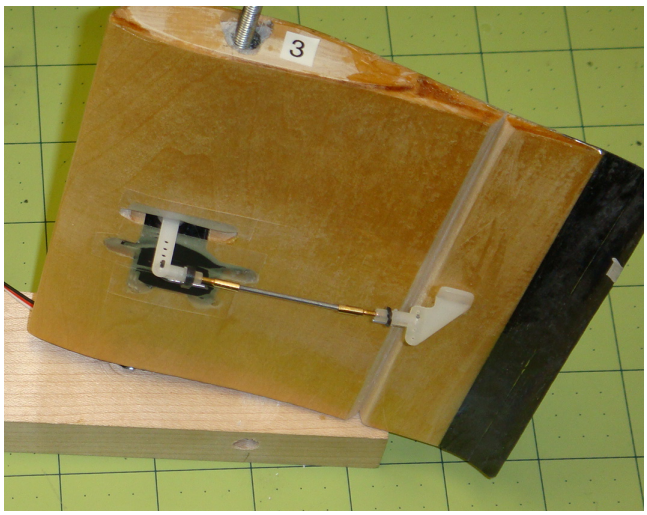

Figure 6.5: Picture of the servo in the airfoil with the wooden stick on its arm (used for the laser).

6.2.2 Bimorph Frequency Response

The cantilevered bimorph and the bimorph actuated wing section are also described in Chapter 3. Here, as with the servo, two experiments were performed. The first was a frequency response for a cantilevered bimorph beam. The second was for the bimorph actuated wing section.

Figure 6.6 and Figure 6.7 shows the cantilevered bimorph and bimorph wing section as they were during testing. Masking tape was placed chord-wise along the top surface of the wing section. The tape was used for a reflective surface for the laser measurement unit. Data was taken at each of the tape locations to observe any non-symmetric bending that might occur during actuation.

The experimental setup is similar that used for the servo tests. Again, LabVIEW was used to create a sinusoidal input signal. The data was then sent through amplifying circuitry, which amplified the input voltages to the 1500V range required by the MFC elements. The laser measured the response of the bimorph by measuring the distance between it and the wing section. Laser data was acquired at the same rate and time as the input signal was generated so that no triggering issues were encountered. Lastly the data was sent back to LabVIEW, where it was packaged into a text file.

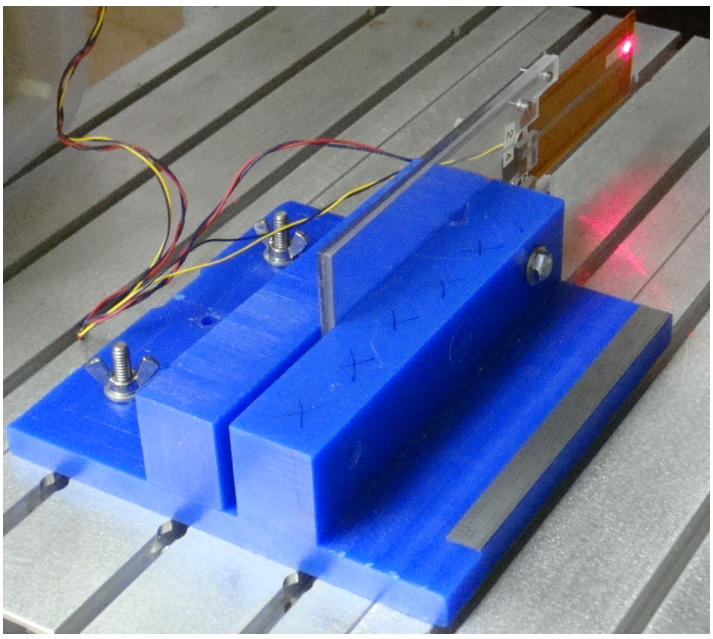

Figure 6.6: Picture of the cantilevered bimorph during the frequency response test.

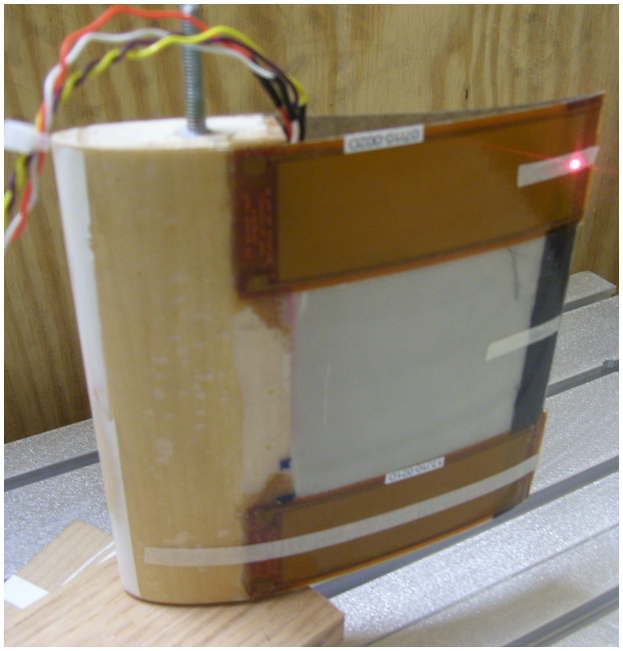

Figure 6.7: Picture of the bimorph actuated wing section during the frequency response tests.

Note that, unlike the servo, both the actuator and the amplifying circuitry were tested for the bimorph specimens. So, the system tested here is representative of an onboard, flight quality system. A standard voltage supply on typical UAVs is 12V. However, the MFCs require 1500V to perform actuation, hence the need for some form of amplification to control actuation. In Figure 6.8, the blue shaded area represents the

actual system that was tested. Thus, the laser is measuring both the response of the actuator and the response of the amplifier circuitry. The author understands the importance of testing only the response of the actuator. Unfortunately, doing this requires measuring the high input voltages that are input to the MFC. At the time that this research was performed, there was no equipment available to the author to perform this task. The author would like to note that, because the circuitry is a necessary part of the bimorph system, it is also important to understand the response of the entire system.

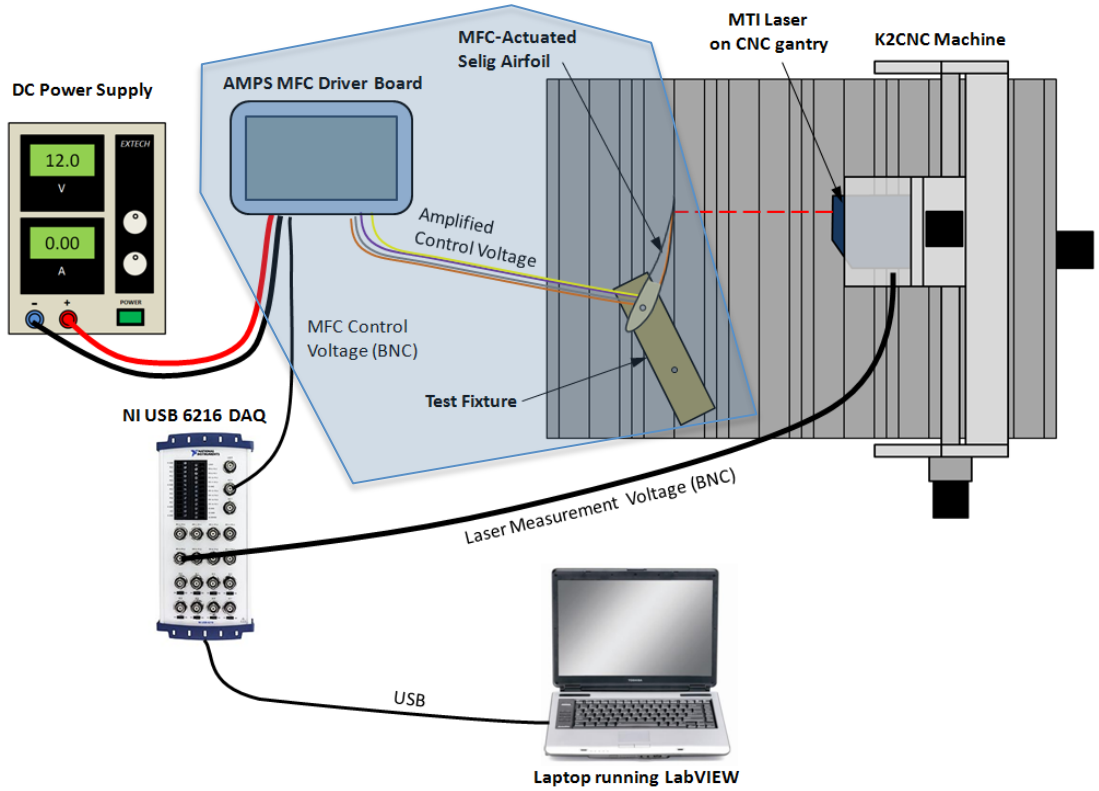

Figure 6.8: Flow chart of data during the bimorph frequency and transient experiments.

6.3 Data Analysis

Once the data was collected, it was analyzed to obtain the desired frequency response information. This section provides information about how the experimental data is reduced and analyzed. This section is arranged into four parts. First, it is important to understand the measured data from the experiment. Second, more data is collected than is needed for analysis, and thus the large data set is reduced. This is discussed later in more detail. Third, although the laser is a very accurate measurement

device, the returned data is still noisy. So, the noise is filtered so that better results are obtained. And fourth, the data is compared to the input sinusoid signal and the results are plotted on Bode diagrams.

As mentioned in Section 6.2, four individual specimens were tested. The cantilevered bimorph, the bimorph actuated wing, and the servo in a loaded and unloaded condition. The data recorded from each test is analyzed in the same manner. So, for the descriptions the author only describes the analysis as if it were performed on the cantilevered bimorph.

Raw Experimental Data

This sub section is intended to describe the form of the recorded data from each experiment. To describe this, it is first necessary to understand more about the experimental procedure and how the data was collected. First, the cantilevered bimorph was actuated at discrete frequencies. For each actuation frequency, LabVIEW recorded the input voltage and the laser output voltage. LabVIEW generated the input voltage at 10kHz, and sampled the laser output at the same rate. Thus, the input voltage and laser output were recorded simultaneously. Lastly, LabVIEW also recorded the time stamp for each sampling. Thus, the recorded data was a Nx3 matrix where N is the number of data samples recorded.

To perform the experiments, a LabVIEW code was used which allowed the user to specify key values to dictate how data was collected. First, the engineer specifies the frequency and the number of periods to actuate the bimorph. The input signal to the system is sine waves at discrete frequencies of 0.1Hz to 50Hz. The number of actuation periods is also specified for each actuation frequency. Generally, more than one period of actuation is required for the system to settle into its steady state sinusoidal motion.

Second, the engineer specifies the amplitude of the input sinusoid to the actuator. As described in Section 6.2 (Figure 6.8), the input signal first goes to the amplifier circuitry in the form of a control signal. The inputs to the amplifier are a constant 12V signal for power, and a 0V to 5V control signal. A control signal of 2.5V corresponds to the neutral condition for the bimorph, while 5V and 0V correspond to 100% and -100%, respectively. To avoid damaging the bimorph during resonance, the input amplitude was 3.75V to 1.25V, or roughly ±50% actuation.

At each input frequency, a data file is generated which contains the input voltage to the amplifier circuitry, the laser output, and the time stamp at which the data is sampled. Again, the input to the amplifier was a control signal between 0V and 5V. The laser outputs are values between 0V and 10V, and the time stamp is recorded in seconds.

Reduced Data

Only a portion of the measured data is required for analysis, and so the raw data is reduced to a more manageable set. As mentioned above, the data is stored in files for each discrete frequency of actuation. And, many periods are taken to allow the actuator to reach a steady state. For each actuation frequency, only the last two periods of the data set are used. So, only 2 periods of the data is kept, but the measured laser data is noisy. To combat this, a sine was fit to the measured output data and is discussed in the following subsection.

Fitting the Data

Figure 6.9 below shows a picture of the measured signal from the laser for an actuation frequency of 1Hz. The figure shows that the measured data is noisy, thus making phase and amplitude calculations difficult to accurately calculate. The author chose to fit a sine wave to the measured data, which is thought of as a form of filtering. The fit was found by using MATLABs *fminsearch* function. In short, fitting the sine finds the ideal sine wave that best fits the measured data. The function *fminsearch* was used to minimize the objective function J given below.

$$f\left(t\right) = A\sin\left(\omega t + \phi\right)$$

and

$$J = \max\left(\left(f(t) - l(t)\right)^2\right)$$

In the equations, $f(t)$ is the sine function to fit to the laser data $l(t)$. Furthermore, A is the amplitude of the sine fit, t is time, $\boldsymbol{\phi}$ is the phase lag, and ω is the actuation frequency. The optimization parameters were the amplitude and phase. Thus, *fminsearch* changes the values of A and $\boldsymbol{\phi}$ to minimize the cost function J. The result of the sine fit for 1Hz actuation frequency is provided in Figure 6.9.

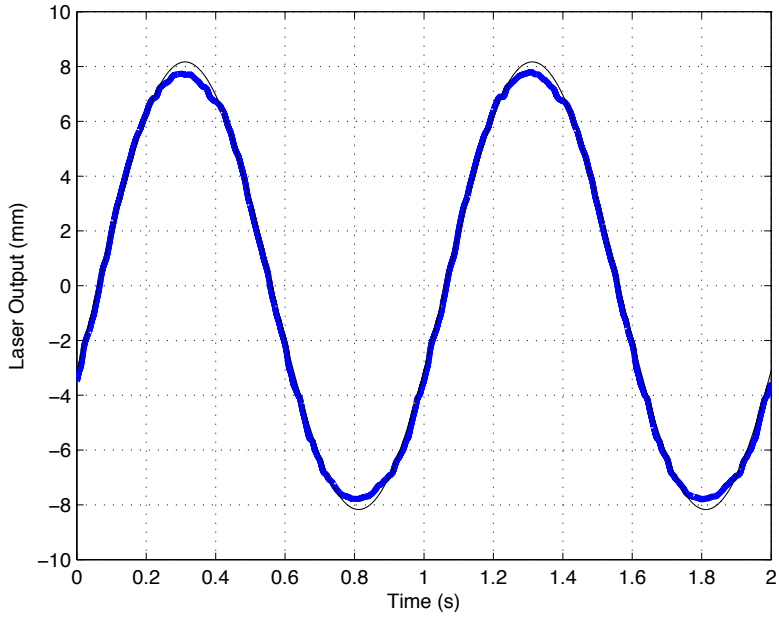

Figure 6.9: Laser measurement (blue) and fitted sine wave (black) from the cantilevered bimorph frequency response at 1Hz.

Scaling the Data

The last step in the process is to scale the fitted data to compare the magnitudes on a Bode diagram. The laser returns a value between 0V and 10V, and each voltage corresponds to a distance away from the laser. For the gain plot of the Bode diagram to start at zero gain, these values must be the same magnitude. Therefore, to perform the amplitude correction the data measured at the lowest actuation frequency (0.1Hz) is assumed to be equal in magnitude to the input sinusoid. Thus, it is assumed that the amplitude ratio is unity at the lowest frequency.

6.4 Results and Discussion

In this section, the author provides the results from the experiments described in the previous sections. First, results from the servo's frequency response are given, followed by the results from the bimorph actuation. Since the servo is the industry standard actuator for UAVs, it is treated here as the baseline for comparison.

6.4.1 Servo Results

As mentioned earlier, the servo was tested in both loaded and unloaded configurations. Figure 6.10 depicts the frequency response results for the servo in both

configurations. No noticeable difference can be seen between the loaded and unloaded servo data. This was anticipated because the load on the servo due to the flap is small. It is expected that a larger flap, or aerodynamic pressure loading, would result in a difference between the loaded and unloaded conditions. The highest frequency the servo can track is roughly 20 rad/sec (≈3Hz), before the gain and phase diverge.

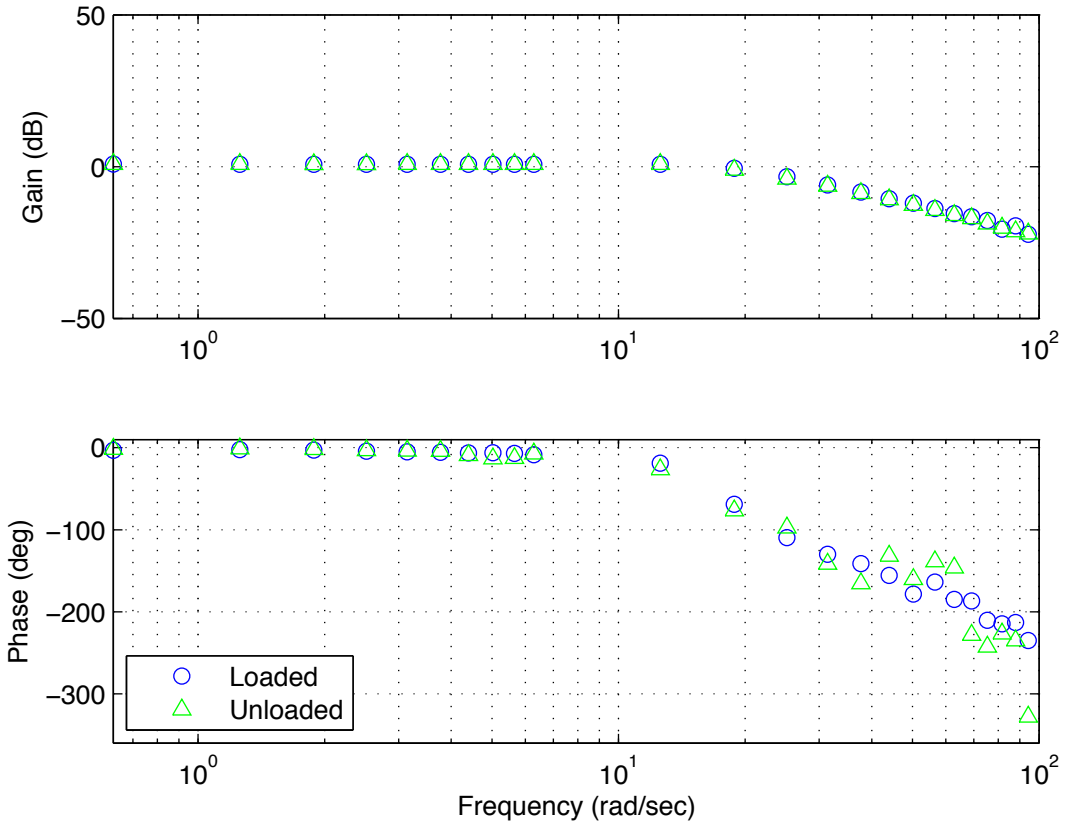

Figure 6.10: Bode Diagram for the Servo in Unloaded and Loaded Conditions.

Figure 6.11 depicts the measured servo data and the transfer function that best fits the data. The transfer function is also provided in Equation 6-III. As can be seen, the transfer function is of second order, which is characteristic of most servo devices. To fit the transfer function to the data, the MATLAB function *invfreqs.m* was used, which is available in MATLABs Signal Processing Toolbox. This m-function was designed specifically for the purpose described here (i.e. using measured data to fit the best transfer function). The inputs to *invfreqs.m* are as follows. First, the complex frequency response data is input in the following form.

$$H_n = A_n \exp(\phi_n i)$$

In the above, A is the amplitude ratio, $\boldsymbol{\phi}$ is the phase lag, and the subscript n designates the n^{th} actuation frequency. Therefore, the frequency response is input as a vector quantity with elements made up of H_n. The second input is also a vector that is made up of the discrete actuation frequencies $\boldsymbol{\omega}_n$. The remaining inputs to *invfreqs.m* are the desired order of the numerator and denominator for the transfer function fit. Thus, the user is able to specify the order of the resulting transfer function from the frequency response data.

In Figure 6.11, the model fits the measured gain data very well. However, the phase only fits the data at low frequencies. This is a trade off that was made by the author. Based on the gain fall-off, the servo most likely will not be actuated beyond frequencies of 30 rad/sec (approximately 4.5Hz), where the gain is less than -10 decibels and the phase lag is less than 90 degrees. At -10dB, the amplitude ratio is about 0.3, meaning that the output of the servo is only 30% of the input. Furthermore, at this frequency, the servo is lagging the input signal by approximately 150 degrees. Thus, the decision was made that the transfer function should fit the data as best as possible in the low frequency spectrum, where the servo is expected to be actuated the most.

$$TF = \frac{358.8}{s^2 + 12.36s + 396.4}$$

Equation 6-III

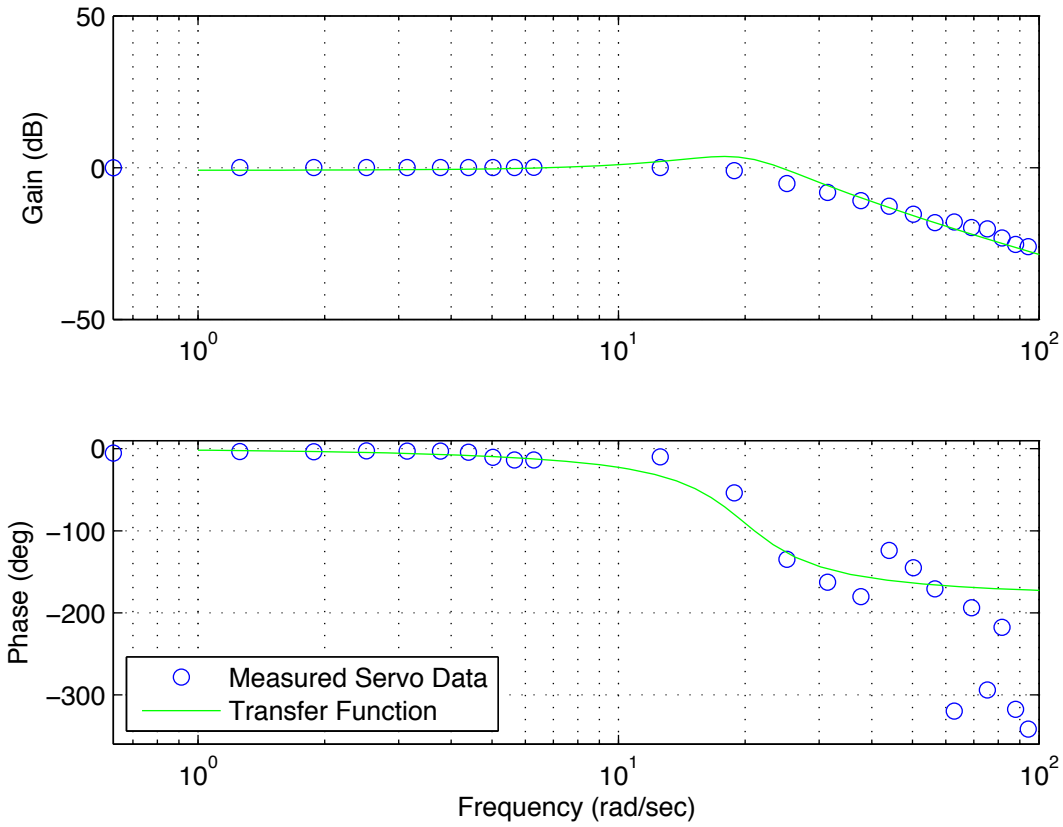

Figure 6.11: Bode Diagram of the Loaded Servo and Modeled Transfer Function.

6.4.2 Cantilevered Bimorph Results

The following presents the results for the frequency response for the cantilevered bimorph shown in Figure 6.6. The cantilevered bimorph is described more thoroughly in the Chapter 3. The Bode diagram shown in Figure 6.12 provides the response of the cantilevered bimorph and the transfer function that best fits the measured data is provided in Equation 6-IV.

$$TF = \frac{0.07356s^3 - 10.61s^2 + 4297s + 1.994e05}{s^3 + 32.66s^2 + 1.227e04s + 1.963e05}$$

Equation 6-IV

As can be seen in Figure 6.12, the cantilevered bimorph resonates at about 100 rad/sec (≈18Hz). This is due to the first resonant frequency of the bimorph beam structure and is sufficiently faster than the servo. However, the phase lag is concerning. First, in the low frequency content between 0.6-6rad/sec, the bimorph lags the input signal by about 20 degrees. The cause of this lag is not yet known, but the author expects that this may be due to the bimorph's hysteresis. Second, just before resonance the phase

lag diverges rapidly. At 90rad/sec, the phase lag is about 45 degrees. More work will be done to understand the phase lag for the bimorph.

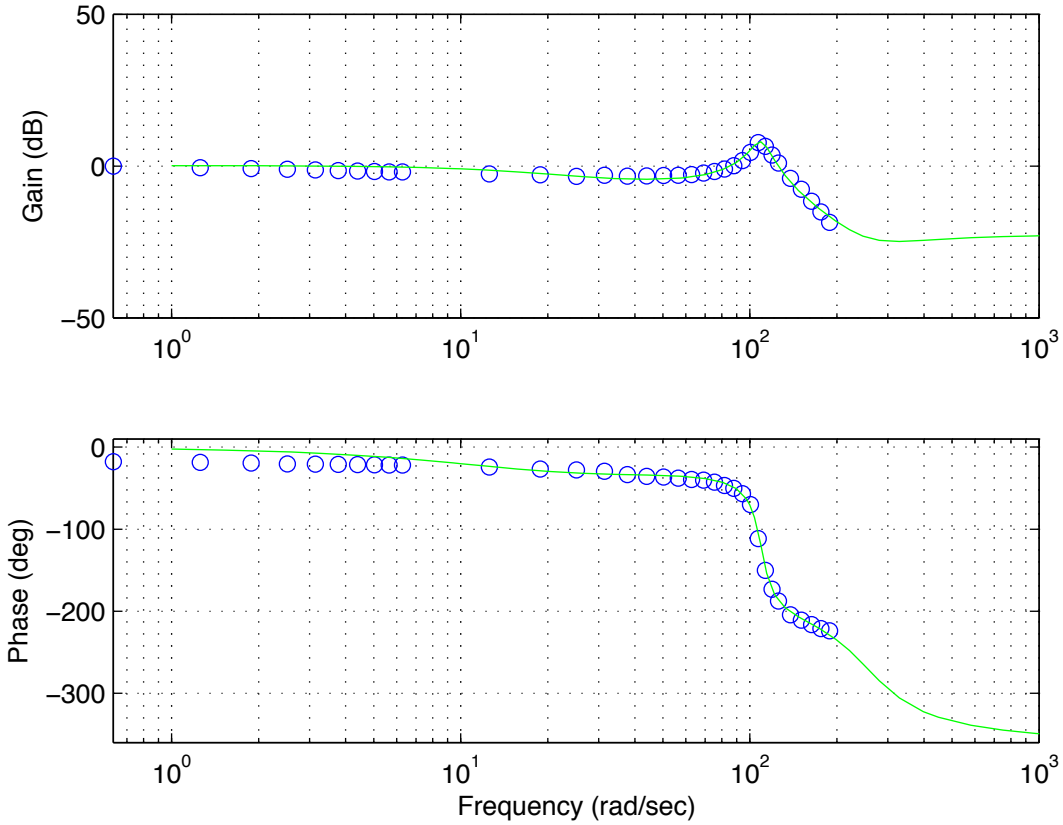

Figure 6.12: Bode Diagram of the Cantilevered Bimorph and the Modeled Transfer Function.

6.4.3 Bimorph-Actuated Airfoil Results

The bimorph-actuated airfoil is shown above in Figure 6.7 and is described in Chapter 3. Figure 6.13 shows the Bode diagram for the bimorph-actuated airfoils frequency response. Also, Equation 6-V provides the transfer function that fitted the measured data. As shown, the wing section resonates at roughly 200 rad/sec (≈32Hz), which is higher than the resonate frequency of the cantilevered bimorph and much higher than the servo. It is believed that this is due to the added structure and stiffness from the wing material. The same phase lag effect is also seen here. As with the cantilevered case, the airfoils phase lag is also roughly 20 degrees at low frequencies, and has the steep divergence at resonance. An interesting note is that the order of the transfer functions for both the cantilevered case and the bimorph airfoil are the same.

$$TF = \frac{0.05s^3 - 7.459s^2 + 4282s + 1.822e06}{s^3 + 64.01s^2 + 5.103e04s + 2.043e06}$$

Equation 6-V

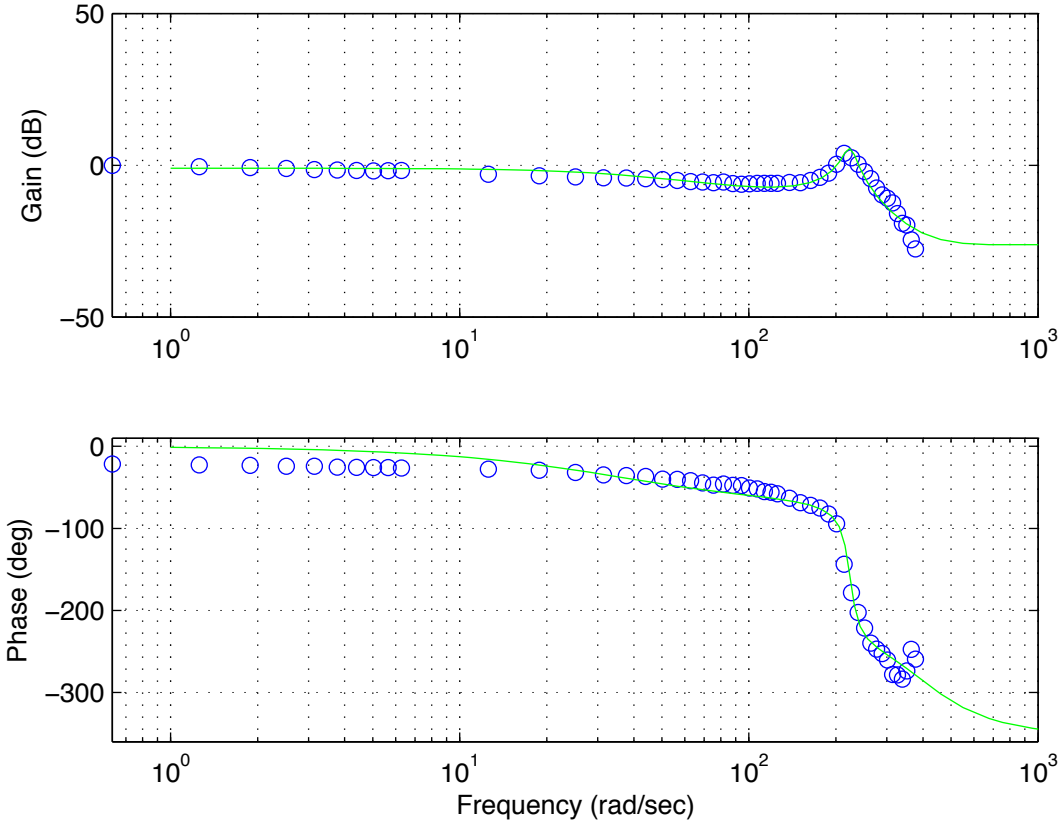

Figure 6.13: Bode Diagram of the Bimorph Actuated Wing Section and the Modeled Transfer Function

6.4.4 Comparison of the Servo and Bimorph Actuated Wings

Figure 6.14 depicts the Bode diagram for both the servo and bimorph actuated wing sections. It has already been shown that the bimorph airfoil can respond to input signals at much higher frequencies than that of the servo. However, the caveat of the previous statement is that the bimorph exhibits some phase lag issues that must be addressed before making a final conclusion.

Lastly, servos have a built in control system that maximizes their response to a given input. The author expects that with a similar control system, the bimorph's phase lag will be corrected, and the response time will be at least equal to the servo.

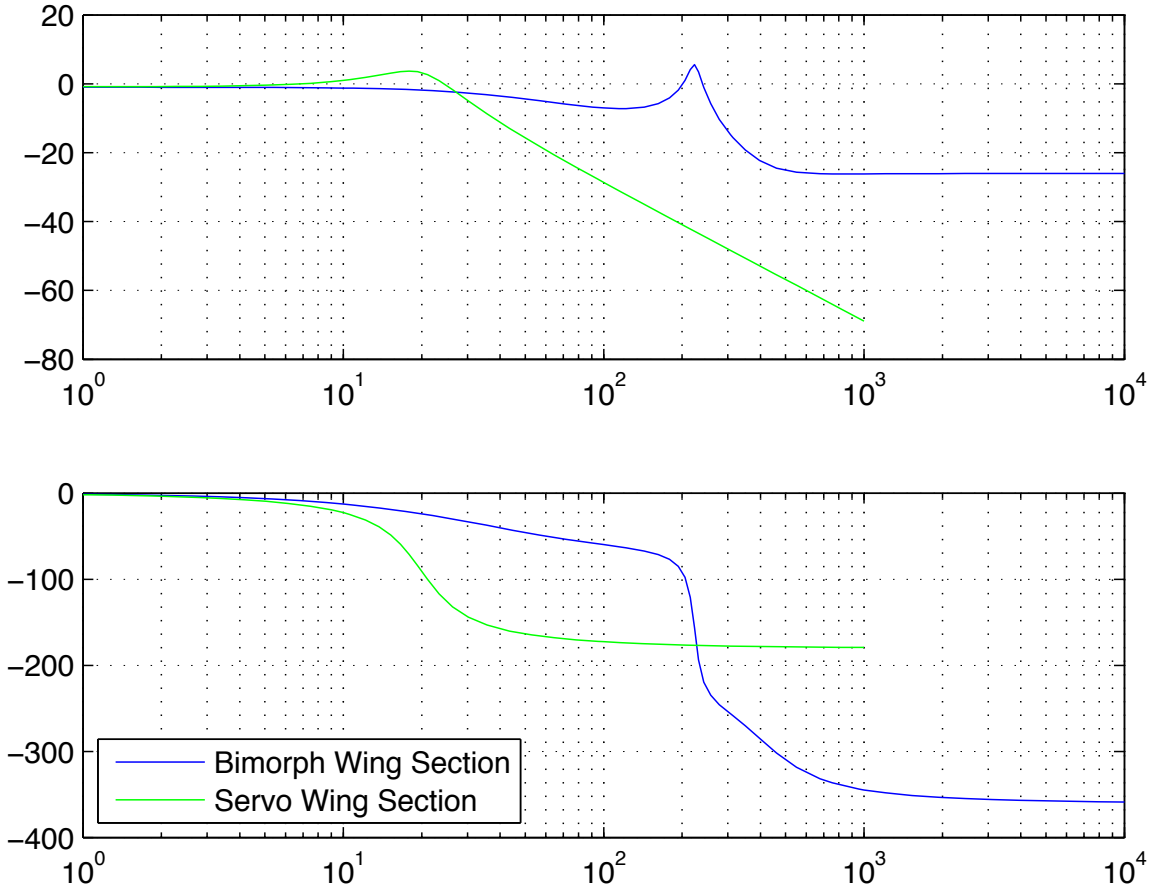

Figure 6.14: Bode Diagram of the Modeled Transfer Functions for the Bimorph and Servo Actuated Wing Sections.

6.5 Discussion and Conclusions

The preceding sections discussed the procedure, data analysis, and results for some frequency response experiments. These experiments were performed on four test specimens: an unloaded and loaded servo, a cantilevered bimorph, and a bimorph actuated wing section. Each of these specimens is described in Chapter 3. For each specimen, a transfer function was found that best fit the measured frequency response data. These transfer functions will be used for control simulations which is discussed in the following chapter.

First, it should be noted is that an assumption was made in the frequency response of the bimorphs test specimens. The frequency response analysis assumes that the tested system is Linear and Time Invariant (LTI). However, the bimorphs are nonlinear due to their hysteresis. This is discussed further in Chapter 7.

Furthermore, at least three conclusions can be drawn from the results. First, the results from the loaded and unloaded servo are roughly the same. This is most likely due to the low mass flap that the servo was actuating. The author expects to see different results under higher loads, such as aerodynamics and heavier flaps. The second conclusion is that the bimorph has some phase lag issues that must be addressed. It is expected that the phase lag is due to the hysteresis exhibited by the bimorph. The final conclusion is that, in open loop operation, the bimorph-actuated airfoil can respond much faster than the servo-actuated airfoil.

7. Controlling the Bimorph

The previous chapter discussed modeling the different actuators using frequency response methods. The frequency response experiments yield transfer functions for each of the actuators described in Chapter 3. In this chapter, the author discusses using those transfer functions for control simulations. Because the bimorph exhibits hysteresis, open loop control is not a realistic option if precise control is desired. For that reason, closed loop control must be utilized. In this chapter, the author presents the current work that has been performed toward controlling the bimorph actuators. Also, some of the planned future work toward inversion based bimorph control is presented.

This chapter is arranged into three sections. The first section discusses the control simulations that were built to simulate the response of the bimorph. Proportional-Integral-Derivative (PID) control was used in the simulation. The second section discusses implementing a control system in LabView to control the cantilevered bimorph. The results of step response experiments are provided that compare the bimorphs open and closed loop responses. The final section is a review of the possible methods to control a bimorph on an aerial vehicle. In this section, the author provides some potential sensors that can be used to achieve a closed loop system, along with some alternative control methods.

7.1 Closed-Loop Control Simulations

Using the transfer functions obtained from frequency response tests in the previous chapter, a simulation was built in Simulink. The block diagram of this simulation is given in Figure 7.1 below. The simulation models the operation of both the 85x28mm active area bimorph. The well-known PID control scheme is used to "close the loop" for the bimorph's actuation.

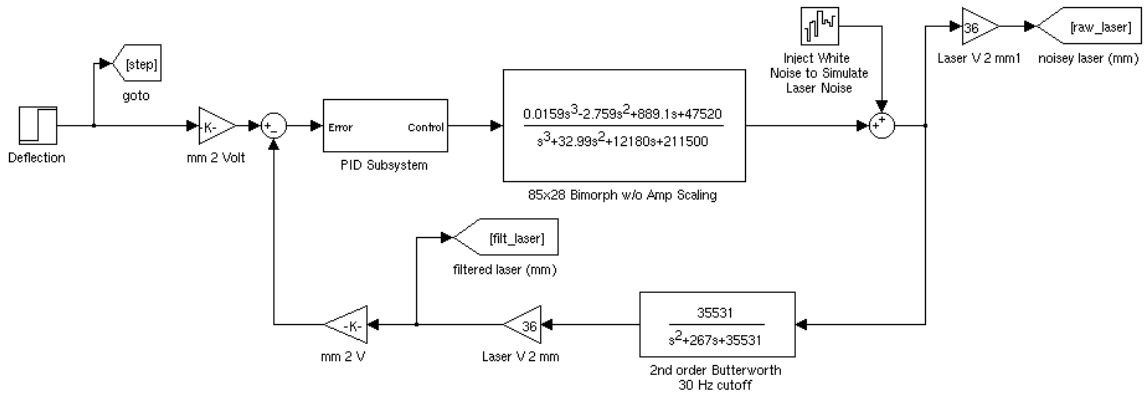

Figure 7.1: Block diagram of the bimorph control simulation in Simulink

In Figure 7.1, the command signal is a step input that is given in millimeters. The step is first converted to voltage before it is compared to the systems response to compute the error. Recall that the input to the transfer function is a value between 0V and 5V. The output of the transfer function is the laser output signal, which also has units of voltage but on a different scale than the input. The laser output is a value between 0V and 10V.

The command signal is compared to the output to create the error signal, which is input to the PID block. The block diagram for the PID system is shown in Figure 7.2. As shown, the error is divided into three separate signals. The top error signal is input to the PID block and is multiplied by the proportional gain, creating the proportional control term. The middle error signal is integrated before it gets to the PID block. This term is then multiplied by the Integral gain to obtain the integral term. Last, the error signal is differentiated in time, and is multiplied by the Derivative gain in the PID block. The resulting control signal is the sum of the Proportional, Integral, and Derivative terms.

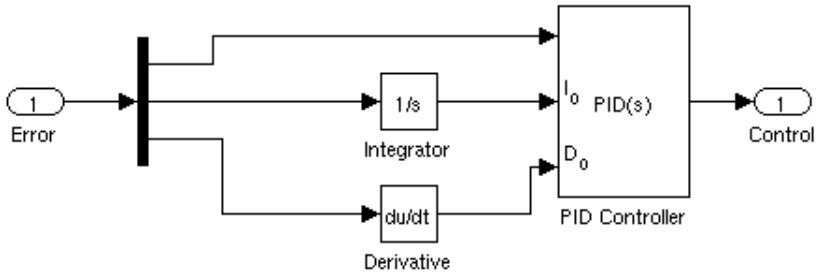

Figure 7.2: Block diagram of the PID control subsystem shown in the block diagram in Figure 7.1.

In Figure 7.1 the control signal is input to the model of the bimorph to obtain the response of the system. White noise is injected into the output of the bimorph to simulate the noise from the laser. After the noise is injected, the output is filtered through a 2nd order Butterworth filter. The filter is designed using the Matlab function *butter.m*, and has a cutoff frequency of roughly 190rad/sec (30Hz). Essentially, the filter smooth's the noisy data by passing only the signals that have a frequency content of 30Hz or less. Figure 7.3 provides the Bode diagram of the Butterworth filter. Once filtered, the measurement signal then completes the loop and is compared with the input signal to create the error.

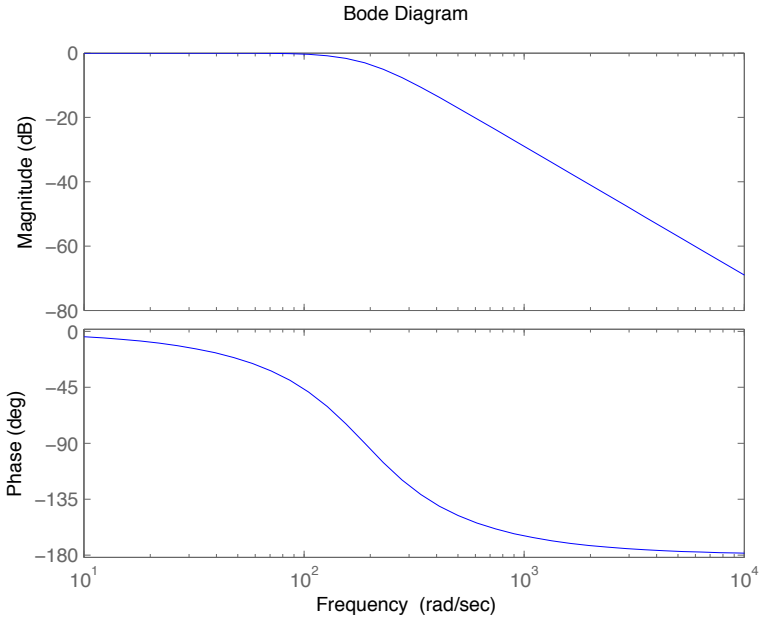

Figure 7.3: Bode plot of a Butterworth filter with 30Hz cutoff frequency

7.1.1 Tuning the PID Gains

The Ziegler-Nichols method was used to tune the PID gains for the simulation. The first step of this tuning method is to increase the proportional gain until the system continuously oscillates, while the integral and derivative gains are zero. K_{cr} is used to denote the *critical* proportional gain, and increasing the proportional gain above K_{cr} causes the system to become unstable. For the simulation, K_{cr} was found to be 0.43, and the figure corresponding to this is given in Figure 7.4 below. The figure shows that a step response leads to sustained oscillations for the bimorph.

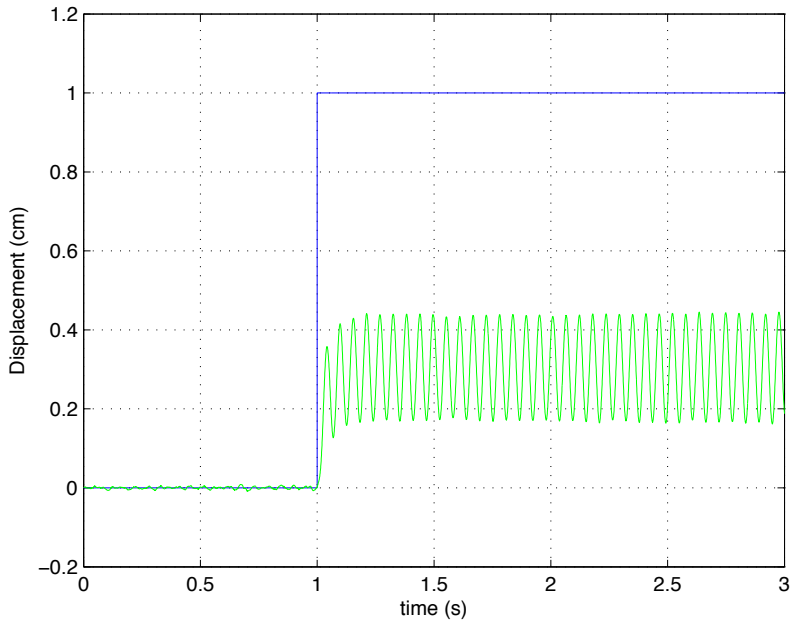

Figure 7.4: Simulated step response of the bimorph actuator with K_{cr} = 0.43

Given K_{cr}, the values for PI, or PID gains can be obtained using the relationships specified by Zeigler and Nichols. For PI control, the following proportional and integral gains are chosen.

$$K_P = 0.45K_{cr}, \qquad K_I = \frac{1.2K_P}{P_{cr}}$$

In the above, P_{cr} is the period of the sustained oscillations in Figure 7.4, which was found to be about 0.055 seconds. Using these values in the PID block in Figure 7.2, and setting the derivative gain to zero, the following step response is obtained. Similarly, the gains for PID control are obtained using the following relationship. Using these values in the PID block, the step response shown in Figure 7.6 was obtained.

$$K_P = 0.6K_{cr}, \qquad K_I = \frac{2K_P}{P_{cr}}, \qquad K_D = 0.125K_P P_{cr}$$

From Figure 7.5 and Figure 7.6, the performance of the closed loop PID control is found. First, from Figure 7.5, the response of the bimorph is fairly slow. The rise time (elapsed time from 0 to 1cm in the step response) is about 1.2 seconds. However, the system settles almost immediately after it rises. Settling time is the elapsed time for the bimorphs oscillations to become less than 5% of the final value.

The full PID control system (Figure 7.6) has a much faster rise time. Specifically, the rise time is about 0.25 seconds. However, the PID system oscillates more than the PI

system, which increases its settling time. Here, the settling time is approximately 0.7 seconds. Even with the increased settling time, the PID systems performance is still better than that of the PI system.

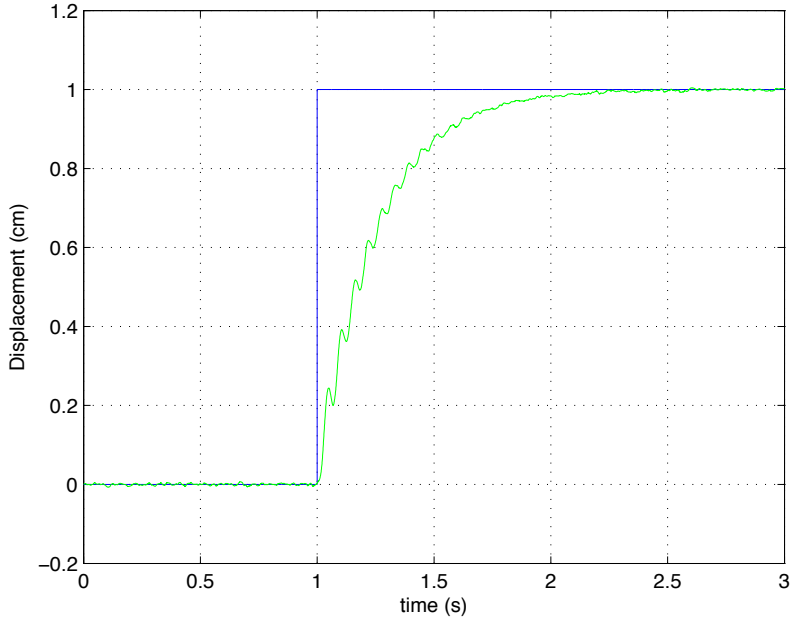

Figure 7.5: Simulated step response of the bimorph with PI control

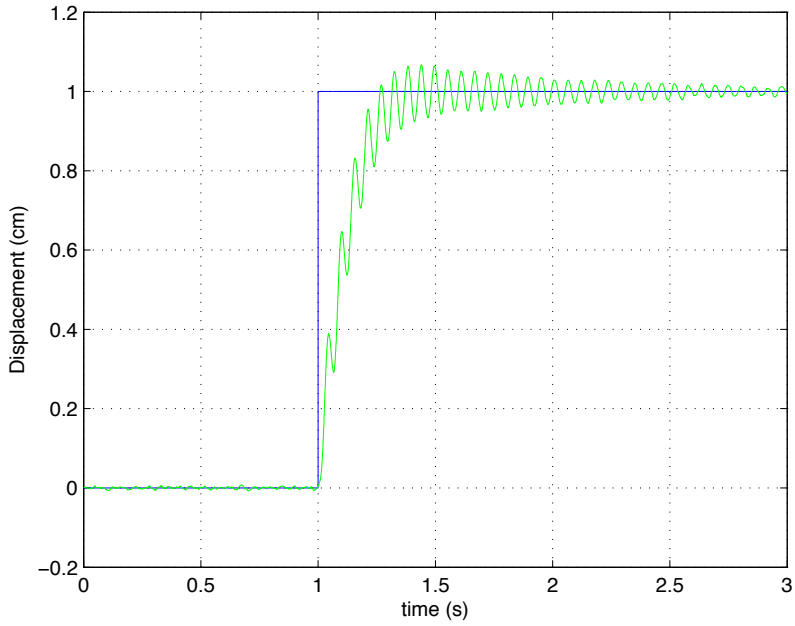

Figure 7.6: Simulated step response of the bimorph with full PID control

7.2 Open and Closed Loop Step Response

After prototyping the control system with simulation, PID control was implemented on the actual cantilevered bimorph. The PID control system was implemented in LabView. The setup for closed-loop control of the bimorph is same setup that was utilized during the frequency response experiments, and is described in Chapter 6.

In this section, results from experiments taken for the 85x28mm active area bimorph are provided. Specifically, this section compares open and closed-loop step response of the cantilevered bimorph. First, the experimental procedure is described, which is followed by the results obtained from the experimental data.

7.2.1 Experimental Procedure

Figure 7.7 provides a diagram of the equipment used during these experiments. The 85x28mm active area bimorph was used for these tests. LabView operates on a laptop computer and is the central hub for the closed loop tests. Using the PID control scheme, LabView commands voltages to the amplifier circuit board, which outputs the high voltages to the bimorph's MFC elements. The bimorph is held in place by a vice that is mounted in the bed of the CNC machine. A laser measurement unit is mounted to the head of the CNC, and the laser focused on the trailing edge of the bimorph. The laser's measurements are sent back to LabView and utilized as the feedback signal for the control loop.

Two different experiments were performed using the setup depicted in Figure 7.7. The first was an open loop step response of the bimorph. A linear relationship was assumed for the input voltage to deflection of the bimorph. Recall that the input voltage (to the AMPS MFC driver board) is a value between 0V and 5V, and 2.5V is the neutral condition for the bimorph. Furthermore, 5V represents the 100% morphing condition of the bimorph, while 0V represents -100% morphing. Because of hysteresis, a linear relationship between input and output is very poor. Without a model of the bimorphs hysteresis, a linear relationship is the best option.

The second experiment performed was a closed loop step response of the bimorph. A closed loop control system was built in LabView similar to the control simulation discussed in Section 7.1. The control system generates the input voltages for the bimorph

in closed loop operation. For these experiments, the step input was given as a value of tip displacement for the bimorph. For example, the bimorph's tip can deflect approximately ±22mm. Here, step inputs were given as 10mm, 20mm, and -10mm, with positive deflection being the free end moving to the left in Figure 7.7. Therefore, the bimorphs tip moves away from the laser in positive deflection, and toward the laser in negative deflection.

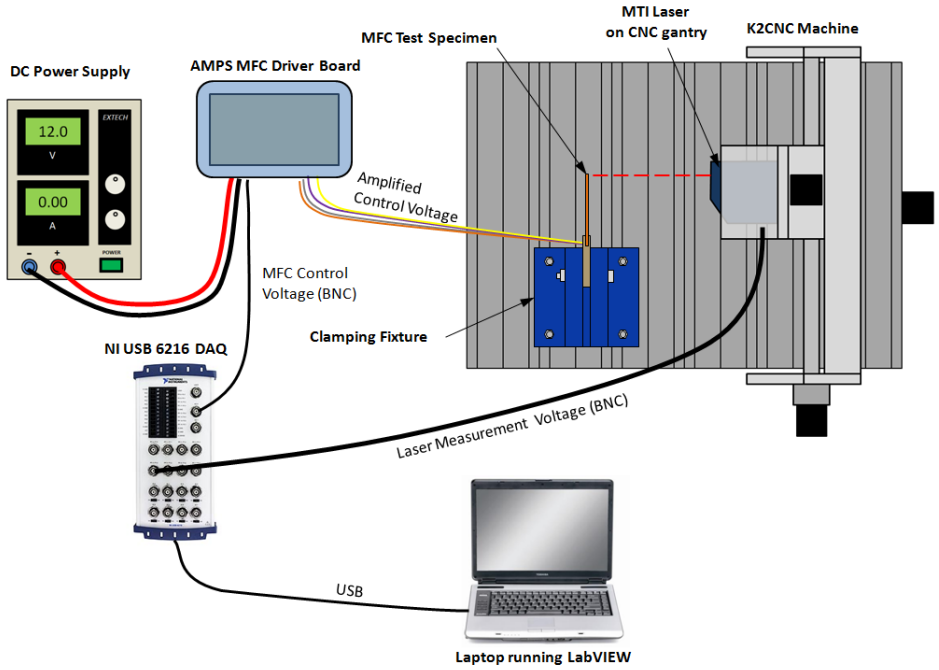

Figure 7.7: Diagram of the setup utilized for the closed loop control experiments performed on the cantilevered bimorph.

7.2.2 Open Loop vs Closed Loop Comparison

Figure 7.8 shows the open and closed loop step response for a 10mm step input. As mentioned above, a 10mm step input means that the desired tip deflection of the bimorph was 10mm. In the figure, the *green* curve is the open loop response data, while *blue* is the closed loop response data. *Black* is the step input, and the *red* lines are the 5% limits for settling time calculations.

From Figure 7.8, one can see that the rise time of the open loop system is much faster than the closed loop system. Specifically, the open loop system's rise time is about 0.05 seconds, while the closed loop system's rise time is about 0.325 seconds. However, it should be noted that the closed loop system settles in about one second, while the open

loop system does not settle. During these experiments, it was found that the bimorphs experience a second nonlinear behavior known as creep. Other authors have documented the bimorph's creep effect [52,53]. The authors show that the creep is an effect of supplying the bimorph with a constant voltage. The creep behavior makes it difficult to compare the open and closed loop system, because the open loop bimorph will never settle to the desired deflection.

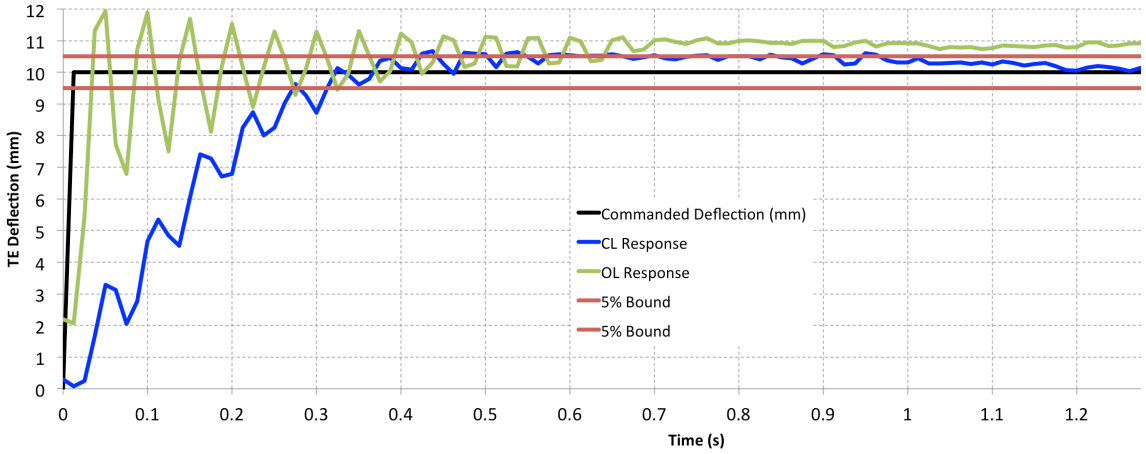

Figure 7.8: Open and closed loop step response for a 10mm step input

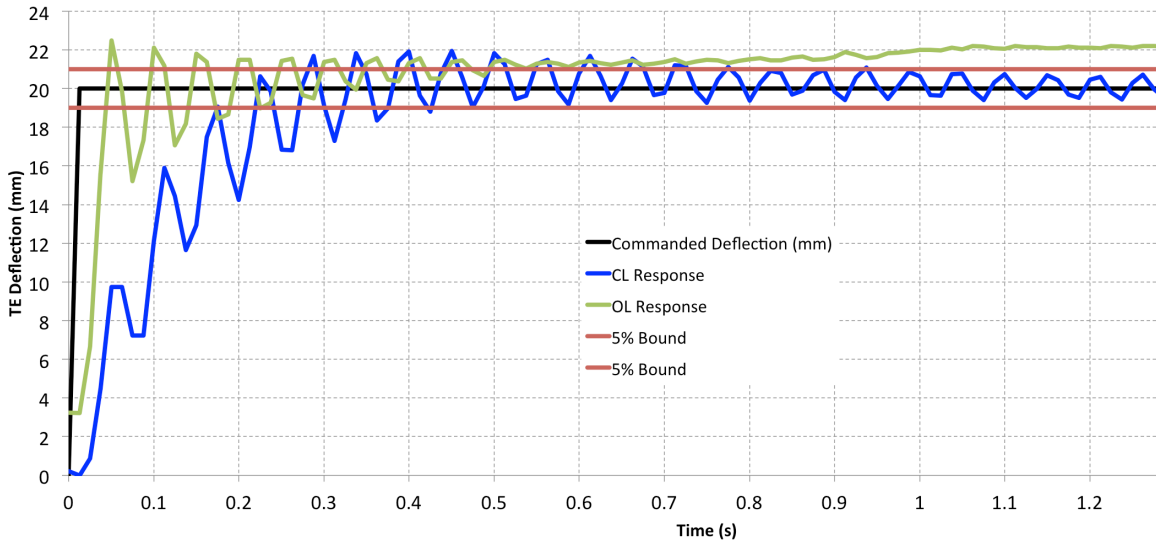

Figure 7.9: Open and closed loop step response for a 20mm step input

Figure 7.9 shows the open and closed-loop responses of the cantilevered bimorph for a 20mm step input. The results from this test are similar to those found for the 10mm step input. Again, the rise time of the open-loop system is about 0.05 seconds, while the

rise time for the closed-loop system is about 0.225 seconds. Furthermore, the open-loop system does not settle due to the creep exhibited by the bimorph in open-loop operation.

Finally, Figure 7.10 shows the open and closed-loop step response of the cantilevered bimorph for a -10mm step input. This figure shows why the bimorph is difficult to use in open loop operation. As can be seen, the open loop response neither rises nor settles to the desired -10mm tip deflection. The initial response is too shallow due to the bimorph's hysteresis. Here, the commanded voltage was not enough for the bimorph to achieve the desired 10mm step. This is due to the linear voltage to deflection relationship, which is inaccurate due to the bimorph's hysteresis.

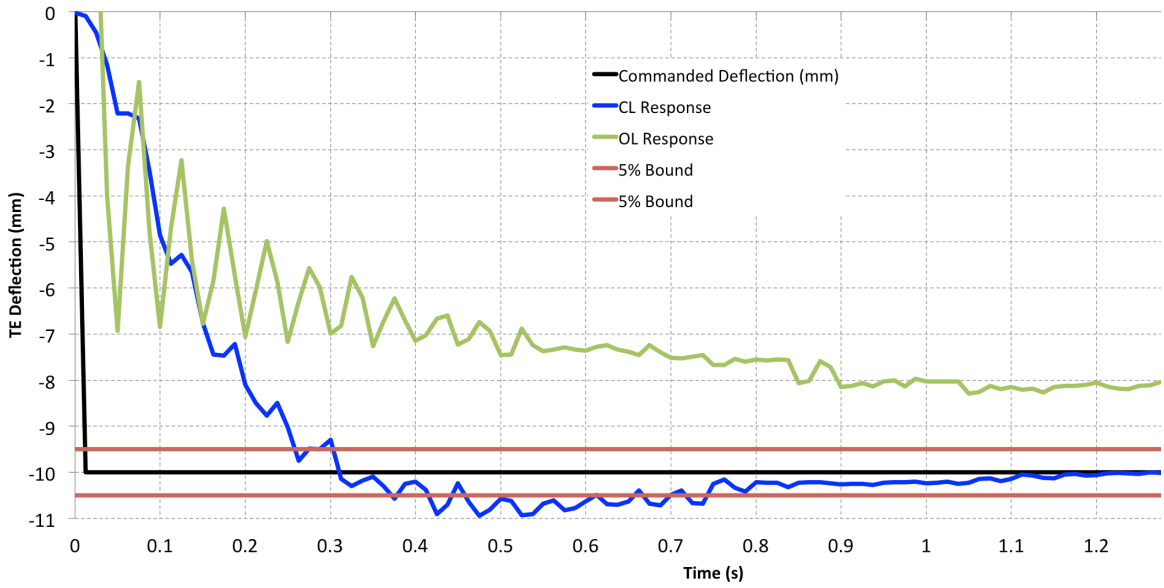

Figure 7.10: Open and closed-loop step response for a -10mm step input.

The figures above show some benefits and costs of closed loop control. The closed-loop control will be more accurate and robust to disturbances at the cost of a slower response time. It is believed that the speed of the response can be improved, but a method to do so is not investigated within this thesis. Improving the response time of the closed loop system will be investigated in future work on the subject. One potential method to improve the response time is by developing a hysteresis model of the bimorph. The hysteresis model can be used to reshape the input to the bimorph so that the desired deflection is achieved. Some of these methods are discussed in the following section.

7.3 Other Control Implementations

In the previous section, PID control was implemented to control the trailing edge deflection of a cantilevered bimorph. These sections showed that feedback control is a viable solution to control the bimorph. However, one challenge of implementing closed loop control lies in the choice of the sensor. In the previous section, the bimorph was controlled and tested in a lab, using a laser as the feedback sensor. This is a very accurate and high-bandwidth sensor, but is not feasible for use on MAVs.

Currently, the targeted vehicles for bimorph actuation are small UAVs and MAVs. Finding a sensor to provide feedback presents a major challenge. This section presents some potential implementations of bimorph control on ducted fan MAVs. Specifically, potential sensors and their impacts on vehicle design are discussed.

In some of the earlier chapters, it was also mentioned that bimorphs are potentially a better substitute to servo actuation. However, Section 7.2 showed that in closed loop operation, bimorphs have response times that are slower than that of a servo. The response time of the bimorph was approximately 0.3 seconds, while servos have response times of roughly 0.1 seconds. However, it is shown in Chapter 3 that the bimorph can actuate at higher bandwidths than servos. Therefore, some possibilities are discussed to use model inversion techniques to control the bimorphs. To do this, an accurate model of the bimorphs hysteresis is required.

In the following subsections, two topics are discussed. First, sensors are discussed that are potential candidates for closed loop implementation on a ducted fan MAV. Some benefits and challenges for each sensor are discussed. Second, some inversion based control techniques are discussed that could allow the bimorphs to be controlled by open loop only. Methods will be outlined to model the bimorph's hysteresis, along with methods to model and invert the creep seen for bimorphs in open-loop operation.

7.3.1 Potential Sensors and Implementation

Implementing bimorph actuators on ducted fan MAVs presents some interesting challenges. One challenge is the reliance on a sensor to measure the morphing condition of the bimorph. Due to the bimorph's nonlinear behaviors (hysteresis and creep), the

bimorph cannot be used in open loop operation. This is especially true for ducted fan vehicles, which are unstable and have a time to double of less than 1 second [6].

In the following, four different sensors are discussed. The emphasis here is implementation of the bimorph on ducted fan MAVs. It is likely that better sensors exist than those discussed, and these are not intended to be an all-inclusive list. Those mentioned here are only some candidates that the author has visualized.

The four potential sensors are: using the vehicle as a sensor, a potentiometer, an angle sensor, and using an MFC as a sensor. The benefits and costs of each of these sensors are discussed.

Sensing by Vehicles State

The best sensor solution to provide feedback of the bimorphs state is one that is low weight, small, has low power draw, and is inexpensive. The optimal solution is then to use sensors that are already available onboard the vehicle. Ducted fan MAVs are typically outfitted with sensors to measure the vehicles state. Specifically, an Inertial Measurement Unit (IMU) and GPS will likely be onboard the vehicle. The idea here is to use the measured vehicle state to identify the morphed state of the bimorphs. For example, assume the vehicle is desired to hover, which is associated with a very specific vehicle state. The vehicle's sensors measure deviations from the hover state. A command is then generated to restore the vehicle to hover, and the bimorph actuators execute the command. However, because of hysteresis, the bimorphs may not precisely execute the commanded deflection. Therefore, the commanded vane deflections may not return the vehicle to hover, and the process is repeated.

The benefit of this method is that no additional sensors are required. However, there are many costs associated with this approach. First, very accurate wind tunnel data is required to model the vehicle and the bimorph control surfaces. Specific vehicle states must be accurately associated with control surface positions. Aerodynamic data is required to map control surface positions to the vehicle state, which will require extensive aerodynamic data.

Second, this system will likely introduce a lag in the overall vehicle bandwidth, which may have a destabilizing effect on the vehicle. The vehicle is commanding its control surfaces based on the mapping mentioned above. If the control surfaces are out

of position, the vehicle must make additional corrections. This will manifest itself as either lag, or limit cycle oscillations.

This method is a possible control implementation, but is not very realistic for use with ducted fan MAVs. This method may also be more applicable to fixed wing or stable vehicles. Furthermore, this method requires large development times and accurate aerodynamic data of the vehicle, both resulting in high cost and man-hours. While this method may not be a realistic "stand-alone" control method, it has the potential to be used in conjunction with another form of control to add robustness and redundancy to the vehicle. This is discussed later in Section 7.3.2.

Sensing by Potentiometers

Potentiometers can be used to determine the morphing condition of the bimorph actuator. A potentiometer is thought of as a variable resistor, and a typical angular potentiometer is shown in Figure 7.11. Assume the two outer leads of the potentiometer (terminals *A* and *B*) are connected to ground and 5V(DC), respectively. The middle lead (*W*) is known as the wiper, and is the output of the potentiometer. The measured voltage on the wiper channel is a linear relationship that is dependent on the angular position of the wiper. When turned to the left, the voltage on the wiper lead is 0V (ground). On the contrary, when turned completely to the right, the wiper channel is 5V.

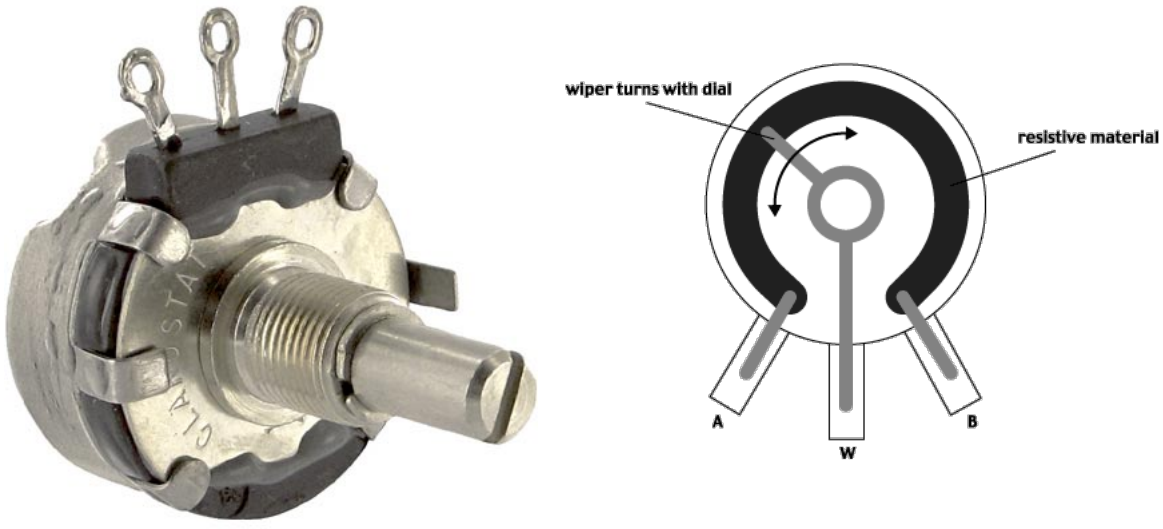

Figure 7.11: (Left) Image of a standard potentiometer; (Right) sketch of a potentiometer.

To understand how a potentiometer could be used as a sensor for the bimorph, first recall the description of the bimorph and linkage concept from Chapter 3. Figure 7.12 provides a picture and cross-section sketch of the bimorph and linkage concept.

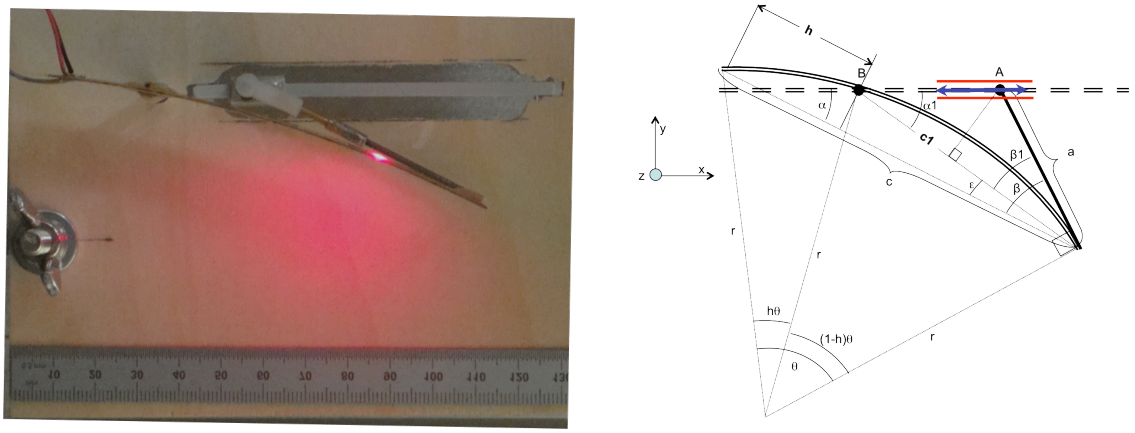

Figure 7.12: (Left) Image of the bimorph and linkage concept during testing, (Right) cross-section view of the bimorph and linkage to show their interactions.

In Figure 7.12, the left is a picture of the bimorph and linkage, and the right is a cross section view of the bimorph and linkage to illustrate the geometry. Recall that the bimorph is free to rotate about its axle, located at point *B* in the figure. An angular potentiometer place at point *B* and connected to the axle can sense the rotation of the bimorph. This gives direct feedback of the morphing condition of the bimorph.

Similarly, a linear potentiometer could be used for the slot shown in Figure 7.12. A linear potentiometer would take the place of the slide in Figure 7.12 (left). The end of the linkage at point *A* would then be connected to the potentiometer. The deflection of the trailing edge then causes the linkage to move, which causes point *A* to traverse in the slot. In this way, the morphing condition of the actuator can be deduced. But, this method is poorer than using the angular potentiometer because the morphing direction is not known. For the linear potentiometer to work, the input signal would need to be used to determine the morphing direction of the bimorph.

The advantages to using the potentiometers for feedback are that they are inexpensive, very lightweight, and reliable. One disadvantage of potentiometers is that they are stiff to turn due to internal friction. This stiffness will cause the bimorph and linkage system to behave more sluggishly. Specifically, this fact eliminates the possibility of using a linear potentiometer in the slot. For the slot to work properly, the

slide should be as frictionless as possible. Another disadvantage associated with potentiometers is that they need a power source, and three wires must be run to each potentiometer on the vehicle. For ducted fan MAVs, at least four potentiometers are required (one for each control surface). Each potentiometer requires three wires, which is a minimum of 12 wires.

Angular Position Sensor

Another candidate sensor is an angular position sensor. The angular position sensor is a type of rotary encoder that measures the rotation of a shaft. The idea for this sensor is essentially the same as the angular potentiometer discussed in the previous subsection. The angular position sensor would measure the rotation of the bimorphs axle at point *B* in Figure 7.12. The benefit to using an angular position sensor is that it is a non-contact sensor. Therefore, the angular sensor would not contact the axle, and not prohibit the bimorph's motion. Although, this sensor still requires wires, like the potentiometers.

Sensing by MFC Elements

The most promising sensor is to use an additional bimorph as a sensor, like the one shown in Figure 7.13. The large MFC area is utilized for actuation, while the slender MFC area is used for sensing. There are many benefits to using an additional bimorph as a sensor. First, the sensor is integrated directly with the actuator. This is opposed to the angular sensors mentioned above, which measure the rotation of a shaft. Second, using an MFC as a sensor allows for fewer complications. For example, the angular sensors mentioned above require proper alignment with shafts, they must be mounted to a fixed surface, and extra wire must be ran to both power and read them. The bimorph sensor eliminates the alignment and mounting issues, because the assembly is an off the shelf part. The sensor MFC also requires wires. However, wires must also be routed to the actuator MFC elements. Fortunately, the wires can be routed together and not separately as with the angular sensors.

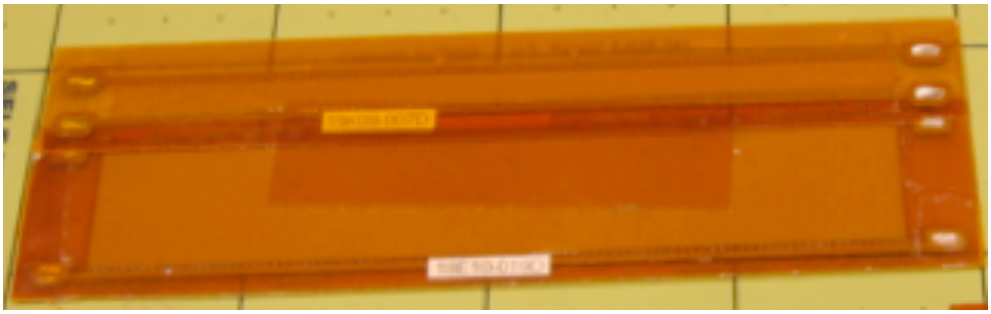

Figure 7.13: 85x15mm MFC element with 85x3mm MFC for sensing.

7.3.2 Hysteresis Inversion and Implementation

As mentioned earlier, the best sensor is one that is lightweight, low power draw, low cost, and small in size. While this statement is true, the absolute best case is to *eliminate* the need for a sensor altogether. To do this, the bimorph must be capable of open loop operation. It has been stated throughout this thesis that because of hysteresis, the bimorph is incapable of open loop operation. However, some researchers have investigated modeling the bimorphs hysteresis to achieve a form of open loop control [52,53,54]. Specifically, researchers have investigated modeling the bimorph's hysteresis, so that the inverse of the hysteresis model may be computed. Given the inverse of the hysteresis model, the input voltage to bimorph may then be reshaped so that the bimorph behaves linearly.

This subsection is broken down into 3 parts. First, the modeling techniques to model the hysteresis of the bimorph are discussed. Next, the inversion based open loop control method is discussed. Finally, the benefits and costs of this form of control are discussed. Some interesting points are shown that may restrict the use of this control method on ducted fan UAVs.

Modeling Hysteresis

Several authors have researched the open loop control of bimorphs. Namely, Rakotondrabe *et. al.* [52], and Lining and Changhai [53,54], have studied this problem. Essentially, the idea is to model the hysteresis of the bimorph actuator with empirical data. Lining *et. al.* [54] models the hysteresis curves with 3rd order polynomial fits. This is shown in Figure 7.14. The modeled hysteresis results in a set of equations that represent the bimorph's response (TE deflection) versus the input voltage. By inverting

the hysteresis model, one then obtains a set of equations that map a desired TE deflection to a voltage input.

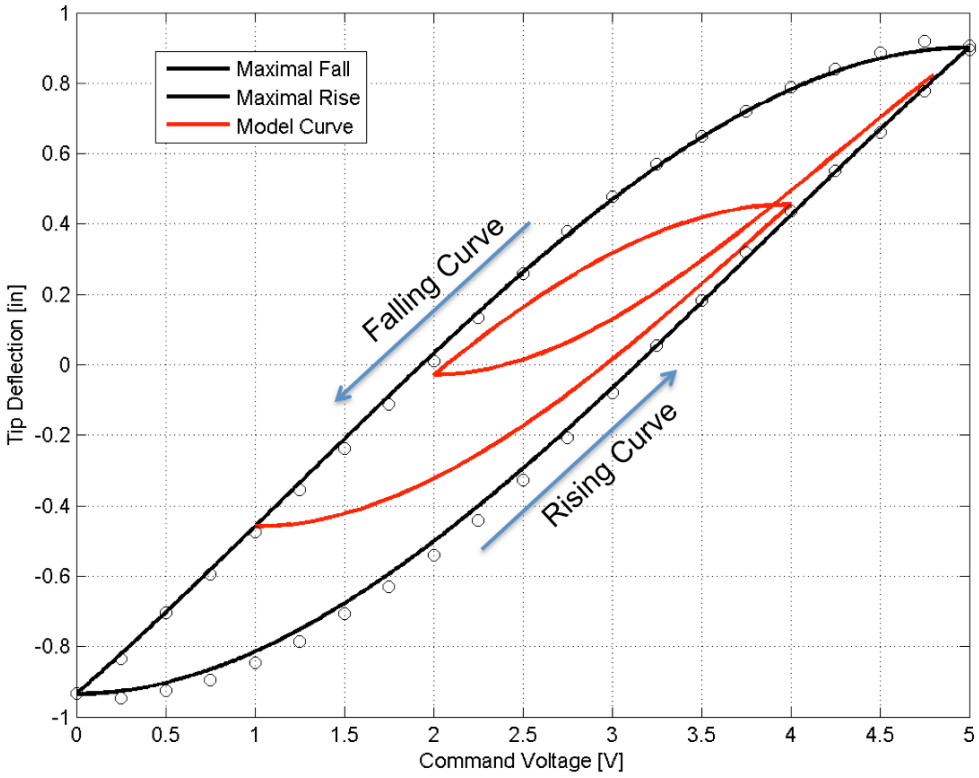

Figure 7.14: Modeled hysteresis curves for the cantilevered bimorph with 85x28mm active area MFC elements.

In the figure, the circles are measured data points from the cantilevered bimorph (85x28mm MFC elements) that is described in Chapter 3. The outer black curve represents the polynomial fit of the measured data. Furthermore, the outer curve is known as the maximal rising and falling curves of the TE deflection, while the red curve represents an inner hysteresis loop. Here, maximal means that the input was varied between its two maximal points. If the input voltage switches direction before reaching the maximal or minimal values, the deflection will follow a curve similar to the red curve shown in the figure. Thus, the red curve is termed an inner hysteresis loop. The equation used for the polynomial fit to the measured data is provided below. Note that this approach is the one taken by Lining *et. al.* [54].

In Equation 7-I, P_n is the equation for the maximal rising curve and D_n is the equation for the maximal falling curve, and u is the input voltage and a function of time. As can be seen, the equations for the rising and falling curves of the hysteresis are

modeled as 3rd order polynomials. Given the equations for the maximal curves, the inner hysteresis curves are then assumed to be linearly proportional to the maximal curves. The equations below help solidify this idea.

$$P_n(u(t)) = \sum_{i=0}^{3} a_i u^i(t)$$

$$D_n(u(t)) = \sum_{i=0}^{3} c_i u^i(t)$$

Equation 7-I

$$y(t) = P_i(u(t)) = kP_n(m(u(t) - U_n) + U_n) + b$$

Equation 7-II

In Equation 7-II, the resulting deflection on an internal rising curve P_i is a linear relationship with the maximal rising curve P_n. In the equation, y denotes the trailing edge deflection of the bimorph and P_i is an internal rising curve. The command input is again u, while U_n is the maximum input voltage that can be commanded to the bimorph (in this case 5V). Lastly, k, m, and b are linear coefficients that scale the inner rising curve and are defined in Equation 7-III, Equation 7-IV, and Equation 7-V.

$$m = \frac{U_n - U_i}{U_n - U_0}$$

Equation 7-III

$$k = \frac{y_{max} - P_i(U_i)}{y_{max} - y_{min}}$$

Equation 7-IV

$$b = P_i(U_i) - ky_{min}$$

Equation 7-V

In the equations, U_0 is the minimum input voltage that can be commanded to the bimorph (0V in Figure 7.14), and y_{max} and y_{min} are the maximum and minimum TE deflections that the bimorph can achieve. These values for the bimorph are approximately ±0.9 inches. Lastly, U_i denotes what is known as the turning voltage, which is the value of the input voltage when it last changed direction. Therefore, this value denotes when the TE deflection changes from a falling curve to a rising curve, or

vice versa. Finally, the equation for internal falling curves can be written similarly to Equation 7-II.

$$y(t) = D_i(u(t)) = kD_n(n(u(t) - U_n) + U_i) + b$$
$$n = \frac{U_i - U_0}{U_n - U_0}$$

Equation 7-VI

Inverse Hysteresis Control

Once the bimorph's hysteresis has been modeled, the equations can be inverted to obtain the inverse model mentioned earlier. Therefore, the independent variable of the equations is deflection (y), and the dependent variable of the equations is the command voltage u. Essentially, a desired deflection is input to the equation, and the result is the reshaped input voltage required to achieve that deflection. By applying this inverse model, the input to the bimorph is reshaped so that the output is linear with respect to the input. This idea is better visualized with the flow diagram in Figure 7.15.

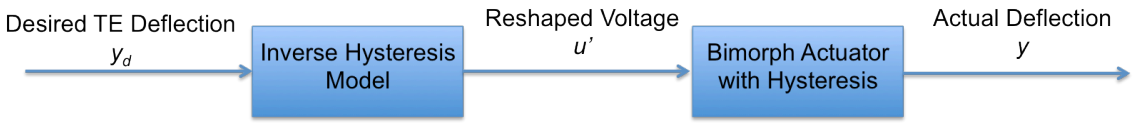

Figure 7.15: Block diagram illustrating how the inverse hysteresis model is used to reshape the input to the bimorph.

By using the inverse hysteresis model, the resulting bimorph deflection is much closer to the desired deflection. The authors mentioned above have implemented this method with good success. In [54], the authors claim to have achieved a relative tracking error of less than 1%, as compared to a 12% error in pure open loop control. However, there are some issues that rise concern. For example, significant modeling is required to use the actuator for each specific application. More of the benefits and costs are discussed in the following subsection.

Benefits and Concerns of the Inverse Hysteresis Model

The previous subsections highlighted research performed to accurately control the position of a bimorph actuator with open loop control. Specifically, a model of the bimorph's hysteresis is inverted to reshape the input voltage to the bimorph. The largest

benefit of using an open loop control scheme is that the need for a sensor is negated. This means that the overall system becomes less complex. The researchers showed that this method resulted in accurate control within a lab setting. However, the research presented here deals with implementing the bimorphs on aircraft. Therefore, the bimorphs are far removed from the laboratory setting.

The first issue that arises is that the hysteresis information must be measured in a wind tunnel setting. It is not known how the dynamic pressure of airflow over the bimorph will affect its output, but it is hypothesized that this will reduce the amount of deflection that the bimorph achieves. If this is the case, the actual hysteresis loop will be much different from data collected under no loads. For ducted fan vehicles, the hysteresis loop will likely change the fan speed and atmospheric conditions. This means that significant modeling is required to obtain an accurate model of the hysteresis for most of the vehicles flight conditions. In short, the output of the bimorph is now a multi-variable function that will take a form like that shown in Equation 7-VII.

$$\alpha = f(u(t), q(t))$$

Equation 7-VII

$$q = \frac{\rho V^2}{2}$$

Equation 7-VIII

Equation 7-VII presents the angle of attack (α) as a function of the input voltage to the bimorph (u) and the dynamic pressure on the bimorph (q). The equation for dynamic pressure is provided in Equation 7-VIII. In the equation, V is the air speed over the bimorph, which is the exit velocity of the duct. Lastly, ρ is the air density.

Recall from Chapter 5 that it was shown that the relationship between input voltage and angle of attack for a bimorph is hysteretic. Here, computing the inverse of a multi variable function is more difficult than inverting a 3rd order single variable function. It is likely that look-up tables would be used as the onboard model of hysteresis if this method were ever flown on a vehicle. The addition of aerodynamics complicates the use of the inverse hysteresis method, but it still my have some advantages.

First, there are some possibilities that using this model will increase the response time of the closed loop step response. Section 7.2.2 shows that the response time of the

closed loop bimorph is relatively slow. This is partially due to the use of a linear mapping between voltage and bimorph deflection. Because of hysteresis, a linear model is poor. By including the inverse hysteresis model in the closed loop path, the response time may be decreased. Future work will investigate this hypothesis.

Second, recall from Section 7.3.1 the closed loop control strategy of using the vehicle as a sensor. One possible control implementation could be a hybrid open/closed loop one where both of these ideas are utilized. The initial response of the bimorph is defined purely by the inverse hysteresis model, while the vehicles sensors are used to generate commands that ensure the vehicles remains in a desired state.

8. Conclusions

The following presents a summary of the conclusions that are shown throughout this thesis. In Chapter 1, it is mentioned that the aim of this research is to characterize the performance of the novel bimorph and linkage concept. Hence, this chapter summarizes the conclusions that are found to meet that end. The bimorph and linkage concept is shown in Figure 8.1.

To characterize the performance of the bimorph and linkage concept, experiments were performed to measure the amount of angle of attack this device can achieve. Thus, the first section of this chapter presents the results and conclusions found during those experiments. From these results, it is inferred that the bimorph and linkage concept achieves greater angles of attack than a cantilevered bimorph. However, the bimorph's hysteresis requires closed loop control to precisely control angle of attack. Therefore, the next section discusses the results obtained from modeling and control of the bimorph actuator. It is shown that while the bimorph has a higher actuating bandwidth than a servo, the closed loop system tested during this research has a slower response time. Lastly, further work is required to fully answer the original aim of this research. Therefore, the final section of this chapter is devoted to the future work that yet remains to fully characterize the bimorph actuators.

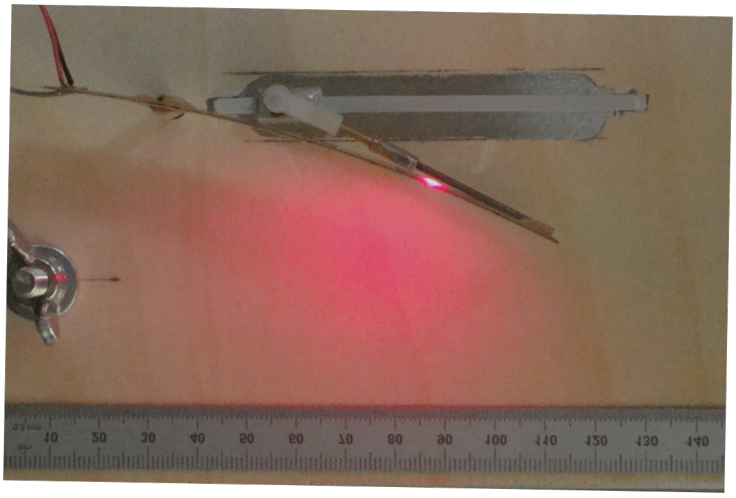

Figure 8.1: Picture of the bimorph and linkage concept taken during steady state experiments.

8.1 The Bimorph and Linkage Concept

During this research, a device was built that is termed the bimorph and linkage concept. This device is shown in Figure 8.1 and is described in Chapter 3 of this thesis. In essence, a linkage is attached to the bimorph so that larger angles of attack are achieved as opposed to a cantilevered bimorph. Experiments were conducted to investigate the amount of angle of attack these specimens can achieve. Figure 8.2 depicts the amount of angle of attack that the cantilevered bimorph achieves. Additionally, Figure 8.3 depicts the bimorph and linkage angle of attack versus input voltage. As is shown, the bimorph and linkage reaches angles of attack that are nearly twice those achieved for the cantilevered case. The steady state experiments and results are better described in Chapters 4 and 5.

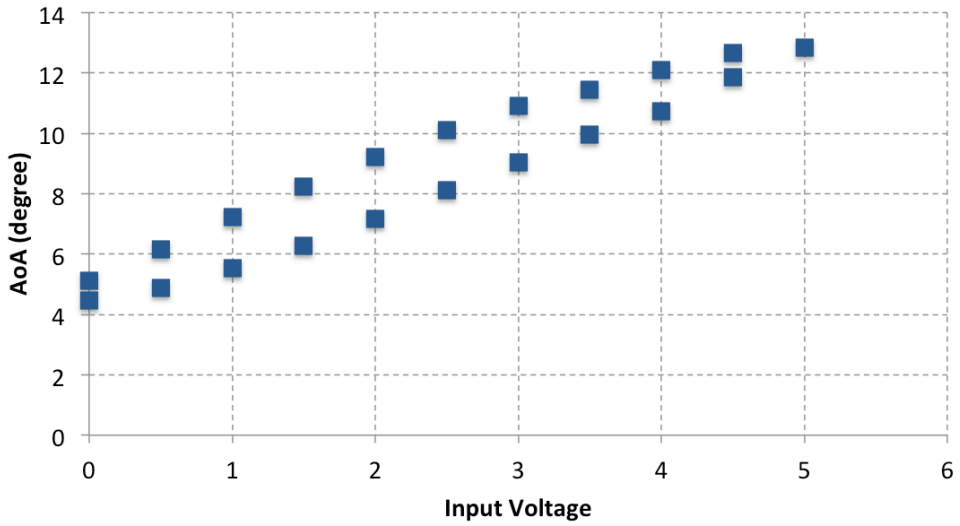

Figure 8.2: Cantilevered bimorph angle of attack versus input voltage.

The figures show that the angle of attack of the bimorphs is a hysteretic process, which is why the relationship between angle of attack and input voltage appear as a loop. Hysteresis is a form of nonlinear behavior in which the current angle of attack is dependent on both the current input and the previous input *history*. Because of hysteresis, the bimorph cannot be controlled in a purely open loop sense. Thus, feedback control is required to control the angle of attack, which is the topic of the following section.

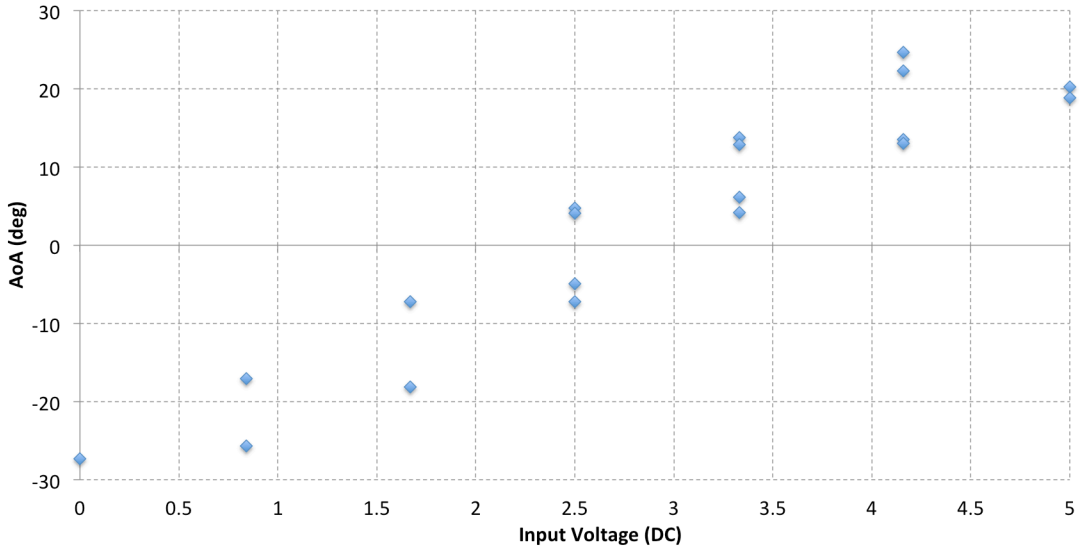

Figure 8.3: Bimorph and linkage angle of attack versus input voltage.

8.2 Controlling the Bimorph

Two tests were performed to characterize the bimorphs dynamic behavior. First, frequency response tests were preformed and the bimorph is modeled using a transfer function. Note that the transfer function obtained is not an accurate representation of the bimorph. This is because the transfer function assumes a linear, time invariant system. As mentioned in Section 8.1, the bimorph is not a linear actuator because of hysteresis. However, preforming the frequency response experiments also provide information into the bimorph's actuation bandwidth. The frequency response tests and results are better described in Chapter 6.

Once the model of the bimorph was obtained, it was used to design a control law for the bimorph. A Proportional-Integral-Derivative control system was used in simulations to control the deflection of the bimorph's trailing edge. The simulation was used to tune the control gains, which were then used for closed loop control tests. The simulation and closed loop control experiments are described in Chapter 7. The following subsections present the conclusions from both the frequency response, and closed loop control experiments.

8.2.1 Frequency Response

Frequency response experiments were performed on both a bimorph actuated wing section and a servo actuated wing section. The wing sections are described in Chapter 3 of this thesis. A servo was used for the baseline of comparison because servos are the state of the art for control actuation on small UAVs and MAVs. Figure 8.4 below shows the frequency response of the servo actuated wing section, while Figure 8.5 provides the frequency response of the bimorph actuated wing section. As can be seen, the bimorph is capable of actuating at frequencies that are much higher than a servo. This is a favorable result for bimorph actuators when concerned with using the devices on ducted fan vehicles. As mentioned in Chapter 1, ducted fan vehicles are unstable with times to double of approximately 1 second [6]. Therefore, faster actuator control is advantageous.

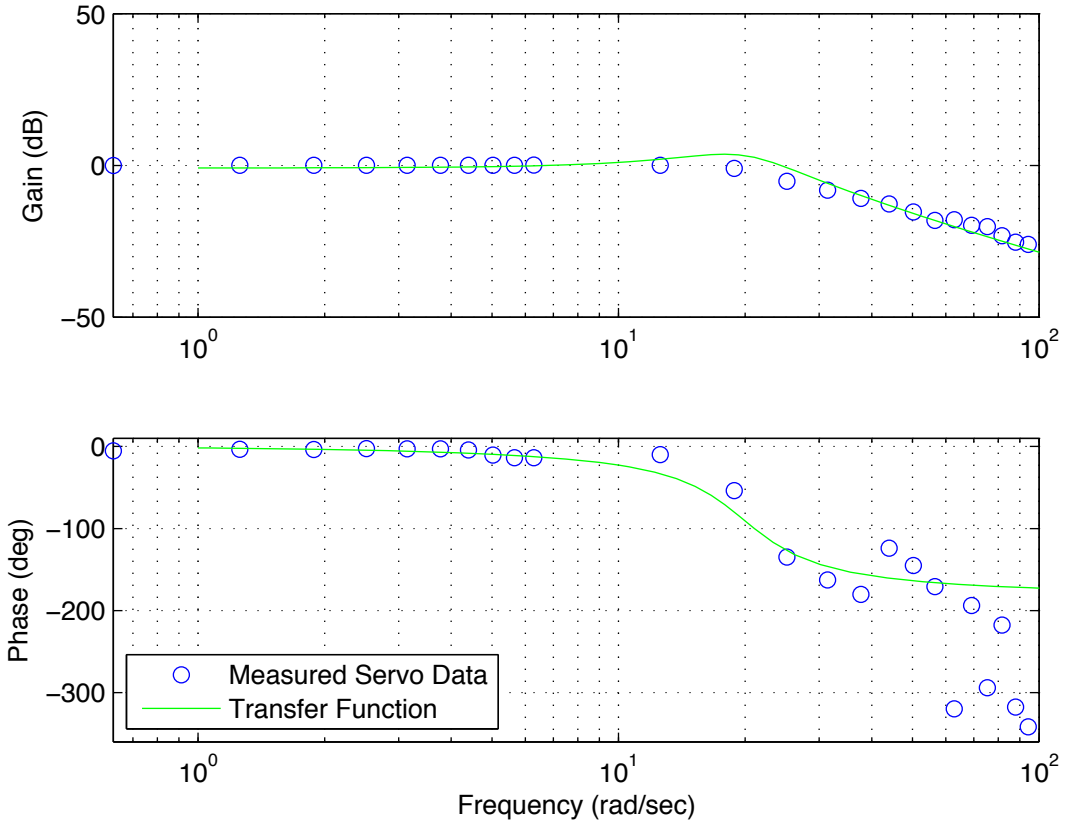

Figure 8.4: Bode diagram for the servo actuated wing section. This material is presented in Chapter 6.

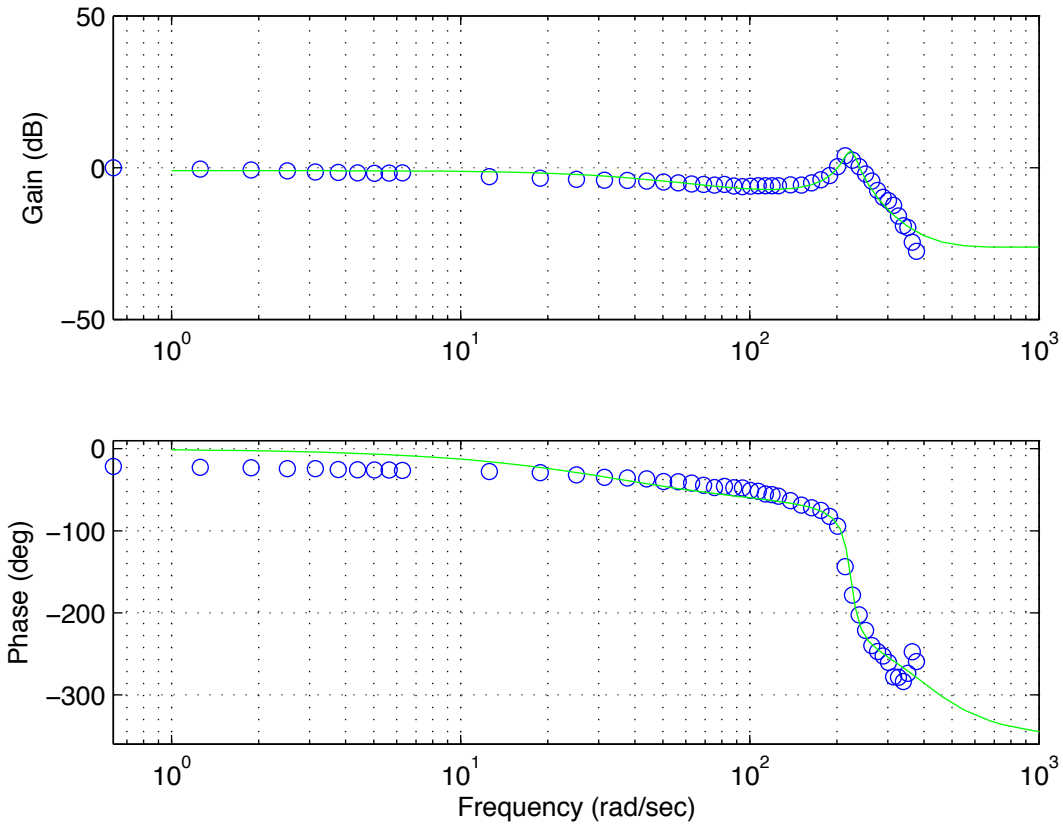

Figure 8.5: Bode diagram for the bimorph actuated wing section. This material is presented in Chapter 6.

8.2.2 Closed Loop Control

Closed loop control was implemented on a cantilevered bimorph in a laboratory, and the bimorph was under no loads during testing. The control gains were originally tuned using a simulation and based on a transfer function model. The model was obtained from a frequency response of the bimorph. Figure 8.6 shows the results of a step response for the cantilevered bimorph in open and closed loop operation. As can be seen, the response time of the bimorph is approximately 0.3 seconds, which is slower than anticipated. For reference, the response time of a standard servo is approximately 0.1 seconds. Future work will be devoted to tuning the control gains so that better transient response times are obtained. Additionally, the results found during the step response tests solidify the fact that the bimorph requires closed loop control for precise actuation. As is shown in the figure, the open loop bimorph overshoots the desired value and never returns. Figure 8.7 depicts another step response in which the open loop bimorph undershoots, and never settles to the desired deflection.

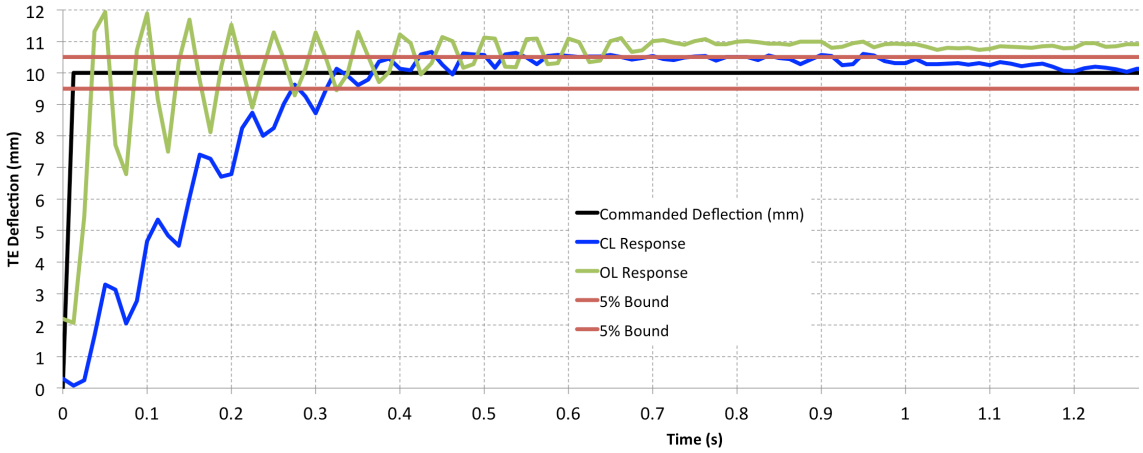

Figure 8.6: Positive step response of the bimorph in open and closed loop operation. This material is presented in Chapter 7.

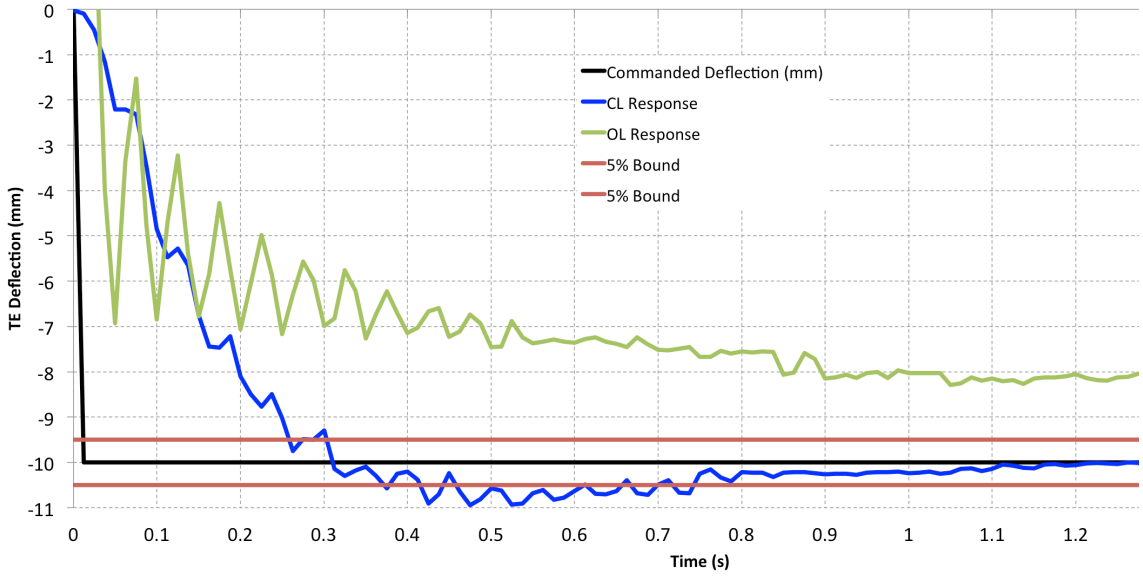

Figure 8.7: Negative step response of the bimorph in open and closed loop operation. This material is presented in Chapter 7.

8.3 Future Research for Bimorph Control

The intention of this research was to determine if the bimorph and linkage concept is a feasible substitute to rigid control surfaces that are actuated by servos. To fully answer this question, a multi disciplinary approach must be taken which was outside the scope of this thesis. In this section, some of the remaining research is outlined.

First, the approach taken for this research was from vehicle and actuator control standpoint. This thesis covers many of the challenges and hurdles but there are still some

stones that must be overturned. As mentioned in Section 8.2, the closed loop response time of the bimorph is slower than expected. This hurdle must be overcome to ensure that these devices are feasible for use on ducted fans. Here, a different control approach than PID may result in a faster response. There also exists a possibility of modeling the bimorph's hysteretic behavior. The hysteresis model can then be used to improve the response time of the bimorph. This is covered in more detail in Chapter 7.

Secondly, aerodynamics was neglected throughout this research, but will have a large impact on the bimorph and linkage actuator. One possible effect of aerodynamics is lower achievable deflections of the bimorph actuator. This would result in lower angles of attack than the values presented in this thesis. Another effect of aerodynamics is slower actuation bandwidth. The aerodynamic drag on the bimorph could manifest itself as phase lag and decreased actuation bandwidth.

Third, structural deformations were also neglected throughout this research. The aerodynamic forces and moments acting on the bimorph and linkage will likely cause structural deformations of the linkage. Thus, research must be conducted to determine the amount of deflection that the linkage can stand before the performance of the bimorph degrades. In this research, the linkage element was assumed to be rigid. However, when the linkage bends under aerodynamic loading, it will likely reduce the amount of achievable angles of attack. Also, the linear slide and bearings were not well designed. The slide is shown in Figure 8.1. Mechanical and structural design must be performed to obtain an optimal slide and bearing to achieve the lowest resistance. Friction in the slide will also reduce the achievable angle of attack, and also affect the systems bandwidth.

Finally, weight is a major consideration for ducted fan UAVs and MAVs. In future research, studies should be performed to determine the weight impact that the bimorph and linkage will have on the vehicle. As mentioned in Chapter 3, the bimorphs require high voltages for actuation. This means that amplifying circuitry must also be onboard the vehicle. Further research in the area of design must be performed to assess the impact of the weight of the bimorph and linkage control versus traditional hinged control surfaces.

9. Bibliography

1. J. G. Leishman, *Principles of Helicopter Aerodynamics*, Cambridge University Press, 40 West 20th Street, New York, NY, 10011, USA, 2000.

2. B. W. McCormick, *Aerodynamics of V/STOL Flight,* Dover Publications, 1999.

3. F. H. Gern, D. J. Inman, and R. K. Kapania. Computation of Actuation Power Requirements for Smart Wings with Morphing Airfoils, AIAA/ASME/ASCE/AHS/ASC Structures, Structural Dynamics & Materials Conference, Denver, CO, April 2002.

4. R. Solecki and R. J. Conant, *Advanced Mechanics of Materials*, Oxford University Press, 198 Madison Ave., New York, NY, 10016, 2003.

5. J. Fleming, T. Jones, W. Ng, P. Gelhausen, and D. Enns. Improving Control System Effectiveness for Ducted Fan VTOL UAVs Operating in Crosswinds, AIAA "Unmanned Unlimited" Systems, Technologies, and Operations, San Diego, CA, September 2003.

6. Stiltner, B., Cotting, M. C., and Ohanian, J., *Derivation and Analysis of the Equations of Motion for a Ducted Fan UAV*, AIAA Atmospheric Flight Mechanics, Portland, OR, Aug 8-11, 2011.

7. R. A. Hess and T. M. Ussery. Sliding mode techniques applied to the control of a micro-air vehicle. AIAA Guidance, Navigation and Control Conference, Austin, TX, August 2003.

8. R. Hess and M. Bakhtiari-Nejad. Sliding-mode control of a nonlinear model of an unmanned aerial vehicle. Journal of Guidance, Control, and Dynamics, 31(4):1163–1166, July - August 2008.

9. E. Johnson and M. Turbe. Modeling, control, and flight testing of small ducted fan aircraft. AIAA Guidance, Navigation and Control Conference, San Francisco, CA, August 2005.\

10. M. Smith, S. Swei, and M. Tischler. A study of the control of micro air vehicles using the linear dynamic inverse approach. AIAA 1st Intelligent Systems Technical Conference, Chicago, Il, September 2004.

11. C. Spaulding, M. Mansur, M. Tischler, R. Hess, and J. Franklin. Nonlinear inversion control for a ducted fan uav. AIAA Atmospheric Flight Mechanics Conference, San Francisco, CA, August 2005.

12. E. Tobias and J. Horn. Simulation analysis of the controllability of a tandem ducted fan aircraft. AIAA Atmospheric Flight Mechanics Conference, Honolulu, HI, August 2008.

13. G. Ozdemir and J. Horn. Control of ducted fan aircraft using redundant effectors. AIAA Atmospheric Flight Mechanics Conference, Chicago, Il, August 2009.

14. A. Ko, O. J. Ohanian, and P. Gelhausen. Ducted Fan UAV Modeling and Simulation in Preliminary Design, AIAA Modeling and Simulation Technologies Conference and Exhibit, Hilton Head, SC, August 2007.

15. X. Zhang, A. Myklebust, and P. Gelhausen. A Geometric Modeler for the Conceptual Design of Ducted Fan UAVs, AIAA "Unmanned Unlimited" Technical Conference, Chicago, Il, September 2004.

16. O. J. Ohanian and P. Gelhausen. A Compact Method for Modeling the Aerodynamics of Ducted Fan Vehicles, AIAA Aerospace Sciences Meeting, Orlando, FL, January 2010.

17. G. Avanzini and S. D'Angelo. Performance and stability of ducted-fan uninhabited aerial vehicle model. Journal of Aircraft, 40(1):86–93, January - February 2003.

18. O. Bilgen, K. Kochersberger, E. Diggs, A. Kurdila, and D. Inman. Morphing Wing Aerodynamic Con-trol via Macro-Fiber-Composite Actuators in an Unmanned Aircraft, AIAA infotech@Aerospace Confer- ence and Exhibit, May 2007.

19. O. Bilgen, K. Kochersberger, D. Inman, and O. Ohanian. Novel, Bi-Directional, Variable Camber Airfoil via Macro-Fiber Composite Actuators, AIAA Structures, Structural Dynamics, and Materials Conference, May 2009.

20. O. Bilgen, K. Kochersberger, E. Diggs, A. Kurdila, and D. Inman. Morphing Wing Micro-Air-Vehicles via Macro-Fiber-Composite Actuators, AIAA Structures, Sturctural Dynamics, and Materials Conference, Honolulu, HI, April 2007.

21. O. Bilgen, K. Kochersberger, and D. Inman. A Novel Aerodynamic Vectoring Control Airfoil via Macro-Fiber-Composite Actuators, AIAA Structures, Structural Dynamics, and Materials Conference, Schaumburg, IL, April 2008.

22. M. Marques, P. Gamboa, and E. Andrade. Design of a Variable Camber Flap for Minimum Drag and Improved Energy Efficiency, AIAA Structures, Structural Dynamics, and Materials Conference, Palm Springs, CA, May 2009.

23. H. M. Garcia, M. Abdulrahim, and R. Lind. In Roll Control for a Micro Air Vehicle Using Active Wing Morphing, AIAA Guidance, Navigation and Control Conference, Austin, TX, August 2003.

24. M. Abdulrahim, H. Garcia, G. F. Ivey, and R. Lind. In Flight Testing A Micro Air Vehicle Using Morphing For Aeroservoelastic Control, AIAA Structures, Structural Dynamics, and Materials Conference, Palm Springs, CA, April 2004.

25. B. L. Stevens and F. L. Lewis, *Aircraft Control and Simulation, 2nd Edition*, John Wiley & Sons, Hoboken, NJ, 2003.

26. B. Etkin, *Dynamics of Atmospheric Flight*, Dover Publications, Mineola, NY, 1972.

27. B. Etkin and L. D. Reid, *Dynamics of Flight: Stability and Control*, John Wiley & Sons, 1996.

28. D. McRuer, I. Ashkenas, and D. Graham, *Aircraft Dynamics and Automatic Control*, Princeton University Press, 1973.

29. G. Webb, A. Kurdila, and D. Lagoudas. Adaptive hysteresis model for model reference control with actuator hysteresis. Journal of Guidance, Control, and Dynamics, 23(3):459–465, May - June 2000.

30. F. Preisach, *Über die magnetische Nachwirkung*. *Zeitschrift für Physik*, 94:277-302, 1935.

31. M. Sunny and R. K. Kapania. A Modified Dynamic Preisach Model for Hysteresis, *AIAA/ASME/ASCE/AHS/ASC Structures, Structural Dynamics & Materials Conference*, Palm Springs, CA, California 2009.

32. G. Song, J. Zhao, X. Zhou, and J. A. D. Abreu-Garcia. Tracking control of a piezoceramic actuator wigh hysteresis compensation using inverse preisach model. *IEEE/ASME Transactions on Mechatronics*, 10(2):198–209, April 2005.

33. O. J. Ohanian, E. Karni, W. K. Londenberg, P. Gelhausen, and D. Inman. Ducted-fan force and moment control via steady and synthetic jets. *Journal of Aircraft*, 48(2):514–526, April 2011.

34. S. R. Viswamurthy and R. Ganguli. Effect of Piezoelectric Hysteresis Nonlinearity on Helicopter Vibration Control Using Trailing Edge Flaps, *AIAA/ASME/ASCE/AHS/ASC Structures, Structural Dynamics & Materials Conference*, Austin, TX, April 2005.

35. R. B. Williams and D. J. Inman. An overview of composite actuators with piezoceramic fibers. www.smart-material.com.

36. Wang, Y. F., Su, C. Y., Hong, H., & Hu, Y. M., Modeling and Compensation for Hysteresis of Shape Memory Alloy Actuators with the Preisach Representation, *IEEE International Conference on Control and Automation*, Guangzhou, China, May – June, 2007.

37. Y. Feng, C. A. Rabbath, T. Chai, & C. Y. Su, Robust Adaptive Control Systems with Hysteretic Nonlinearities: A Duhem Hysteresis Modeling Approach, *IEEE Africon*, Nairobi, Kenya, September, 2009.

38. A. J. Kurdila, & G. Webb, Compensation for Classes of Distributed Hysteresis Operators and Representation of Active Structural Systems, *AIAA Aerospace Sciences Meeting and Exhibit*, Reno, Nevada, January, 1997.

39. X. Lu, & H. Hanagud, Extended Thermodynamic Model for Piezoelectric Ceramics, *AIAA/ASME/ASCE/AHS/ASC Structures, Structural Dynamics, and Materials Conference*, Seattle, WA, April, 2001.

40. A. J. Kurdila & G. Webb, Compensation for Distributed Hysteresis Operators in Active Structural Systems, *AIAA Journal of Guidance, Control, and Dynamics*, Vol. 20, No. 6, pp. 1133-1140, November-December, 1997.

41. K. C. Stewart, K. Blackburn, J. Wagener, L. J. Czabaranek, and G. Abate. In Development and Initial Flight Tests of a Single-Jointed Articulated-Wing Micro Air Vehicle, *AIAA Atmospheric Flight Mechanics Conference*, Honolulu, HI, August 2008.

42. E. J. Abdullah, C. Bil, and S. Watkins. Application of Smart Materials for Adaptive Airfoil Control, *AIAA Aerospace Sciences Meeting*, January 2009.

43. K. Boothe, K. Fitzpatrick, and R. Lind. Controllers for Disturbance Rejection for a Linear Input-Varying Class of Morphing Aircraft, *AIAA/ASME/ASCE/AHS/ASC Structures, Structural Dynamics & Materials Conference*, Austin, TX, April 2005.

44. T. Martin, A. Guitton, R. Schmit, and M. N. Glauser. Development of a Morphing Micro Air Vehicle Wing Using the Combined POD and LSE Technique, *AIAA Infotech@Aerospace*, Arlington, VA, September 2005.

45. N. Ameri, E. Livne, M. H. Lowenberg, and M. I. Firswell. Modeling Continuously Morphing Aircraft for Flight Control, *AIAA Guidance, Navigation and Control Conference*, August 2008.

46. A. Lampton, A. Niksch, and J. Valasek. Morphing Airfoils with Four Morphing Parameters, *AIAA Guidance, Navigation and Control Conference*, Honolulu, HI, August 2008.

47. D. Inman and H. Cudney. Structural and machine design using piezoceramic materials: A guide for structural design engineers. Technical report, NASA Langley Research Center, April 2000.

48. F. Gern, D. Inman, and R. Kapania. Structural and aeroelastic modeling of general planform wings with morphing airfoils. AIAA Journal, 40(4):628–637, April 2002.

49. F. H. Gern, D. J. Inman, and R. K. Kapania. In Structural and Aeroelastic Modeling of General Planform UCAV Wings with Morphing Airfoils, AIAA/ASME/ASCE/AHS/ASC Structures, Structural Dynamics & Materials

Conference and Exhibit, Seattle, WA, April 2001.

50. C. O. Johnston, W. H. Mason, C. Han, H. H. Robertshaw, and D. J. Inman. In Actuator-Work Concepts Applied to Unconventional Aerodynamic Control Devices, AIAA/ISSMO Multidisciplinary Analysis and Optimization Conference, Albany, NY, September 2004.

51. K. Ogata, *Modern Control Engineering, Fourth Edition*, Pearson Education, Inc., Prentice Hall, Upper Saddle River, NJ, 2002.

52. M. Rakotondrabe, C. Clevy, and P. Lutz. Complete open loop control of hysteretic, creeped, and oscil- lating piezoelectric cantilevers. IEEE Transactions on Automation Science and Engineering, 7(3), July 2010.

53. R. Changhai and S. Lining. Hysteresis and creep compensation for piezoelectric actuator in open-loop operation. Elsevier Sensors and Actuators A: Physical, May 2005.

54. S. Lining, R. Changhai, R. Weibin, C. Liguo, and K. Minxiu. Tracking control of piezoelectric actuator based on a new mathematic model. Journal of Micromechanics and Microengineering, 14:1439–1444, August 2004.

55. B. Stiltner, C. Olien, and J. Faber. In Preliminary and Conceptual Design of a Remotely Piloted Ducted Fan MAV, AIAA Aerospace Sciences Meeting, Orlando, FL, January 2010.

56. B. Stiltner, C. Olien, J. Faber, R. Merritt, and S. Tanious. In Detailed Design, Construction, and Flight Tests of a Remotely Piloted Ducted Fan MAV, AIAA Aerospace Sciences Meeting, Orlando, FL, January 2010.